Model-Assisted Analysis of Electrochemical CO_2 Reduction at Ag Electrodes in Aqueous Electrolyte

Zur Erlangung des akademischen Grades einer

DOKTORIN DER INGENIEURWISSENSCHAFTEN (Dr.-Ing.)

von der KIT-Fakultät für
Elektrotechnik und Informationstechnik
des Karlsruher Instituts für Technologie (KIT)

angenommene

DISSERTATION

von

Inga Dorner, M.Sc.
geb. in Braunschweig

Tag der mündlichen Prüfung:	06.03.2026
Hauptreferentin:	Prof. Dr.-Ing. Ulrike Krewer
Korreferent:	Prof. Dr.-Ing. Thomas Turek

Kurzfassung[1]

Die atmosphärische CO_2-Konzentration ist in den letzten Jahrzehnten aufgrund der vom Menschen verursachten Emissionen dramatisch angestiegen, was den Anstieg der Erdtemperatur um mehrere Grad zur Folge hat und das Klima signifikant verändert. Um die katastrophalen Folgen des Klimawandels einzudämmen, müssen CO_2-Emissionen drastisch reduziert werden und zusätzlich eine CO_2-Ökonomie aufgebaut werden. Diese künstliche CO_2-Ökonomie umfasst die CO_2-Rückgewinnung aus der Atmosphäre, dessen Speicherung, den Transport und die Nutzung von CO_2. Die elektrochemische CO_2-Reduktion ist in diesem Zusammenhang eine vielversprechende Technologie, da sie das Recycling von CO_2 mithilfe von grünem Strom ermöglicht und mit CO_2 als Ausgangsstoff für Synthesen einen Beitrag zur Defossilisierung der chemischen Industrie und anderer Industriezweige leisten kann. Allerdings befindet sich die technische Umsetzung noch stark im Forschungsstadium und nur wenige Beispiele haben bisher eine hohe Technologiereife erreicht. Dies liegt unter anderem an den hohen Überpotentialen, geringer Produktselektivität und einem unvollständigen Verständnis der Wechselwirkungen zwischen den ablaufenden Prozessen bei der Untersuchung von Katalysatormaterialien und Elektrolytauswahl, sowie beim Betrieb und Design technischer Elektroden. All dies erschwert eine wissensbasierte Optimierung der Technologie und deren Scale-Up.

Diese Dissertation untersucht den Einfluss von Betriebsbedingungen und Elektrodendesignparametern an planaren Elektroden und Gasdiffusionselektroden und liefert detaillierte Einblicke in die lokalen Zustände innerhalb dieser Systeme durch umfassende physikochemische, dynamische Modellierung von Reaktionskinetik, Stoff- und Ladungstransport.
Zunächst werden die Unterschiede in der Leistung, d. h. im Elektrodenpotential und in der Produktselektivität, zwischen dynamischer und stationärer Analyse an planaren Silberelektroden unter kontrollierten Transportbedingungen aufgeklärt. Die Unterschiede resultieren aus langsamem Transport und Karbonatreaktionen, die zu einer zeitabhängigen CO_2-Verarmung und

[1] Portions of this thesis were drafted with assistance from the AI language model ChatGPT (GPT-5, OpenAI). The tool was used to improve grammar, spelling, clarity, and readability. All AI-generated content was carefully reviewed, edited, and approved. The final analyses, conclusions, and interpretations reflect my own work, and I take full responsibility for the content and accuracy of this thesis.

Elektrolytpufferung führen. Der dynamische Betrieb verbessert die faradaysche Effizienz, indem er das Gleichgewicht der Karbonatreaktionen verschiebt und den elektrochemischen CO_2-Verbrauch gegenüber dem chemischen Verbrauch begünstigt. Durch die Aufklärung der Unterschiede zwischen dynamischem und stationärem Betrieb trägt diese Forschung zum Verständnis der Prozesse während der elektrochemischen CO_2-Reduktion bei, bietet Methoden zur Identifizierung von Transportlimitierungen durch dynamische Messungen und liefert wichtige Hinweise für treffendere Leistungsbewertungen.
Der zweite Teil konzentriert sich auf die Optimierung der Leistung von planarer Silberelektroden durch Hinzufügen einer UiO-67-Beschichtung, einer metallorganischen Gerüstverbindung. Die Faradaysche Effizienz für die CO-Produktion steigt durch die Beschichtung von 0% auf 67% bei $-0.6\,\mathrm{V}$ vs. RHE und von 48% auf 90% bei $-1.2\,\mathrm{V}$ vs. RHE, wobei eine Faradaysche CO-Stromdichte von $-11.5\,\mathrm{mA\,cm^{-2}}$ erreicht wird. Simulationen decken auf, dass diese Steigerung der Leistung hauptsächlich durch die Erhöhung der lokalen CO_2 Aktivität resultierend aus der hohen CO_2-Speicherkapazität des MOFs erreicht wird und zustätzlich durch die selektive Verbesserung des CO_2 Transports in der porösen UiO-67 Struktur.
Um die erreichbaren Stromdichten der elektrochemischen CO_2-Reduktionin weiter zu erhöhen, werden in technischen Setups in der Regel Gasdiffusionselektroden eingesetzt. Diese ermöglichen durch die Schaffung eines Dreiphasensystems aus Katalysator, Gas- und Flüssigphase eine bessere CO_2-Versorgung, führen aber auch zu einem komplexeren Gesamtsystem. Experimentelle Variationen des Elektrodendesigns und der Betriebsparameter in Kombination mit makrokinetischer Modellierung identifizieren die kritischen Faktoren zur Optimierung der Faradayschen Effizienz von CO. Dabei zeigen sich besonders große Gas-Flüssig-Grenzflächen, kurze Flüssigkeitstransportwege und ein optimaler PTFE-Gehalt als entscheidend. So verdoppelt beispielsweise ein Überdruck von $40\,\mathrm{mbar}$ auf der Gasseite die CO-Faradaysche Effizienz bei $200\,\mathrm{mA\,cm^{-2}}$, während dünne Elektroden eine bessere Versorgung mit CO_2 und frischem Elektrolyt ermöglichen. Diese Erkenntnisse erlauben die gezielte Anpassung von Elektroden- und Betriebsparametern, um Gas- und Flüssigkeitsverteilung zu optimieren und kohlenstofffreie Gasdiffusionselektroden für CO_2-Reduktion als wettbewerbsfähiges Design zu etablieren.

Diese Arbeit nutzt modellbasierte Ansätze, um limitierende Prozesse in verschiedenen Elektrodenkonfigurationen aufzudecken und Optimierungsstrategien vorzuschlagen, um die Leistung der elektrochemischen CO_2-Reduktion an Silberkatalysatoren zu verbessern und damit einen Beitrag zur Weiterentwicklung der Technologie zu leisten. Für zukünftige Studien besteht die Möglichkeit, die entwickelten Modelle um weitere Zellkomponenten zu erweitern und so Einflüsse, beispielsweise der Gegenelektrode oder der Membran, zu untersuchen. Ebenso ist eine Übertragung der entwickelten Methoden auf andere Katalysator- und Elektrolytkombinationen denkbar. Zudem wäre die Untersuchung des Langzeitbetriebs der betrachteten Systeme im Hinblick auf eine technische Umsetzung von großem Interesse.

Abstract

Atmospheric CO_2 concentrations have dramatically increased in recent decades due to anthropogenic emissions. Mitigating climate change requires not only reducing CO_2 emissions but also establishing dedicated CO_2 infrastructures for carbon capture, storage, and utilization. Electrochemical CO_2 reduction is a promising technology within this area, enabling CO_2 recycling using green electricity and defossilizing the chemical and other industries by using CO_2 as a feedstock for synthesis. However, its technical application is still pending. This is partly due to the system's high overpotentials, low product selectivity, and an incomplete understanding of the interactions of key processes during the investigations of catalyst and electrolyte system. Moreover, there is an incomplete understanding of the operation of technical electrodes and the selection and effects of operating and electrode design parameters. All these aspects significantly hinder knowledge-based optimization of the technology and its scale-up.

This thesis investigates the effects of operating conditions and electrode design parameters at planar and gas diffusion electrodes, providing detailed insights into local states within these systems through comprehensive physicochemical modeling of reaction kinetics, species and charge transport.
Firstly, the study explains performance discrepancies between dynamic and steady-state analyses of planar silver electrodes under controlled transport conditions. These differences arise from slow transport and carbonation processes, leading to time-dependent CO_2 depletion and electrolyte buffering. Dynamic operation enhances Faradaic efficiency by the equilibrium shift of carbonate reactions, favoring electrochemical CO_2 consumption over chemical consumption. By clarifying the differences between dynamic and stationary operation, this research advances the understanding of electrochemical CO_2 reduction processes, offers methods for identifying transport limitations via dynamic measurements, and provides guidelines for more accurate performance assessment.
The second part investigates the performance enhancement of planar silver electrodes using a UiO-67 metal-organic framework coating. The Faradaic efficiency for CO increases from 0% to 67% at $-0.6\,\mathrm{V}$ and from 48% to 90 % at $-1.2\,\mathrm{V}$ vs. RHE, reaching a partial CO current density of $-11.5\,\mathrm{mA\,cm^{-2}}$. Simulations reveal that the improvement mainly arises from enhanced local CO_2 activity due to CO_2 uptake within the MOF, while a secondary contribution results from a selective improvement in CO_2 transport.

For an improvement of the system to reach higher absolute current densities, gas diffusion electrodes are usually used in technical setups. They create a three-phase system consisting of the catalyst, a gas and liquid phase, which results in a better CO_2 supply due to shortening of the CO_2 pathway to the catalyst surface. However, this also introduces greater complexity to the overall system. In the following, experimental variations in electrode design and operating parameters, combined with physicochemical modeling, identify critical factors for optimizing Faradaic efficiency toward CO at high current densities. Results highlight the importance of a distinct gas/liquid interface and short liquid transport distances in carbon-free electrodes. Increasing overpressure on the gas side by $40\,\mathrm{mbar}$ doubles the Faradaic efficiency for CO at high current densities of $200\,\mathrm{mA\,cm^{-2}}$, attributed to elevated local CO_2 concentrations in electrolyte-flooded regions. Furthermore, thin electrodes prove advantageous, yielding higher Faradaic efficiency for CO compared to thicker electrodes due to shorter transport distances, enhanced CO_2 supply, and improved fresh electrolyte transport, which reduces local pH. An optimal PTFE content minimizes the blockage of active surface area while maintaining sufficient hydrophobicity to stabilize the gas-liquid boundary. These insights enable tuning of electrode properties and operating conditions to optimize gas and liquid distribution, accelerating the improvement of carbon-free gas diffusion electrodes for CO_2 reduction and establishing competitive designs for future applications.

This work employs model-based approaches to uncover limiting processes in various electrode configurations and propose optimization strategies to enhance the performance of electrochemical CO_2 reduction at silver catalysts, contributing to the development of an efficient and scalable technology. The developed models can be further expanded to incorporate additional cell components, allowing the study of interactions and influences of the counter electrode and membrane. Furthermore, their application to other electrolyte and catalyst combinations is conceivable. In addition, evaluating long-term operation and its impact on the investigated systems and operating conditions would be highly valuable with respect to their technical implementation.

Danksagung

Der Inhalt dieser Arbeit entstand während meiner Zeit am Institut für Angewandte Materialien - Elektrochemische Technologien, die für mich auf vielfältige Weise lehrreich und spannend war, sodass ich sie nicht missen möchte und in der ich von so vielen Seiten stets unterstützt wurde.

Großer Dank geht an meine Betreuerin Prof. Ulrike Krewer für die Möglichkeit an diesem faszinierenden Thema forschen zu können und für ihre konstruktive, fördernde und motivierende Betreuung, dafür, auch in schwierigen Phasen Wege zum Erfolg zu finden, und dafür, mir die Freiheit zu geben, meinen eigenen Vorstellungen zu folgen.
Großer Dank geht auch an Prof. Thomas Turek für die Übernahme der Zweitbegutachtung dieser Arbeit und die Koordination der DFG-Forschergruppe FOR 2397, im Rahmen der ein Großteil des Inhalts dieser Arbeit entstand.

Ich danke allen Mitgliedern der FOR 2397 für die anregenden Projekttreffen und den wertvollen Austausch. Besonders bedanken möchte ich mich bei Jens Osiewarz und Dr. Barbara Ellendorff für ihre große Hilfsbereitschaft und herzliche Aufnahme am Institut für Chemische und Elektrochemische Technologien während meines Aufenthalts an der TU Clausthal.

Für die fachliche und persönliche Betreuung danke ich auch meinem Arbeitsgruppenleiter Dr. Philipp Röse, der mich umfassend in meiner Forschung und bei meinen Publikationen unterstützt hat. Mein besondererer Dank gilt zudem allen Mitgliedern der Elkat-Arbeitsgruppe. Ich habe die familiäre und stets hilfsbereite Arbeitsatmosphäre sowie die schönen Gruppenunternehmungen sehr geschätzt und genossen. Ein großes Dankeschön geht an Niklas Oppel und Ruth Witzel für den intensiven fachlichen Austausch und für das Korrekturlesen meiner Paper und dieser Arbeit und an Dr.-Ing. Maximilian Röhe, der mich gerade in der Anfangszeit und durch seine Forschung sehr unterstützt hat.

Ebenso danke ich allen Mitarbeiterinnen und Mitarbeitern des IAM-ETs für das liebenswerte Arbeitsklima und die vielfältige Unterstützung. Großer Dank geht auch an die Bouldergruppe für den sportlichen und spaßigen Ausklang nach Feierabend.

Ich möchte mich auch bei meinen Studierenden bedanken, die mich in meiner Forschung oder auch beim Literaturdatenmanagement des IAM-ETs tatkräftig unterstützt haben: Viktor Steinlein, Eric Cramer, Thomas Shaw, Tobias Schmid, Lisa Rodriguez-Pfützner und Luisa Weihing.

Nicht zuletzt möchte ich aus tiefstem Herzen meiner Familie und meinem Partner Thimo Brendel danken, die mich durch alle Höhen und Tiefen begleitet haben, mich so tatkräftig unterstützen in allem, was ich tue, und mir in dieser Zeit so viel Kraft, Freude und Zuversicht geschenkt haben.

Göttingen, Januar 2026 *Inga Dorner*

Publications within the Research of this Thesis

Journal publications

- I. Dorner, P. Röse, U. Krewer, "Dynamic vs. Stationary Analysis of Electrochemical Carbon Dioxide Reduction: Profound Differences in Local States", *ChemElectroChem* **2023**, 10, e202300387. https://doi.org/10.1002/celc.202300387.
- I. Dorner, J. Osiewacz, P. Röse, B. Ellendorff, M. Röhe, T. Turek, U. Krewer, "Control of Electrolyte Intrusion in Carbon-Free Silver Gas Diffusion Electrodes for Electrochemical CO_2 Reduction", *J. CO2 Util.* **2025**, 99, 103163. https://doi.org/10.1016/j.jcou.2025.103163.
- R. Witzel, W. Leonie, E. Tusini, S. Czioska, I. Dorner, A. Zimina, J.-D. Grunwaldt, P. Röse, "Investigation of the Performance and Stability of Copper and Brass Nanoparticles for CO_2 Reduction in Organic Electrolytes", *J. CO2 Util.*, **2025**, 97, 103138. https://doi.org/10.1016/j.jcou.2025.103138.

Conference contributions

- I. Dorner, P. Röse, U. Krewer, "Differences between Dynamic and Stationary Analysis of the Electrochemical CO_2 Reduction", *758. WE-Heraeus-Seminar : From Wind and Solar Energy to Chemical Energy Storage: Understanding and Engineering Catalysis under Dynamic Conditions* **2022**, online (Poster).
- I. Dorner, P. Röse, U. Krewer, "Differences between Dynamic and Stationary Analysis of the Electrochemical CO_2 Reduction", *32nd Topical Meeting of the International Society of Electrochemistry* **2022**, Stockholm, Sweden (Talk).
- I. Dorner, P. Röse, U. Krewer, "Electrochemical CO_2 Reduction: Steady-state vs. Dynamic Investigation", *Symposium on Insights into Gas Diffusion Electrodes: From Fundamentals to Industrial Applications* **2022**, Magdeburg, Germany (Poster).

- I. Dorner, P. Röse, J. Osiewacz, B. Ellendorff, T. Turek, U. Krewer, "Critical Role of Flooding Degree in Silver Gas Diffusion Electrodes for Electrochemical CO_2 Reduction", *Annual Meeting on Reaction Engineering* **2023**, Frankfurt, Germany (Talk).
- I. Dorner, P. Röse, J. Osiewacz, B. Ellendorff, T. Turek, U. Krewer, "Model-assisted Analysis of Carbon-free Silver Gas Diffusion Electrode Designs for Performance Enhancement in Electrochemical CO_2 Reduction", *20^{th} Symposium on Modeling and Experimental Validation* **2024**, Baden, Switzerland (Talk).
- I. Dorner, J. Osiewacz, P. Röse, B. Ellendorff, T. Turek, U. Krewer, "From RDE to GDE: A model-based Analysis of the Electrochemical CO_2 Reduction at Silver Electrodes", *Electrochemistry* **2024**, Braunschweig, Germany (Poster).

Contents

Kurzfassung . . . . . **i**

Abstract . . . . . **iii**

Danksagung . . . . . **v**

Publications within the Research of this Thesis . . . . . **vii**

1 Introduction **1**
1.1 Motivation and purpose 1
1.2 Scope and structure 3

2 Fundamentals **5**
2.1 Fundamentals of electrochemical systems 5
2.1.1 Reaction kinetics 5
2.1.2 Species transport 7
2.1.3 Phase interfaces and phase transitions 12
2.2 Experimental analysis methods 13
2.2.1 Stationary current-potential measurement 14
2.2.2 Cyclic voltammetry 14
2.2.3 Rotating disk electrode 17
2.2.4 Performance characteristics 19
2.3 Electrochemical CO_2 reduction 20
2.3.1 Reaction system 21
2.3.2 Aqueous electrolyte for CO_2R 23
2.3.3 Electrode and cell design 27
2.3.4 Modeling of CO_2 reduction 33
2.4 Concluding remarks 37

3 CO_2 Reduction at Planar Ag Electrodes **39**
3.1 Introduction 39
3.2 Dynamic macrokinetic modeling approach for planar electrode 41
3.3 Experimental characterization 47

3.4 Results and discussion . . . 48
3.4.1 Dynamic vs. steady-state behavior . . . 48
3.4.2 Impact of species transport . . . 52
3.4.3 Impact of carbonation reaction . . . 54
3.4.4 Faradaic efficiency . . . 58
3.5 Concluding remarks . . . 59

4 CO_2 Reduction Enhancement with Metal-Organic Framework Coating . . . 61
4.1 Introduction . . . 61
4.2 Experimental details . . . 63
4.2.1 Synthesis of UiO-67/Ag system via Vapor Assisted Conversion . . . 63
4.2.2 Electrochemical characterization . . . 64
4.3 Model details . . . 65
4.4 Results and discussion . . . 67
4.5 Concluding remarks . . . 72

5 CO_2 Reduction in Ag Gas Diffusion Electrodes . . . 73
5.1 Introduction . . . 73
5.2 Experimental section . . . 76
5.2.1 Electrode preparation . . . 76
5.2.2 Electrochemical characterization and product analysis . . . 76
5.3 Macrokinetic modeling approach for GDE . . . 77
5.3.1 Model description . . . 78
5.3.2 Numerical simulation and parametrization . . . 83
5.4 Results and discussion . . . 83
5.4.1 Current and concentration distribution along the GDE . . . 84
5.4.2 Electrolyte intrusion behavior of the GDE . . . 86
5.4.3 Local sensitivity analysis . . . 93
5.5 Concluding remarks . . . 95

6 Conclusion and Perspective . . . 97
6.1 Summary and conclusion . . . 97
6.2 Perspective . . . 98

List of Symbols and Abbreviations . . . 101

A Supporting Information . . . 107
A.1 Supporting information of Chapter 3 . . . 107
A.1.1 Variation of rotation rate . . . 107
A.1.2 Impact of carbonation reactions . . . 108
A.1.3 Impact of electrolyte concentration . . . 110

A.2 Supporting information of Chapter 4 . . . 112
A.2.1 Chronoamperometric measurements for product analysis . . . 112
A.2.2 Double-layer capacitance measurements . . . 112
A.2.3 Reproducibility of electrochemical measurements . . . 112
A.2.4 Local sensitivity analysis . . . 113
A.3 Supporting information of Chapter 5 . . . 116
A.3.1 Binary diffusion coefficients in the gas phase . . . 116
A.3.2 Diffusion length of dissolved CO_2 . . . 117
A.3.3 Tafel plot . . . 117
A.3.4 Variation of electrode thickness . . . 117
A.3.5 3D FIB-SEM reconstruction of porous electrode structure . . . 119
A.3.6 Experimental Faradaic efficiencies . . . 120
A.3.7 Profile root mean square error analysis . . . 120

List of Figures . . . **123**

List of Tables . . . **127**

1 Introduction

1.1 Motivation and purpose

The concentration of carbon dioxide has been increasing exponentially over the past decades due to anthropocentric emissions, reaching 422 ppm in 2024 (Figure 1.1A).[1] This drastic increase in CO_2 has dramatic consequences for the climate and the environment. Thus, 2024 is the first calendar year that the average global temperature exceeded $1.5\,^{\circ}\mathrm{C}$ above its pre-industrial level. Global warming and the acidification of the oceans trigger rising sea levels, polar ice cap melting, an increase in extreme weather events, desertification, and biodiversity loss. To mitigate the risks and impacts of the climate crisis, the Paris Agreement set the goal of "holding the increase in the global average temperature to well below $2\,^{\circ}\mathrm{C}$ above pre-industrial levels and pursuing efforts to limit it to $1.5\,^{\circ}\mathrm{C}$".[2] Achieving this target requires a net-zero emissions strategy, which involves balancing greenhouse gas emissions, primarily CO_2, with their removal from the atmosphere by 2050. This goal can only be realized through a significant reduction in CO_2 emissions and the development of a robust carbon dioxide infrastructure for carbon capture, storage, transportation, and utilization, particularly to address hard-to-abate emissions.
Carbon capture and storage technologies enable the capture of CO_2 from exhaust gas streams or directly from the atmosphere. This can be achieved through, e.g., chemical or physical adsorption or membrane processes included in a pre- or post-combustion process.[3] Subsequently, the captured CO_2 is stored long-term in geological formations such as deep saline aquifers or depleted oil

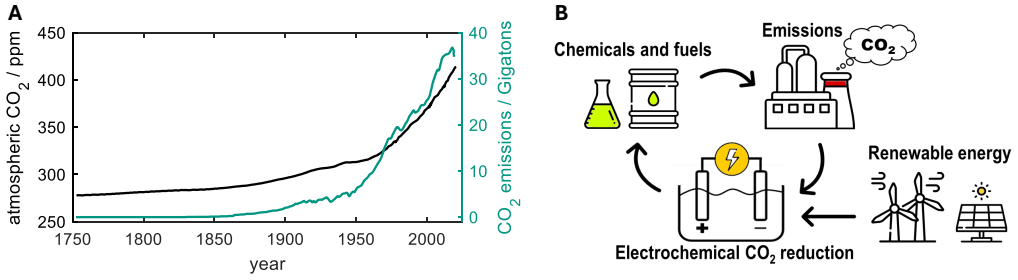

Figure 1.1: (A) Global atmospheric carbon dioxide concentration over time compared to annual CO_2 emissions [1] and (B) scheme of CO_2 life cycle via electrochemical CO_2 reduction.

and gas reservoirs. However, the selection of storage sites remains controversial due to potential environmental impacts and competition with other applications, such as geothermal energy. In addition, the storage of CO_2 is not economically attractive.

CO_2 utilization complements the CO_2 economy by converting purified CO_2 into value-added products. These technologies are not strictly negative-emission technologies, as their effectiveness depends on the lifetime of the product in which the CO_2 is stored. Nevertheless, CO_2 utilization allows for the use of CO_2 as a carbon source, defossilizing the chemical industry, and closing the CO_2 life cycle. Target products can be synthesized using thermocatalytic, photochemical, biochemical, electrochemical, and hybrid methods.[4, 5]

Electrochemical CO_2 reduction (CO_2R), which employs electrocatalysis to convert CO_2 into valuable chemicals (Figure 1.1B), is a promising approach in CO_2 utilization. Depending on the catalyst material, reaction environment (e.g., pH or presence of ions), and process conditions, a variety of products can be generated, including carbon monoxide, formic acid, ethanol, methane, or ethylene. The advantages of electrochemical CO_2 reduction include moderate operating conditions under ambient pressure and temperature, the direct use of electricity as an energy source, and non-toxic solvents and by-products.

Despite its potential, this technology remains at the stage of fundamental research and pilot-scale implementation. Electrocatalysts often operate at high overpotentials to achieve acceptable reaction rates, while Faradaic efficiency and energy efficiency toward desired products remain low. Electrochemical catalysis of CO_2 to CO on silver is still one of the more promising reaction systems, with a Faradaic efficiency of 60% to 90% and an energy efficiency of approx. 10% to 50%.[6, 7] The reason for the observation of low Faradaic efficiencies is that the CO_2R constantly competes with other side reactions and processes, such as the hydrogen evolution reaction (HER), mass transport limitations, and the change in local conditions (e.g., pH fluctuation and concentration gradients). Advancing this technology requires the further development of improved catalyst materials and electrode designs, along with the identification of optimal operating conditions, to enable commercialization and scale-up.

The objective of this thesis is to investigate electrochemical CO_2R on silver-based electrodes using model-assisted methods. The aim is to understand the impact of transport and reaction processes at and within the electrodes on performance and identify limiting factors under defined operating conditions. This helps enhance both the energy efficiency and the Faradaic efficiency of the target product in this system.

1.2 Scope and structure

This thesis investigates electrochemical CO_2R on silver-based electrodes in aqueous electrolytes to convert CO_2 into CO with experimental and especially model-based methods.
The main research questions are:

- Which influence does potential, local pH value, and CO_2 concentration have on the current density and product distribution of the CO_2R?
- To what extent do intermediates and carbonation reactions influence the electrode behavior and performance of CO_2R?
- To what extent does dynamic analysis provide a deeper insight into the processes taking place?
- How do the position of the phase boundary and the electrolyte distribution in gas diffusion electrodes influence the local reaction state and electrode performance?

The following chapter introduces the fundamentals of electrochemical systems, including fundamental principles of describing electrochemical reaction kinetics, species transport, phase interfaces, and key performance metrics used to evaluate system efficiency. This is followed by insights into experimental methods for electrochemical analysis, which are used in this work for the experimental characterization of CO_2R. Fundamentals of CO_2R are introduced by focusing on the general reaction network. This is followed by a brief discussion of the impact of electrolytes and an overview of existing electrode and cell designs. The latter part of the chapter provides a review of the state-of-the-art deterministic modeling of electrochemical CO_2 reduction.
The third chapter compares dynamic and stationary analyses of CO_2 reduction on planar silver electrodes under controlled mass transport conditions. The study includes the model-based analysis of cyclic voltammograms and polarization curves on silver rotating disk electrodes.
The fourth chapter demonstrates the potential for enhancing performance by modifying the surfaces of planar silver electrodes with metal-organic framework coatings. Physico-chemical simulations were employed to elucidate the underlying mechanisms responsible for the observed improvements in Faradaic efficiency and current density.
The fifth chapter presents a study on silver gas diffusion electrodes with a focus on understanding the effects of operating and electrode parameters on half-cell performance. Through systematic variation of electrode thickness, gas-side overpressure, and PTFE content in the electrode, both experimentally and via simulations, the main factors contributing to performance limitations are identified.
The thesis concludes with a summary of the main findings from each chapter, deriving key insights and offering an outlook on future research.

2 Fundamentals

2.1 Fundamentals of electrochemical systems

Electrochemical systems are fundamental to a wide range of technologies that convert chemical energy into electrical or vice versa. They encompass diverse fields of applications such as energy storage (batteries), energy conversion (electrolyzer, fuel cell), and the electrosynthesis of value-added chemicals. What these systems have in common is the coupling of charge-transfer reactions at electrode/electrolyte interfaces with ionic transport through the electrolyte and a separate electron conduction within the electrodes.
The performance of an electrochemical system is often governed by the interplay between reaction kinetics, transport effects, as well as the formation of phase interfaces and interfacial phenomena. The following section explains the fundamentals used to describe these processes, which are relevant to electrochemical systems in general and are applied in this work.

2.1.1 Reaction kinetics

The starting point for describing electron transfer processes is a one-step transfer reaction at the electrode surface, where oxidized (Ox) and reduced species (Red) exchange z electrons according to:

$$\nu_{\mathrm{Ox}}\mathrm{Ox} + \mathrm{ze}^- \rightleftharpoons \nu_{\mathrm{Red}}\mathrm{Red}. \tag{2.1}$$

with the stoichiometric coefficients of the species ν_{Ox} and ν_{Red}. A central equation used to describe electron transfer kinetics is the Butler-Volmer equation, which expresses the exponential relationship between current density j and the overpotential η. The Butler-Volmer equation is given as:

$$j = j_0 \left\{ \exp\left[\frac{\alpha z \mathrm{F}}{\mathrm{R}T}\eta\right] - \exp\left[\frac{-(1-\alpha) z \mathrm{F}}{\mathrm{R}T}\eta\right] \right\}. \tag{2.2}$$

The current density is an expression for the reaction rate of the electrochemical reaction, driven by η as the driving force. The first term of Equation 2.2 corresponds to the anodic current density j_{a} and the second term to the cathodic current density j_{c} (Figure 2.1A). The degree of increase

of each branch of the current density depends on the exchange current density j_0 and the charge transfer coefficient α. Butler-Volmer kinetics normally only apply to elementary reactions that involve a single step and one electron transfer with $z = 1$.
Different forms of the Butler-Volmer equation are used. A comprehensive overview is provided by Dickinson et al.[8] One expression, which makes the concentration dependence of the exchange current density conceptually clear and uses the heterogeneous rate constant k_0 to describe the rate of electron transfer, is:

$$j = Fz\left\{k_{0,\mathrm{a}}\exp\left[\frac{\alpha z\mathrm{F}}{\mathrm{R}T}\eta\right]\prod a_{\mathrm{Red}}^{\nu_{\mathrm{Red}}} - k_{0,\mathrm{c}}\exp\left[\frac{-(1-\alpha)z\mathrm{F}}{\mathrm{R}T}\eta\right]\prod a_{\mathrm{Ox}}^{\nu_{\mathrm{Ox}}}\right\} \tag{2.3}$$

where the product of activities of the reduced and oxidized reactants a_{Red} and a_{Ox}, along with their stoichiometric coefficients ν_{Red} and ν_{Ox}, following the rate law of chemical reactions.
At equilibrium, when the anodic and cathodic currents are equal, the net current is zero. In this state, the Butler-Volmer equation reduces to the Nernst equation by setting $\frac{j}{j_0} = 0$ and $\eta_{\mathrm{eq}} = E_{\mathrm{eq}} - E^0$[8, 9]:

$$E_{\mathrm{eq}} = E^0 + \ln\frac{\prod a_{\mathrm{Ox}}^{\nu_{\mathrm{Ox}}}}{\prod a_{\mathrm{Red}}^{\nu_{\mathrm{Red}}}}\cdot\frac{\mathrm{R}T}{z\mathrm{F}}. \tag{2.4}$$

At the turn of large absolute values of η, either the anodic or cathodic terms become negligible. This simplifies Equation 2.2 for anodic term to:

$$j = j_0\exp\left[\frac{\alpha z\mathrm{F}}{\mathrm{R}T}\eta\right] \tag{2.5}$$

and for cathodic term to:

$$j = -j_0\exp\left[\frac{(1-\alpha)z\mathrm{F}}{\mathrm{R}T}\eta\right]. \tag{2.6}$$

By taking the logarithm of these expressions, the Tafel equation is obtained:

$$\lg|j| = \lg j_0 + \frac{\alpha z\mathrm{F}}{2.3\mathrm{R}T}\eta \tag{2.7}$$

and

$$\lg|j| = \lg j_0 - \frac{(1-\alpha)z\mathrm{F}}{2.3\mathrm{R}T}\eta. \tag{2.8}$$

This form is used to generate a Tafel plot, where j is plotted semilogarithmically against η. From this plot, α can be easily determined from the linear slope, and j_0 from the y-axis intercept (Figure 2.1B).

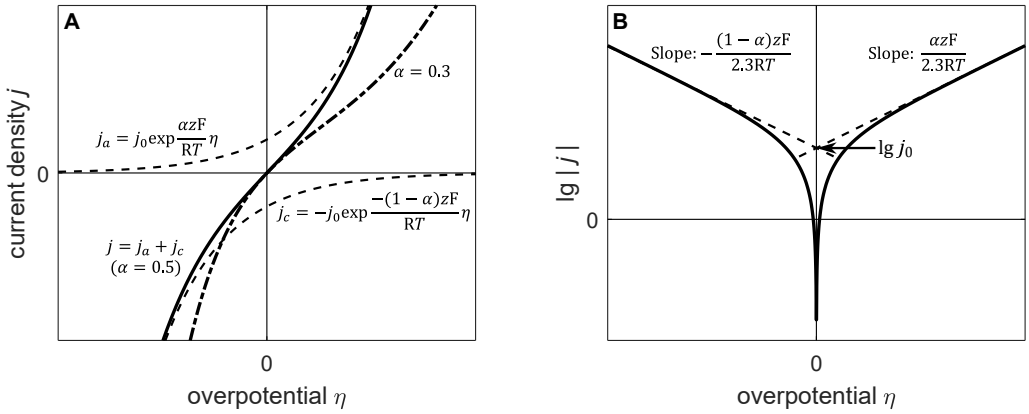

Figure 2.1: (A) Current density-overpotential curve of electron-transfer reaction with $\alpha = 0.5$ as a sum of cathodic and anodic current density according to Butler-Volmer equation and current density-overpotential curve for $\alpha = 0.3$. (B) Tafel plot for electron-transfer reaction ($\alpha = 0.5$) with Tafel equation as the linear slope at high values of $|\eta|$. Adapted from Hamann et al.[10].

2.1.2 Species transport

However, many electrochemical systems deviate from Butler-Volmer behavior at high overpotentials due to the influence of mass transport. This makes considering mass transport essential for most systems. The following section describes the transport of charged and uncharged species in dilute electrolyte solutions. The restriction to dilute solutions allows the neglect of species interactions and the use of transport properties of the species independent of the local system state.

The transport can be calculated by the Nernst-Planck equation. It describes the flux of the species i N_i by Fickian diffusion due to concentration gradient ∇c_i, by migration due to impact of an electric field resulting in a potential gradient in the electrolyte $-\nabla \phi_\mathrm{E}$, and by a convective term due to the motion of liquid phase with the velocity v:

$$\underbrace{N_i}_{\text{flux}} = \underbrace{-D_i \nabla c_i}_{\text{diffusion}} \underbrace{-z_i u_i \mathrm{F} c_i \nabla \phi_\mathrm{E}}_{\text{migration}} \underbrace{+c_i v}_{\text{convection}} \tag{2.9}$$

with the diffusion coefficient D_i and the mobility u_i as transport properties of the species i. In dilute solutions, the mobility of the species can be estimated from the diffusion coefficients using the Nernst-Einstein equation:

$$u_j = \frac{D_j}{\mathrm{R}T}. \tag{2.10}$$

2.1.2.1 Fickian diffusion

In general, diffusion is the transport of species due to a gradient in the chemical potential μ_i.

$$N_{i,\mathrm{diff}} = -L_i \nabla \mu_i \tag{2.11}$$

where L_i is the coefficient of proportionality.[11] With the restriction that the gradient of the chemical potential is only due to a concentration gradient, i.e., with ideal behavior and the exclusion of e.g., temperature gradients, pressure gradients, or electrical potential gradients, the chemical potential can be expressed by concentration in term of $\mu_i = \mu_i^0 + \mathrm{R}T\ln(\gamma_i c_i)$ and setting activity coefficients γ_i to 1. This results in the most common form of the concentration-dependent Fick's law:

$$N_{i,\mathrm{diff}} = -\frac{\mathrm{R}TL_i}{c_i}\nabla c_i = -D_i \nabla c_i \tag{2.12}$$

where $\mathrm{R}TL_i/c_i$ can be replaced by diffusion coefficient D_i. In addition to the spatial description of the first law, Fick's second law enables the temporal resolution of the transport process with

$$\frac{\partial c_i}{\partial t} = D\frac{\partial^2 c_i}{\partial x^2}. \tag{2.13}$$

Equation 2.13 represents the dynamic species balance including diffusive transport.
As an approximation, the ideal behavior of species, isothermal, and isobaric conditions can be well assumed for most electrochemical systems, including CO_2R, which supports the use of concentration-dependent Fickian diffusion (Eq. 2.12).

2.1.2.2 Migration and electrolyte potential

In addition to diffusive transport, an electric field exists between the electrodes in the electrochemical system, influencing the movement of charged species. Consequently, the transport equation must be extended to account for this effect. The shown Nernst-Planck equation (Eq. 2.9) extends the Fickian diffusion with a term for migrative transport expressed by an electric field $\mathbf{E}$ or by the spatial gradient of potential $\nabla\phi$, applying electrostatics $\mathbf{E} = -\nabla\phi$.

$$N_{i,\mathrm{mig}} = z_i u_i \mathrm{F} c_i \mathbf{E} = -z_i u_i \mathrm{F} c_i \nabla \phi_{\mathrm{E}} \tag{2.14}$$

This describes the transport of ionic species in the electrolyte. The sum of ionic flux results in an ionic current, which is equal to the electric current density j.

$$j = \mathrm{F}\sum_{i=1}^{n} z_i (N_{i,\mathrm{diff}} + N_{i,\mathrm{mig}}) \tag{2.15}$$

Convective flow does not matter for the ionic current because convection transports positive and negative charged species in the same way, resulting in zero net current. The species balance can also be extended by a migrative term leading to

$$\frac{\partial c_i}{\partial t} = -\nabla(-D_i \nabla c_i - z_i u_i \mathrm{F} c_i \nabla \phi_\mathrm{E}). \tag{2.16}$$

Besides the concentrations of each species, the gradient of potential in the electrolyte is unknown. With n species balances and $n+1$ unknown state variables, there is an additional equation required to close the equation system. There are some possibilities to create such a closing condition.

- **Poisson** The most straightforward and fundamental approach for calculating the potential gradient is applying Poisson's equation, which describes the potential generated by electric charge density ρ_e

  $$\nabla^2 \phi_\mathrm{E} = -\frac{\rho_\mathrm{e}}{\epsilon} = -\frac{\mathrm{F}}{\epsilon} \sum_i z_i c_i \tag{2.17}$$

  with ϵ as the permittivity valid for a medium with constant permittivity.[12] This approach enables the description of the charge separation in the electrical double layer next to the electrode surface. In turn, this requires the local resolution of the EDL, which has a total thickness of between 1 and 10 nm. Most macroscopic models do forgo such a low local resolution for computational time reasons, which is why other closing conditions are common.

- **Electroneutrality** Charge separation in the electrolyte is only present in the small area of the EDL. In the diffusion layer and electrolyte bulk, electroneutrality is given. This is because any spatial separation of charge carriers generates strong electrostatic forces that counteract further separation. Consequently, charge separation can only persist at the electrode/electrolyte interface, where the approach of charged species to the electrode is limited by their hydrated molecular radius. Therefore, relevant charge separation exists only within the EDL, justifying the common assumption that the electrolyte solution is locally electroneutral:

  $$\rho_e = \mathrm{F} \sum_i c_i z_i = 0, \tag{2.18}$$

  valid for electrolyte bulk, membranes, and the diffusion layer, but not for the EDL. The EDL in these models is considered as a rapid potential drop without spatial resolution. In the case of Equation 2.18 as a closing condition, $\nabla \phi_\mathrm{E}$ is not explicitly mentioned. To do

so, electroneutrality can be included in the Nernst-Planck equation (Eq. 2.9), leading to a differential-algebraic system:

$$\sum_i z_i \mathrm{F} \nabla N_i = -\nabla \left[\left(\sum_i \frac{z_i^2 \mathrm{F}^2 D_i}{\mathrm{R}T} c_i \right) \nabla \phi_\mathrm{E} - \sum_i z_i \mathrm{F} D_i \nabla c_i \right] = 0 \tag{2.19}$$

which can be used as a so-called hidden constrain.[13]

- **Charge conservation** Charge neutrality can also be enforced by setting the divergence of j to zero:

$$\nabla \cdot j = 0. \tag{2.20}$$

This means that there are no sinks or sources of net current in the electrolyte resulting in equal transport of negative and positive ions. This closing condition is often referred to as charge conservation. Combining this with the equation of ionic current (Eq. 2.15) leads to

$$\nabla \cdot j = \nabla \cdot \left[\mathrm{F} \sum_i z_i (N_{i,\mathrm{diff}} + N_{i,\mathrm{mig}}) \right] = 0. \tag{2.21}$$

This can be reformulated to an equation to calculate $\nabla \phi_\mathrm{E}$ explicitly

$$\nabla \cdot (\sigma \nabla \phi_\mathrm{E}) + F \sum_i z_i \nabla (D_i \nabla c_i) = 0 \tag{2.22}$$

with the local ionic conductivity of the electrolyte $\sigma = \mathrm{F}^2 \sum_i \frac{z_i^2 D_i}{\mathrm{R}T} c_i$. This equation is obviously identical to the hidden constraint of electroneutrality (Eq. 2.19). This means that the condition derived from electroneutrality is also accompanied by conservation of charge.

2.1.2.3 Stefan flow

The last term in the Nernst-Planck equation (Eq. 2.9) describes convective transport, which results from gradients in density or an external flow field. Given its relevance in the gas diffusion models of CO_2 reduction, the fundamentals and assumptions of Stefan flow as a form of convective transport are described.

The phenomenon of general two-sided diffusion, or one-sided diffusion in a particular case, occurs at interfaces that are semi-permeable allowing only specific species from a mixture to pass through. Examples include gas/liquid phase boundaries where species have very different vapor pressures or interfaces with sink or source terms due to chemical or electrochemical reactions.

An illustrative example is a gas/liquid interface in a binary mixture where component A evaporates

and an inert component B exists solely in the gas phase, unable to condense (Figure 2.2). This example represents one-sided diffusion, where the phase transition occurs in only one direction. As component A evaporates, a stationary diffusion flux, $N_{\mathrm{A,diff}}$, occurs due to the gradient between the partial pressure of A at the phase boundary p_{A}^{*} and the partial pressure in the gas bulk $p_{\mathrm{A}}^{\mathrm{bulk}}$. Assuming constant total pressure p along the local coordinate x, a diffusion flux $N_{\mathrm{B,diff}}$ towards the phase boundary also forms for the inert component B. However, since no sink term for B exists here and accumulation of B is not expected, a convective flux $N_{\mathrm{B,conv}}$ is introduced that cancels the diffusion flux of B:

$$N_{\mathrm{B,diff}} + N_{\mathrm{B,conv}} = 0. \tag{2.23}$$

Since the convective flux also transports component A in the same way, the total flux of A is increased by this convective part. The total fluxes of both components can be calculated by accounting for diffusive and convective terms by

$$N_{\mathrm{A}} = -\frac{D}{\mathrm{R}T}\frac{\mathrm{d}p_{\mathrm{A}}}{\mathrm{d}x} + v_{\mathrm{conv}}\frac{p_{\mathrm{A}}}{\mathrm{R}T} \tag{2.24}$$

and

$$N_{\mathrm{B}} = -\frac{D}{\mathrm{R}T}\frac{\mathrm{d}p_{\mathrm{B}}}{\mathrm{d}x} + v_{\mathrm{conv}}\frac{p_{\mathrm{B}}}{\mathrm{R}T} \tag{2.25}$$

with v_{conv} representing the velocity of the convective Stefan flow. This velocity can be determined using Equation 2.23 resulting in

$$v_{\mathrm{conv}} = \frac{D}{p_{\mathrm{B}}}\frac{\mathrm{d}p_{\mathrm{B}}}{\mathrm{d}x}. \tag{2.26}$$

Using this expression and assuming constant total pressure $p = p_{\mathrm{A}} + p_{\mathrm{B}}$, the flux of A can be reformulated as

$$N_{\mathrm{A}} = -\frac{D}{\mathrm{R}T}\frac{p}{p - p_{\mathrm{A}}}\frac{\mathrm{d}p_{\mathrm{A}}}{\mathrm{d}x}. \tag{2.27}$$

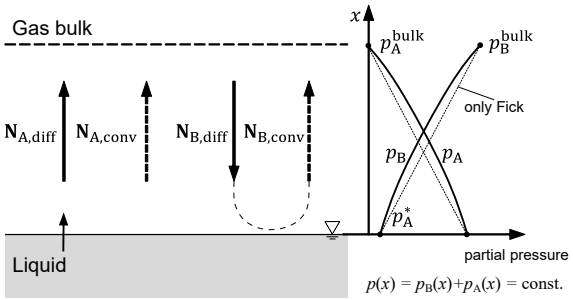

Figure 2.2: Stationary one-sided diffusion at a gas/liquid phase boundary with convective Stefan flow. Partial pressure profiles in the diffusion layer with and without convective flux are shown. Adapted from Kögl et al.[14].

This formulation highlights that the flux of A is increased by the factor $\frac{p}{p-p_A}$ due to the Stefan flow. The impact of the convective flux becomes negligible if the proportion of the inert component B is large, such that $\frac{p}{p-p_A}$ approaches 1.
This one-sided diffusion approach can be extended to general two-sided diffusion, in which the different diffusion fluxes of the components are balanced to an equimolar flux by a convective term. In this work, this method was applied to describe the liquid/gas phase boundary in the gas diffusion electrode model (Chapter 5).

2.1.3 Phase interfaces and phase transitions

Some electrochemical systems exhibit the coexistence of gas and liquid phases, such as electrochemical CO_2 reduction when using gas diffusion electrodes. The presence of the gas-liquid interface is critical to electrode and overall cell performance. The following section briefly discusses the fundamentals of describing phase transition processes and calculating the composition of the liquid and gaseous phases at the interface.
An ideal mixture of substances is considered. The partial pressure of the individual components in the gas phase, which is in equilibrium with the liquid phase, is proportional to the mole fraction x_i of these components in the liquid, with the equilibrium pressure of the pure substance p_i^{sat}, also known as the saturation vapor pressure, serving as the proportionality constant:

$$p_i = x_i p_i^{\mathrm{sat}}. \tag{2.28}$$

This relationship corresponds to Raoult's law and is valid if the components of the system are very similar in their interactions with each other or if the species under consideration, i, is present in a high concentration/mole fraction and the interaction with the other components can therefore be neglected. In this case, the partial pressure of a nonideal solution approaches that of an ideal solution (Figure 2.3). For the purpose of this work, Raoult's law is applied to describe the evaporation of water as a solvent in the context of electrochemical CO_2 reduction.
Henry's law is used to describe the solubility of gases in a liquid. It states that the mole fraction of the component i in the liquid phase is proportional to the partial pressure of i in the gas phase, with Henry's law constant H_i^{xp}:

$$x_i = H_i^{\mathrm{xp}} p_i. \tag{2.29}$$

Henry's law constant varies as a function of temperature, total pressure, and solvent. The

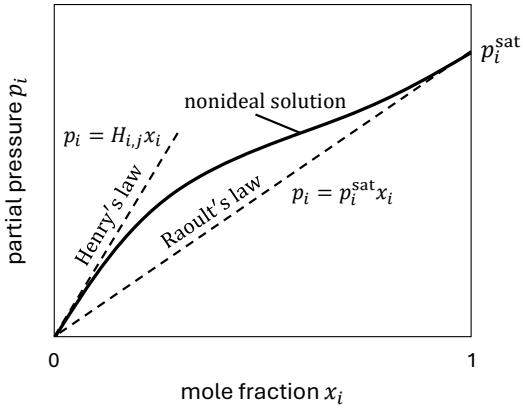

Figure 2.3: Positive nonideal behavior of the vapor pressure of a component i in a solution follows Henry's law at low mole fraction and Raoult's law at high mole fractions at constant temperature. Adapted from Czeslik et al.[15].

upper index delineates the methodology employed in the calculation. Calculations based on concentrations are also common, resulting in:

$$c_i = H_i^{\mathrm{cp}} p_i. \tag{2.30}$$

Equation 2.1.3 is used to calculate the CO_2 solubility in the aqueous electrolyte in all models developed and applied in this work. In addition, the decrease in solubility caused by the presence of the electrolyte salt is taken into account, as described in section 3.2.

2.2 Experimental analysis methods

Building on the fundamental principles of reaction kinetics, species transport, and interfacial phenomena outlined above, the following section introduces the experimental methods used in this work to analyze electrochemical systems. These techniques enable the systematic investigation of the processes previously described and provide the basis for evaluating electrode and cell behavior.

Experimental analysis of electrochemical systems is primarily based on analyzing the potential-current relationship. Measurements can be conducted under either potential or current control, with various input signal options depending on the scope of the investigation, available equipment, and the specific electrochemical systems. In the following section, the techniques of stationary current-potential measurements and cyclic voltammetry are introduced as common measurement

methods, which were also applied in this work. Additionally, the concept of rotating disk electrodes, a setup for kinetic investigations in electrochemistry, is described.

2.2.1 Stationary current-potential measurement

The most basic method for measuring the relationship between current and potential involves applying a constant input signal and extracting the stationary response of the system. Stationary means that current and potential are no longer varying with time. Typically, the system response becomes stable after several seconds to minutes, depending on the reaction rate and diffusion layer formation.[10] Using stationary methods has the advantage of excluding the effects of charge and discharge phenomena in the electrical double layer. Current-potential value pairs can be recorded either by controlling potential (potentiostatic mode) or by controlling current (galvanostatic mode).
In potentiostatic measurements, the potential between the working and reference electrodes is controlled, and the resulting current density between the working and counter electrodes is measured. This control is analogous to chemical kinetic measurements, where concentration or temperature is varied as an input parameter and the reaction rate is determined. Additionally, controlling the potential more precisely defines which reactions are taking place, as individual oxidation or reduction reactions occur at specific potential values.[16] This precision makes potentiostatic measurements a preferred choice in fundamental electrochemistry. However, potentiostatic setups are more complex and costly than galvanostatic setups, as they require a feedback loop to maintain potential control between the working and reference electrodes by adjusting the current density.[9]
In contrast, galvanostatic measurements control the current density directly. By setting the current density, the reaction rate and conversion are directly controlled, as they are proportional to the current density. This simplicity in setup and operation makes galvanostatic control attractive for technical and large-scale applications.

2.2.2 Cyclic voltammetry

In addition to stationary measurements, techniques capable of capturing the transient behavior of electrochemical systems are available and are particularly valuable for investigating complex reaction mechanisms and differentiating between diffusion-controlled and charge-transfer limited reactions. A common transient technique is cyclic voltammetry. It is characterized by a triangular voltage wave over time within a defined potential range between the potentials E_1 and E_2. The slope of the linear sweep is referred to as the scan rate $\nu = \frac{\mathrm{d}E}{\mathrm{d}t}$. During cyclic voltammetry, forward

and backward sweeps are repeated multiple times until the system reaches a quasi-stationary state, in which the potential-current curve becomes independent of the cycle number n. The potential input over time, focusing on reduction, can be expressed mathematically for a given cycle (starting at $n = 1$) as

$$E(t) = \begin{cases} E_1 - \nu\,(t - (2n-2)t_{\text{switch}})\,, & \text{for } 0 \leq t - 2nt_{\text{switch}} < t_{\text{switch}} \\ E_2 + \nu\,(t - (2n-1)t_{\text{switch}})\,, & \text{for } t_{\text{switch}} \leq t - 2nt_{\text{switch}} < 2t_{\text{switch}} \end{cases} \tag{2.31}$$

where t_{switch} is the time required for a single potential sweep and marks the point at which the sweep direction changes (Figure 2.4A). For a reversible electrochemical reduction, the current-potential curve, also called the cyclic voltammogram (CV), exhibits a characteristic shape, as shown in Figure 2.4B. In terms of concentration profiles, it is assumed that only the oxidized species Ox is present in the bulk and under initial conditions.

During the forward scan, as the potential is decreased, the cathodic current density (denoted by a negative sign according to IUPAC[18]) increases (point a, Figure 2.4B). Consequently, the concentration of Ox decreases in the electrolyte adjacent to the electrode surface ($x = 0$), while the concentration of reduced species Red increases. At the point of maximum absolute current density (point b, Figure 2.4B), the concentration of Ox is close to zero and a sharp concentration gradient in the electrolyte of both species was built up. As the potential further decreases and time passes from point b to c, the diffusion layer thickness expands according to $\delta = \sqrt{\pi D t}$ in a quiescent

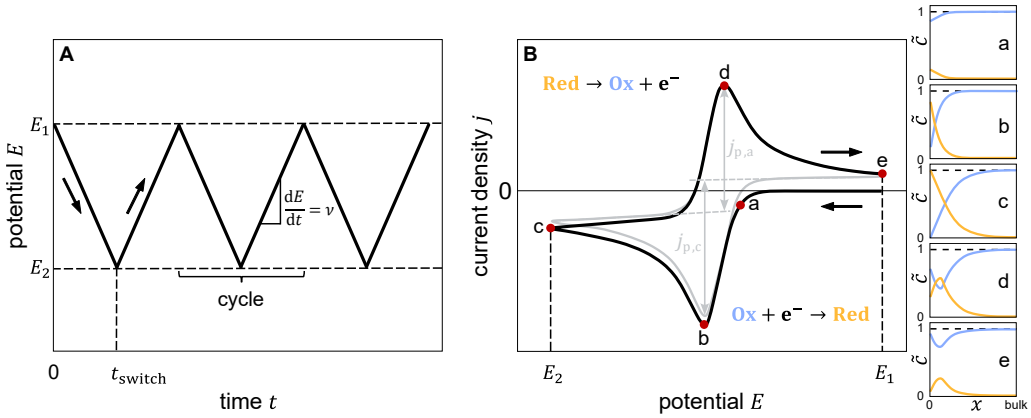

Figure 2.4: (A) Potential input over time for cyclic voltammetry as multiple linear sweep between E_1 and E_2 with the scan rate ν and (B) characteristic cyclic voltammogram for reversible reduction process with corresponding normalized concentration profiles (a-e) of oxidized species (blue) and reduced species (orange) with $\tilde{c} = c/c_{\text{Ox,bulk}}$ along the distance to the electrode surface x for the first cycle and cyclic voltammogram for the subsequent cycle (grey) with peak current densities $j_{\text{p,c}}$ and $j_{\text{p,a}}$. Assumptions: Diffusion coefficients of reduced and oxidized species are equal $D_{\text{Ox}} = D_{\text{Red}}$ and reduction is reversible. Adapted from Compton et al.[17].

electrolyte solution. This expansion causes a decrease in current density $j = zFD\frac{dc}{dx}|_{x=0}$. In this potential region, the reaction rate is significantly faster than the mass transport rate of reactive species, resulting in a diffusion-controlled reaction.
During the subsequent backward scan, the reduction reaction proceeds, albeit to a decreasing extent due to the increasing potential. Additionally oxidation of the reduced species begins to occur at more positive potentials. At point d, the anodic current reaches its maximum; a further increase in potential leads to a decrease in current density due to diffusion limitation, analogous to that observed in the forward sweep.
The cyclic voltammogram and the corresponding concentration profiles discussed specifically refer to the first cycle. In subsequent cycles, the CV differs from the first cycle (shown in gray in Figure 2.4B), as concentration profiles exhibit slight deviations. Here, the oxidation occurring in parallel reduces the cathodic currents during the forward sweep.
For reversible one-electron reactions, the distance between oxidation and reduction peaks, known as the peak-to-peak separation, serves as a key indicator of fast or slow charge-transfer kinetics. In cases of fast charge transfer, the diffusion of reactive species is limiting, and the voltammogram follows the Nernstian expression outlined above. This results in a peak-to-peak separation of 59 mV, independent of the scan rate, and a linear relationship between peak current j_p and $\nu^{1/2}$ described by Randles-Servcik expression (at 25 °C):

$$j_\mathrm{p} = 2.686e5\ [\mathrm{C\ mol^{-1}\ V^{-1/2}}]\ n^{3/2} A c_0 D^{1/2} \nu^{1/2}. \tag{2.32}$$

This expression can be used to determine the diffusion coefficient D.
Conversely, when charge transfer is slow and limits the system, the peak-to-peak separation increases with higher scan rates, and deviations from linearity appear in the plot of j_p versus $\nu^{1/2}$.
The degree of reversibility can be determined by comparing anodic and cathodic peak current densities. For fully reversible reactions, the absolute values of $j_{\mathrm{p,a}}$ and $j_{\mathrm{p,c}}$ are equal. In contrast, irreversible reactions, such as the electrochemical CO_2R, lack a reverse peak. A decrease in reversibility can also indicate a prior or subsequent chemical reaction (EC or CE), which usually leads to a high scan rate dependence of the CV.[18]
Cyclic voltammetry thus enables the determination of standard potentials, transport coefficients, and the degree of reversibility. Additionally, by observing peak shifts with varying scan rates, charge-transfer limitations can be identified in simple systems. However, for systems involving multiple-electron transfer reactions, competing reactions, additional chemical processes, or migration effects, interpreting CVs becomes significantly more complex and often requires simulative assistance.

Additionally, cyclic voltammetry can be used to investigate the electrical double layer by recording charge and discharge currents. This technique allows the determination of the double-layer capacitance at the electrolyte/electrode interface. To achieve this, the scan rates of the applied

potential sweeps are varied. When selecting the potential range of the sweep, it is essential to choose a region where only capacitive currents flow, avoiding any Faradaic currents. A potential difference of 100 mV between the upper and lower potentials is typically sufficient. To calculate the capacitance of a planar double layer C_{DL}, the charge equation for a plate capacitor can be applied. In the context of the EDL, the galvani potential $\Delta\phi$ can be described with the potential difference between the metal electrode and electrolyte $\phi_{\mathrm{M}} - \phi_{\mathrm{E}}$. Under the assumption of ideal electric and ionic conductivity, the potential E can be approximated as $E \approx \Delta\phi - \Delta\phi_{\mathrm{ref}}$ with $\Delta\phi_{\mathrm{ref}}$ as the potential drop at the reference electrode.

$$Q = C_{\mathrm{DL}}\Delta\phi = C_{\mathrm{DL}}(\phi_{\mathrm{M}} - \phi_{\mathrm{E}}) \approx C_{\mathrm{DL}}(E + \Delta\phi_{\mathrm{ref}}) \tag{2.33}$$

The definition of current as the change in charge over time, $I = \frac{\mathrm{d}Q}{\mathrm{d}t}$, leads to a linear relationship between current density and the scan rate, with the capacitance of the double layer as the slope by assuming a constant capacitance over time $\frac{\mathrm{d}C_{\mathrm{DL}}}{\mathrm{d}t} = 0$ and a constant potential drop at the reference electrode $\frac{\mathrm{d}\phi_{\mathrm{ref}}}{\mathrm{d}t} = 0$ (current-free reference electrode in a three-electrode configuration).

$$I = \frac{\mathrm{d}Q}{\mathrm{d}t} = (E + \phi_{\mathrm{ref}})\cancelto{0}{\frac{\mathrm{d}C_{\mathrm{DL}}}{\mathrm{d}t}} + C_{\mathrm{DL}}\frac{\mathrm{d}E}{\mathrm{d}t} + C_{\mathrm{DL}}\cancelto{0}{\frac{\mathrm{d}\phi_{\mathrm{ref}}}{\mathrm{d}t}} = C_{\mathrm{DL}}\frac{\mathrm{d}E}{\mathrm{d}t} = C_{\mathrm{DL}}\nu \tag{2.34}$$

The capacitance of the electrical double layer can be used to determine the electrochemically active surface area (ECSA) of non-planar electrodes, as the ECSA is assumed to be proportional to the double-layer capacitance. The proportionality factor is commonly referred to as the roughness factor RF, which is the ratio of the capacitance of the electrode under investigation to that of a planar electrode used as a reference.

In summary, cyclic voltammetry offers the ability to investigate electrochemical systems in a transient manner and in dependence on the scan rate. This enables in-depth analysis of reaction mechanisms[19, 20], impact of mass transport effects[21, 22], or processes in the electrical double layer[23].

2.2.3 Rotating disk electrode

In kinetic studies on a laboratory scale, controlling transport effects within the electrolyte is often desired to enable investigations of species transport. The rotating disk electrode setup enables this control. It consists of a disk of electrode material embedded into an insulating shaft, which is rotated at a defined frequency/rotation rate f in the electrolyte. The rotation creates a characteristic flow profile, the velocity profile of which was determined by Karmann and Cochran by solving the hydrodynamic equations under steady-state conditions. Qualitatively, the RDE entrains the adjacent electrolyte. At the same time, the centrifugal forces cause a radial flow outward from

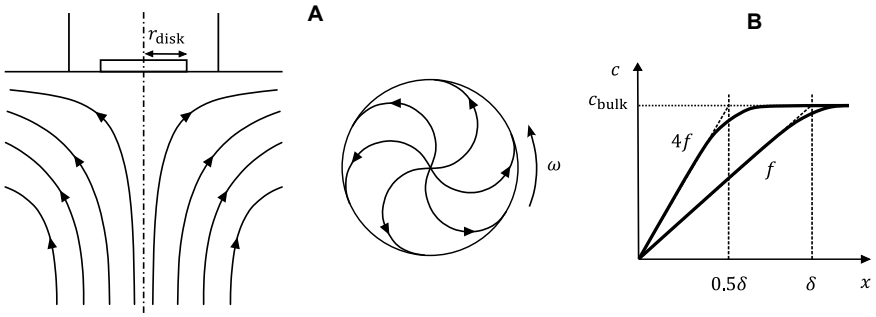

Figure 2.5: (A) Schematic streamlines of flow next to the rotating disk electrode and (B) concentration profile of the stagnant diffusion layer where a fourfold increase in rotation rate reduces the diffusion layer thickness by half. Aadapted from Bard et al.[9] and Compton et al.[17].

the center, while an axial flow towards the electrode compensates for the displaced electrolyte (Figure 2.5A). As a result, a stagnant hydrodynamic layer of constant thickness δ_{H} forms at the electrode surface:

$$\delta_{\mathrm{H}} = 3.6 \left(\frac{\nu_{\mathrm{kin}}}{\omega} \right)^{1/2}, \tag{2.35}$$

where ν_{kin} is the kinematic viscosity and ω the angular velocity. By combining this with the Nernst-Planck equation - including both convective and diffusive terms - in this boundary layer, Levich demonstrated that a constant mass transport rate occurs at the electrode surface, independent of the radial position. This characteristic is referred to as a uniformly accessible surface.[16] This creates a stagnant Nernst diffusion layer. The diffusion layer thickness can be calculated using Equation 2.36 and is easily adjustable by varying the rotation rate:[9]

$$\delta = 1.61 D^{1/3} \nu_{\mathrm{kin}}^{1/6} \omega^{-1/2}. \tag{2.36}$$

ω is related to the rotation rate f by $\omega = 2\pi f$ (Figure 2.5B).
The equations for the RDE are applicable within a range of ω values that maintain a stable, laminar boundary layer. If ω is too low, the thickness of the hydrodynamic layer may exceed the radius of the disk electrode r_{disk}, causing the assumption of a uniform layer to collapse. This results in a lower limit for ω, defined by the assumption that the r_{disk} need to be larger than δ_{H} $r_{\mathrm{disk}} > 3.6 \left(\frac{\nu_{\mathrm{kin}}}{\omega} \right)^{1/2}$. This combined with Eq. 2.35 results in

$$\omega > 10 \frac{\nu_{\mathrm{kin}}}{r_{\mathrm{disk}}^2}. \tag{2.37}$$

The upper limit is determined by maintaining a laminar flow profile, set with a Reynolds number below approximately 10^5.

$$Re = \frac{\omega r_{\mathrm{disk}}^2}{\nu_{kin}} < 10^5 \tag{2.38}$$

Assuming a kinematic viscosity of $1 \times 10^{-6}\,\mathrm{m^2\,s^{-1}}$ and an electrode radius of $r_{disk} = 2.5\,\mathrm{mm}$, the theoretical minimum rotation rate is around 15 rpm and maximum rotation rate around 1.5×10^5 rpm. However, roughness in the electrode surface or small bends in the RDE shaft cause turbulent flow to develop at lower rotation rates than calculated. Consequently, in practice, the rotation rate is often limited to $3000\,\mathrm{rpm}$.

2.2.4 Performance characteristics

The analysis of electrochemical systems reveals distinct performance characteristics that are optimized during the investigation of, e.g., catalyst materials, cell design, or operating conditions. Key targets include high activity, efficiency, and stability.

Current density and electrode potential

A high activity is typically characterized by high current densities, i.e., high turnover rates of the reactant at a given potential. Current density generally correlates linearly with the total electrochemical reaction rate per electrochemically active surface area (ECSA) of the electrode. The ECSA rarely equals the geometric surface area of electrodes and depends strongly on the surface roughness, surface morphology, or pore structure. However, current densities are often normalized to the geometric surface area for simplicity. This implies that current density can be increased by elevating the activity of a given catalyst site, but also by increasing catalyst loading or enhancing the roughness of the electrode surface.[24]
The current density in an electrochemical system cannot be analyzed in isolation; it is intrinsically linked to the electrode potential or the overall cell voltage. This interdependence is fundamental, as the applied potential drives the electrochemical reactions, governing the charge transfer rate and thus influencing the observed current density as is described in section 2.1.1 and 2.2.1.

Faradaic efficiency

Faradaic efficiency FE_i describes the percentage of the total consumed or produced charge that is used to produce a given product i:

$$\mathrm{FE}_i = \frac{Q_i}{Q_{\mathrm{total}}} \cdot 100\% = \frac{n_i \cdot z_i \cdot \mathrm{F}}{Q_{\mathrm{total}}} \cdot 100\% \tag{2.39}$$

with the charge Q_i stored in the product i, the total consumed charge Q_{total}, the amount n_i of product i in mole, the number of electrons z_i transferred to form product i, and the Faraday

constant F. Thus, the FE_i serves as a measure of charge selectivity of a catalyst to produce the desired product. A high FE also minimizes separation and purification costs in downstream processes.[25]

Energy efficiency

Energy efficiency (EE) of a cell is defined as the ratio between the energy stored in the desired product and the total energy input needed to produce it.[25] It can be calculated by

$$\mathrm{EE}_i = \frac{\Delta H_i^0}{\Delta G_i} \cdot \mathrm{FE}_i = \frac{E^0}{E_{\mathrm{ext}}} \cdot \mathrm{FE}_i = \frac{E^0}{E^0 + \eta} \cdot \mathrm{FE}_i \tag{2.40}$$

where ΔH_i^0 is the theoretical enthalpy change associated with the formation of product i,, ΔG_i is the corresponding Gibbs free energy change, E^0 is the standard potential of the reaction, and E_{ext} the applied potential, which differs from the standard potential due to overpotentials η. η generally arises from activation barriers associated with sluggish reaction kinetics, concentration overpotentials caused by mass transport limitations, and ohmic losses within the cell.

Stability

Catalyst and cell stability are essential to ensure sustained performance over hundreds of hours, with operational lifetimes of several thousand hours being desirable for industrial applications. This requirement implies that current density, cell voltage, FE, and, EE must be preserved under process conditions without a significant decline over operation time. Instability may arise from changes in the catalyst surface[26], dissolution of the catalyst[27], poisoning effects[28, 29], the introduction of impurities[30, 31], flooding of porous electrode structures[32], or degradation of other cell components[33].

2.3 Electrochemical CO_2 reduction

In this work, the electrochemical CO_2 reduction was investigated as the electrochemical system of interest. The electrochemical reduction of CO_2 enables the conversion of CO_2 into value-added chemicals. The reaction products and overall cell performance depend on several factors, s, including the catalyst material, electrolyte composition, electrode structure, cell configuration,

and process conditions. The following section provides an overview of the reaction system, the role of the electrolyte, and commonly used electrode and cell configurations in CO_2R.

2.3.1 Reaction system

In electrochemical CO_2 reduction, various catalyst materials are known, leading to multiple possible reaction pathways and products. In aqueous electrolytes, catalysts can be broadly categorized based on their primary products: 1) CO, 2) formic acid/formate ($HCOOH/HCOO^-$), or 3) hydrocarbons or alcohols, such as methane (CH_4), methanol (CH_3OH), ethanol (C_2H_5OH), and ethylene (C_2H_4) (Figure 2.6).[34, 35]. The corresponding reaction equations in acidic electrolytes are

$$CO_2 + 2\,H^+ + 2\,e^- \longrightarrow CO + H_2O \tag{2.41}$$

$$CO_2 + 2\,H^+ + 2\,e^- \longrightarrow HCOOH + 2\,H_2O \tag{2.42}$$

$$n CO_2 + m H^+ + m e^- \longrightarrow C_nO_{2n+p-m}H_{2p-m} + p H_2O \tag{2.43}$$

and in alkaline electrolytes

$$CO_2 + H_2O + 2\,e^- \longrightarrow CO + 2\,OH^- \tag{2.44}$$

$$CO_2 + 2\,H_2O + 2\,e^- \longrightarrow HCOOH + 2\,OH^- \tag{2.45}$$

$$n CO_2 + p H_2O + m e^- \longrightarrow C_nO_{2n+p-m}H_{2p-m} + m OH^-. \tag{2.46}$$

The reaction mechanism of the multi-reduction sequences in CO_2R is not fully understood and contradictory opinions persist. For example, either an electron transfer (ET) to a CO_2 radical anion or a proton-coupled electron transfer (PCET) to *COOH is assumed to be the rate-determining step for CO_2R at Au, Ag, and Ni catalysts.[36–38] In this thesis, and in agreement with a widely accepted view, ET - forming the radical anion $CO_2^{-\bullet}$ - is considered the rate-determining step at bulk metal electrodes in neutral and alkaline aqueous electrolytes for C_1 products.[38, 39]
Au and Ag as a catalyst exhibit high Faradaic efficiency for CO production, along with excellent stability and activity. This is attributed to the weak binding of protons and CO at surface sites, which prevents further reduction of CO and suppresses the hydrogen evolution reaction (HER).[34]

$$2\,H^+ + 2\,e^- \longrightarrow H_2 \tag{2.47}$$

$$2\,H_2O + 2\,e^- \longrightarrow H_2 + 2\,OH^- \tag{2.48}$$

The HER occurs in the same potential window as CO_2R, making it a competing parasitic reaction. Therefore, it is crucial to suppress this reaction through the careful selection of catalysts and

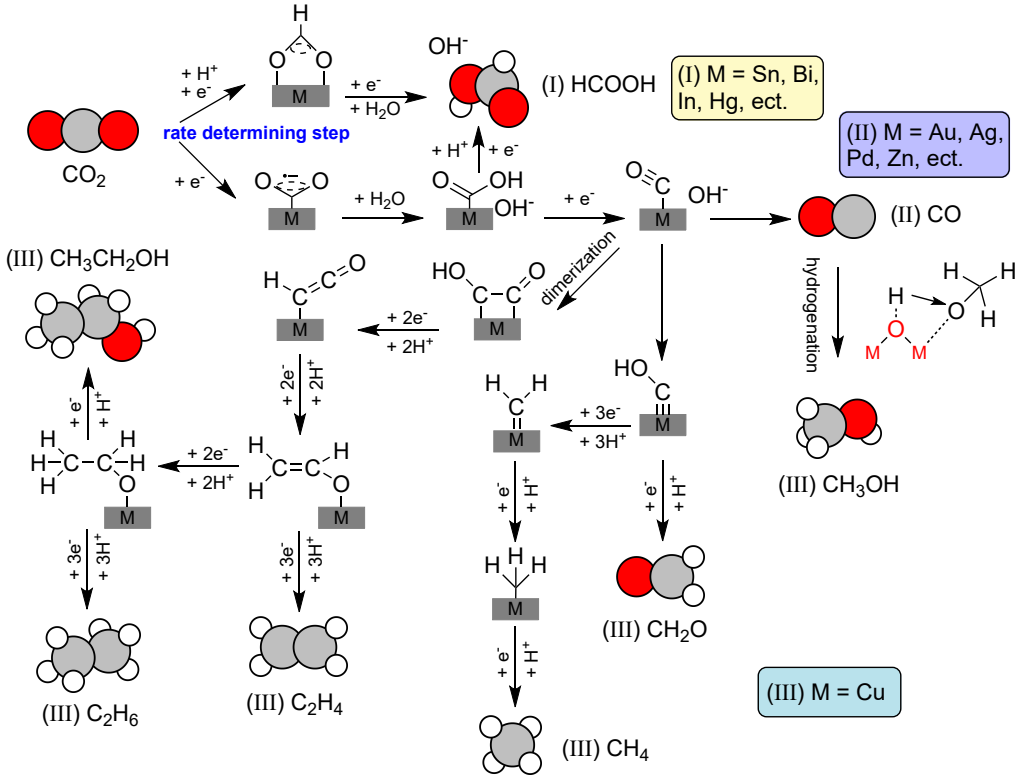

Figure 2.6: Schematic mechanism of electrochemical CO_2 reduction at different metal catalysts in aqueous, alkaline electrolyte solution. Adapted from Ahsaine et al.[40] licensed under CC BY 4.0.

electrolytes. Certain metals, such as Fe, Ni, Pd, and Pt, predominantly produce H_2 due to their strong hydrogen adsorption affinity and lack of CO_2 adsorption under negative potentials.[34] Metals like Sn, Bi, and In mainly produce formic acid (HCOOH) in a $2\,e^-$-reduction, or more precisely formate ($HCOO^-$), which predominates at pH values above 3.75.[41] Small quantities of formate are also detected on Ag electrodes at more negative potentials.[42, 43]

So far, copper is the only metal catalyst known to produce multi-carbon (C_{2+}) products and alcohols via CO_2 reduction (Eq. 2.46). This makes copper an outstanding catalyst with a high potential for valuable chemical production. However, its low Faradaic efficiency to a single product, the instability of single facets on the Cu-catalyst surface resulting in a change in selectivity, and a complex reaction mechanism make it a challenging catalyst for CO_2R.[44, 45]

In addition to bulk metal catalysts, a wide range of materials has been explored for CO_2R, including metal nanoparticles[46, 47], metal oxides[48], single atoms[49], carbon-based materials[50], porphyrins[51], and metal organic frameworks[52]. The various strategies for incorporating these catalyst materials into electrochemical cells as electrode structures are discussed in section 2.3.3.1.

2.3.2 Aqueous electrolyte for CO_2R

In addition to the choice of catalyst material, the selection of the electrolyte is crucial in CO_2R. It provides ion exchange between electrodes to complete the current circuit. Therefore, the electrolyte must exhibit high ionic conductivity, good solubility for reactants, and ease of handling. Electrochemical CO_2 reduction is conducted in various solvents, including aqueous, organic[53, 54], and ionic liquid electrolytes[55], each offering distinct advantages and disadvantages. Water-based systems with inorganic salts are commonly used in CO_2R due to good availability and environmental friendliness of water. However, water is not electrochemically inert in the applied potential window because the HER occurs concurrently, potentially decreasing the Faradaic efficiency. Nevertheless, the benefits of water as a solvent motivatecontinued investigation and optimization. Early studies of water-based electrolytes have shown that the electrolyte plays a significant and complex role in CO_2R .[56, 57] The electrolyte affects local pH through buffering and chemical reactions, and both anions and cations may modify reaction kinetics and the electric field near the electrode. These aspects are discussed in the following sections.

Dependency on pH

The pH dependency of electrochemical CO_2R is significant because pH alters system performance strongly. This arises from the involvement of protons and hydroxide ions in both the CO_2 reduction and hydrogen evolution reaction, as well as the carbonate reactions when CO_2 dissolves in water. The dependency of HER and CO_2R kinetics on pH is not entirely straightforward due to overlapping effects.

It is widely assumed that higher pH values kinetically suppress HER.[58] Bondue et al.[58] suggest that the pH dependency of HER arises from the transition from proton reduction (Eq. 2.47) to water reduction (Eq. 2.48) as pH increases. At low pH, HER proceeds predominantly via proton reduction, while at higher pH, proton depletion suppresses this pathway.[59] Beyond this point, water reduction dominates HER, requiring higher overpotentials and exhibiting slower kinetics, which explains the decrease in HER activity at higher pH. Ooka et al.[60] reported that above pH 2.5, proton reduction is already transport-limited and negligible, with water reduction becoming the primary pathway. Compared to proton reduction, water reduction shows weaker pH dependence. Although the equilibrium potential shifts with pH on the SHE scale according to the Nernst equation, H_2O concentration as proton donor remains effectively constant across the pH range. Combined with sluggish kinetics, this results in weak overall pH dependency of water reduction, and consequently of HER under neutral and alkaline conditions.[61]

The CO production pathway of CO_2R exhibits pH-invariant kinetics on the SHE scale in most studies. This supports the assumption that the rate-limiting step is CO_2 adsorption, which does not involve a proton donor (H^+/H_2O).[62, 63] However, pH affects the availability of CO_2 in aqueous electrolytes through water dissociation (Eq. 2.49) and carbonation reactions (Eq. 2.50 and 2.51):

$$H_2O \overset{r_w}{\rightleftharpoons} H^+ + OH^- \tag{2.49}$$

$$CO_2 + OH^- \overset{r_{c1}}{\rightleftharpoons} HCO_3^- \tag{2.50}$$

$$HCO_3^- + OH^- \overset{r_{c2}}{\rightleftharpoons} CO_3^{2-} + H_2O \tag{2.51}$$

At higher pH, CO_2 converts to bicarbonate and carbonate, reducing its availability in solution (Figure 2.7). However, carbonate electrolytes can potentially release CO_2 because the carbonation reactions are reversible. The equilibrium position of the carbonate species depends on temperature and salt content, both of which decrease the CO_2 concentration at higher values (Figure 2.7).[64] The reaction rate constants for carbonation reactions are commonly derived from seawater analyses.[65, 66] In CO_2R, the carbonate reactions are strongly influenced by the

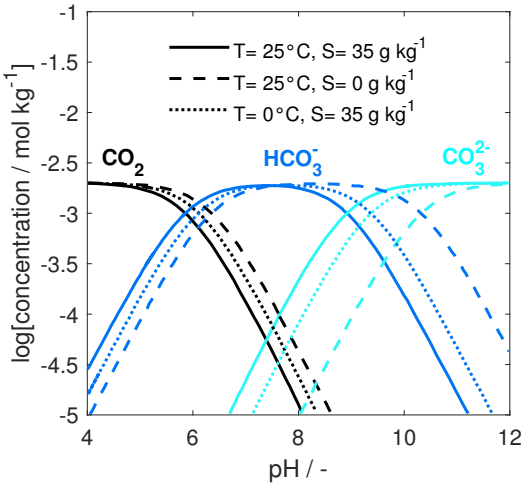

Figure 2.7: Concentrations of CO_2, HCO_3^-, and CO_3^{2-} at reaction equilibrium in seawater as a function of temperature and salinity S. The decrease in CO_2 solubility due to the higher salt content is neglected here. Adapted from König et al.[64].

production of hydroxide ions and contribute to the local pH. A characteristic measure that sets electrochemical against chemical consumption of CO_2 is the so-called carbon efficiency CE:

$$\mathrm{CE} = \frac{\dot{n}_{\mathrm{CO_2,elchem}}}{\dot{n}_{\mathrm{CO_2,elchem}} + \dot{n}_{\mathrm{CO_2,chem}}}. \tag{2.52}$$

CE quantifies the proportion of CO_2 consumed electrochemically, relative to the total CO_2 consumption (electrochemical and chemical).

Thus, the pH dependency of CO_2R and HER is a complex interplay of reactions and transport involving protons, hydroxide ions, and carbonate species, where higher pH generally suppresses hydrogen evolution reactions while decreasing CO_2 availability through carbonation reactions. Additionally, the apparent pH-dependencies also vary with the applied potential because more negative potentials accelerate reaction rates, induce mass-transport limitations, and lead to an increase of the local pH near the electrode surface. Building on this understanding, anions introduced by the electrolyte salt further impact the reaction system, as discussed in the following section.

Anion effects

Changing the anion or its concentration in the electrolyte affects CO_2R through several mechanisms: (1) by buffering and local pH regulation, (2) by proton donation for HER, and (3) by specific anion adsorption that alters reaction kinetics of CO_2R and HER.
The effect of anions on CO production appears to arise mainly from the buffering capacity of the electrolyte. Buffering anions such as bicarbonate neutralize hydroxide generated at the electrode surface, thereby suppressing the chemical conversion of CO_2 to carbonate and maintaining a higher local CO_2 concentration available for the electrochemical reaction.[67]
A stronger influence of the anion is observed for H_2 and CH_4 production when non-buffering electrolytes such as K_2SO_4 and KCl are compared with buffering electrolytes such as $KHCO_3$ and K_2HPO_4.[68–70] While the current density of these reactions remains constant in non-buffering electrolytes, the reaction rate in buffering electrolytes was found to increase with stronger buffers, achieved either through higher concentration or a higher buffer strength (HCO_3^- < H_3BO_3 < HPO_4^{2-}).[68] This is attributed to HPO_4^{2-} and HCO_3^- donating protons, which promote HER.[69, 70]

$$\mathrm{HCO_3^-} \rightleftharpoons \mathrm{H^+ + CO_3^{2-}}, \quad pK_\mathrm{a} = 10.33 \tag{2.53}$$

$$\mathrm{B(OH)_3 + H_2O} \rightleftharpoons \mathrm{H^+ + B(OH)_4^-}, \quad pK_\mathrm{a} = 9.23 \tag{2.54}$$

$$\mathrm{H_2PO_4^-} \rightleftharpoons \mathrm{H^+ + HPO_4^{2-}}, \quad pK_\mathrm{a} = 7.21 \tag{2.55}$$

However, the role of anions as a significant proton source is only relevant at more positive potentials ($\approx -0.4\,\mathrm{V}$ vs. reversible hydrogen electrode, RHE) or higher electrolyte concentrations ($>0.1\,\mathrm{M}$). There are also indications that a stronger physisorption of anions at the catalyst surface is associated with more favorable CO_2R kinetics by modifying the local electric field and stabilizing reaction intermediates.[71]

Overall, anion identity and concentration influence CO_2R through buffering, proton donation, and specific adsorption. In addition to the effects of the anions, the cations of the electrolyte salt also significantly influence the product distribution of the CO_2R.

Cation effects

Electrolyte cations influence current density and product distribution. Although the exact mechanisms remain under investigation, cation effects are commonly attributed to cation hydrolysis and intermediate stabilization.

Studies show that increasing the size of alkali metal cations ($Li^+ < Na^+ < K^+ < Rb^+ < Cs^+$) leads to higher current density of CO_2R at a fixed potential on metal electrodes and an increased Faradaic efficiency for C_2 products at copper electrodes.[57, 72] Early hypotheses suggested cation adsorption at the electrode surface, thereby altering the potential profile in the electrical double layer according to Frumkin's theory.[57] However, this hypothesis is now considered unlikely, as Mills et al.[72] showed that the adsorption potential of alkali cations on transition metal electrodes is around $-2.4\,\mathrm{V}$ vs. NHE.[72, 73] Instead, Singh et al.[73] matched the observation of cation impact with a simulation study suggesting the hydrolysis of cations as a reason for the effect. Hydrolysis of a metal cation refers to the deprotonation of a water molecule coordinated to the metal ion M^+ due to solvation, releasing a proton into solution (Eq. 2.56).

$$[\mathrm{M^+(H_2O)}_n] \rightleftharpoons [\mathrm{MOH(H_2O)}_{n-1}] + \mathrm{H^+} \tag{2.56}$$

Larger cations have lower pK_a of this reaction. This implies that larger cations can provide protons through dehydration at the electrode, which then react with electrochemically produced hydroxide ions near the electrode. This buffering effect decreases the local pH value and increases the CO_2 concentration near the electrode by preventing the shift of carbonation reactions towards HCO_3^- and CO_3^{2-}.[73]

Another hypothesis is that larger cations may stabilize intermediates of CO_2R through stronger electric fields[74] or stronger electrostatic interactions[75]. This stabilization reduces the adsorption energy of adsorbed CO_2 species, thereby increasing the reaction rate of CO_2R.

2.3.2.1 Salt precipitation

Another effect that is strongly governed by the choice of electrolyte is salt precipitation. At higher current densities, carbonate concentrations rise due to reaction of CO_2 with hydroxide ions, while local cation concentrations increase via migration. If solubility limits are exceeded, salts precipitate, especially at the gas-liquid interface within porous electrodes:

$$\mathrm{HCO_3}^{2-}{}_{(\mathrm{aq})} + \mathrm{M}^{+}_{(\mathrm{aq})} \rightleftharpoons \mathrm{MHCO_{3(s)}} \tag{2.57}$$

$$\mathrm{CO_3}^{2-}{}_{(\mathrm{aq})} + 2\,\mathrm{M}^{+}_{(\mathrm{aq})} \rightleftharpoons \mathrm{M_2CO_{3(s)}} \tag{2.58}$$

Salt precipitation blocks gas-transport pathways and covers electrochemically active catalyst surfaces, all of which result in a decline of performance during operation time.
Strategies to mitigate salt deposition aim to minimize the (local) concentrations of cations, anions, and the precipitating salt itself.[76] In addition to active strategies such as dynamic electrolyte pulsing[77, 78] or potential pulsing[79] during operation (not discussed further here), the electrolyte composition itself can exert a major influence on salt precipitation. This includes both the electrolyte salt concentration and the identity of the cation. Lower electrolyte concentrations have been found to improve the long-term stability of CO_2R, but they also cause significantly higher ohmic losses due to reduced ionic conductivity.[80, 81] Thus, the choice of electrolyte salt concentration involves a trade-off between cell potential and cell lifetime.
With respect to the cation identity, the solubility of the corresponding carbonates and bicarbonates is decisive. Solubility increases with cation size: $Na^+ < K^+ < Cs^+$.[76, 81] This makes Cs^+, together with observations of enhancements in reaction rate of CO_2R through hydrolysis, increasingly attractive as an electrolyte cation. Nevertheless, K^+ in the form of KOH or $KHCO_3$ remains the most widely used electrolyte salt in CO_2R owing to its good solubility, far greater availability compared to cesium salts, and ease of handling.

Overall, the microenvironment is strongly influenced by the electrolyte system. The choice of electrolyte affects performance due to the impact on local pH, CO_2 availability, and kinetic barriers of both CO_2R and HER. This highlights the importance of electrode and cell design, which together define the actual reaction conditions.

2.3.3 Electrode and cell design

Electrode structure and cell design play a critical role in overall system performance, as they govern key parameters such as catalyst accessibility, transport processes, and effective electrical

and ionic conductivity. Depending on the research focus, various electrode and cell configurations are employed in studies and scale-up of electrochemical CO_2 reduction.

2.3.3.1 Electrode structures

Beyond the choice of catalyst material, the way it is incorporation into the cell - namely, the electrode structure - has a decisive impact on performance. Common electrode types in CO_2R can be categorized into three main classes: planar electrodes, porous electrodes, and gas diffusion electrodes.[82]

Planar electrodes These electrodes are most commonly used in CO_2R, primarily for catalyst screening and fundamental kinetic studies.[67, 83, 84] They are typically made of bulk catalyst materials, such as metal foils, which makes them simple in design and easy to integrate into electrochemical cells (Figure 2.8A). Introduced in either batch or flow cells, planar electrodes are entirely immersed in a CO_2-saturated liquid electrolyte. The simplicity of planar electrodes makes them suitable for investigating catalyst-electrolyte interactions and for the initial evaluation of catalyst activity, product selectivity, and stability. However, their current densities are limited due to significant mass transport constraints and the relatively low ECSA.

Porous electrodes Porous electrodes are designed to increase the ECSA and thereby enhance total current density (Figure 2.8B).[85, 86] The three-dimensional pore structure allows for higher electrochemical production rates and facilitates the detection of trace products. However, this added complexity due to new transport and reaction phenomena, including elevated local current densities, concentration and potential gradients within the electrode, and multiphase flow involving pores, product gas bubbles, and electrolyte. While this makes the electrode more representative of technically relevant designs, it also renders its interpretation more complex and causes performance to become highly sensitive to structural parameters such as electrode thickness, porosity, and pore diameter. Furthermore, these electrodes are stronger affected by transport limitations due to high reaction rates combined with poor CO_2 availability.

Gas diffusion electrodes[1] To further improve CO_2 availability, gas diffusion electrodes (GDEs) are incorporated into CO_2R cells. In GDEs, gaseous CO_2 is supplied from one side of the electrode, while the electrolyte is delivered from the opposite side. This configuration creates a high three-phase boundary between gas, electrolyte, and catalyst within the porous

[1] Parts of this section have been published in Dorner et al., J. CO2 Util., 2025 [87]

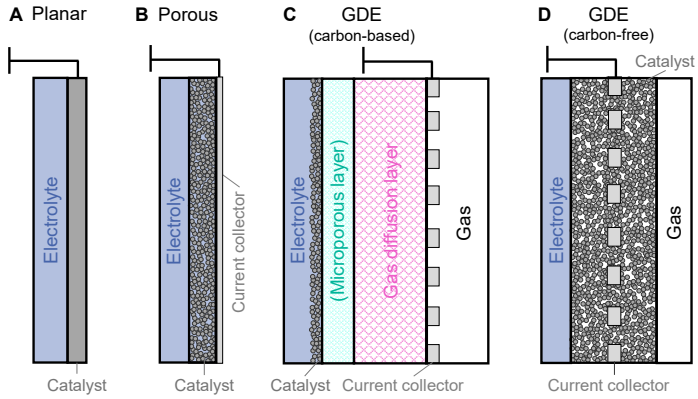

Figure 2.8: Electrode structures for electrochemical CO_2 reduction: (A) planar electrode, (B) porous electrode, and (C) carbon-based and (D) carbon-free gas diffusion electrode. Adapted from Ampelli et al.[82].

electrode structure. This design significantly shortens the diffusion distance of CO_2, allowing for high current densities exceeding $200\,\mathrm{mA\,cm^{-2}}$, while maintaining high Faradaic efficiencies for targeted products.

Commonly studied GDEs in CO_2R comprise a carbon-based gas diffusion layer (GDL), optionally coated with a hydrophobic microporous layer (MPL), and an overlying porous catalyst layer (CL) that is in contact with the electrolyte (Figure 2.8C).[82, 88] The catalyst layer, normally just a few nanometers thick, provides the ECSA. The MPL, typically made of carbon black and polytetrafluoroethylene (PTFE) particles, minimizes electrical contact resistance between GDL and catalyst layer, and creates a hydrophobic barrier to prevent complete electrode flooding by the electrolyte. The GDL supplies mechanical support and a macroporous structure for gas transport, while its hydrophobic PTFE coating prevents flooding by the liquid electrolyte.

However, these carbon-based electrodes face significant stability issues for CO_2R applications due to susceptibility to flooding.[89] Moreover, studies in literature were carried out with many different GDLs, which differ in terms of the carbon structure, thickness, porosity, etc. This makes a systematic comparison difficult.[88]

Besides using GDLs based on metal,[90, 91] PTFE,[92] or membranes,[93] carbon-free silver GDEs without a separate GDL can be used for CO_2 reduction. The latter electrodes are known from commercial use for the oxygen reduction reaction (ORR) in chlor-alkali electrolysis. They consist of a porous structure made from a mixture of Ag catalyst particles and PTFE binder coated on a metal mesh, which serves as a current collector and mechanical support (Figure 2.8D). PTFE, with a typical mass content ranging from $1\,\mathrm{wt\%}$ to $10\,\mathrm{wt\%}$, serves to adjust hydrophobicity. The catalyst loading ranges between $140\,\mathrm{mg\,cm^{-2}}$ and $250\,\mathrm{mg\,cm^{-2}}$ for electrode thicknesses of around $200\,\mu\mathrm{m}$ to $400\,\mu\mathrm{m}$. These carbon-free Ag-GDEs are slightly more expensive due to higher catalyst loading but offer a high electrochemically active surface area and demonstrate excellent

lifetime in ORR[94] and in CO_2R[6, 95, 96]. They are used in the GDE study presented in this thesis (Chapter 5).

2.3.3.2 Cell configurations

Beside variations in electrode structures, a range of cell setups can be used for CO_2R. The choice depends on various factors, including feasibility, scale, energy efficiency, and process conditions. To complete the cell setup, an anode and a suitable counter reaction are required. The most commonly used anodic reaction in CO_2R studies is the oxygen evolution reaction (OER), typically catalyzed by platinum, iridium oxide, or dimensionally stable anodes (e.g., IrRuOx on Ti). The spatial arrangement of the anode and cathode is also a critical design consideration in the cell design, as it influences transport processes, potential distribution, and overall cell efficiency.
Cell configurations can be broadly classified into four main types, each with distinct characteristics: batch cell, liquid-phase flow cell, membrane electrode assembly (MEA) cell, and solid oxide electrolyzer cell (SOECs) (Figure 2.9). In this work, batch and flow cells are employed, while MEA and SOEC configurations are included here for completeness.

Batch cell The batch cell is one of the most commonly used laboratory-scale configurations for electrochemical CO_2. Its popularity stems from its simple and rapid setup, making it highly suitable for catalyst screening. Both undivided and divided setups exist. The catalyst is generally provided as bulk material or deposited on supports such as carbon paper or glassy carbon (planar or porous electrode). The electrolyte is continuously purged with CO_2 gas to maintain saturation (Figure 2.9A). In some cases, GDEs are integrated into batch cells.[98]
In the divided cell setup or H-cell, a porous glass frit or ion exchange membrane separates the anodic and cathodic compartments, preventing the reoxidation of reduction products (Figure 2.9A2). A key limitation of batch cells is the low solubility of CO_2 in aqueous electrolytes (≈33 mM) combined with long diffusion paths, which restricts current densities to less than $100\,\mathrm{mA\,cm^{-2}}$. Additionally, the large electrode spacing typical of classical H-cells contributes to high overpotentials and reduced energy efficiency.
In summary, batch cells are well-suited for catalyst characterization and product analysis on a laboratory scale. For industrial applications and large-scale processes, different cell concepts with a focus on higher current densities and better energy efficiency are required.

Liquid-phase flow cell The liquid-phase flow cell is characterized by the continuous convective flow of liquid electrolyte within the cell, facilitating the transport of reactants and products to and from the catalyst surface.[99] In this configuration, CO_2 is supplied to the cathode via

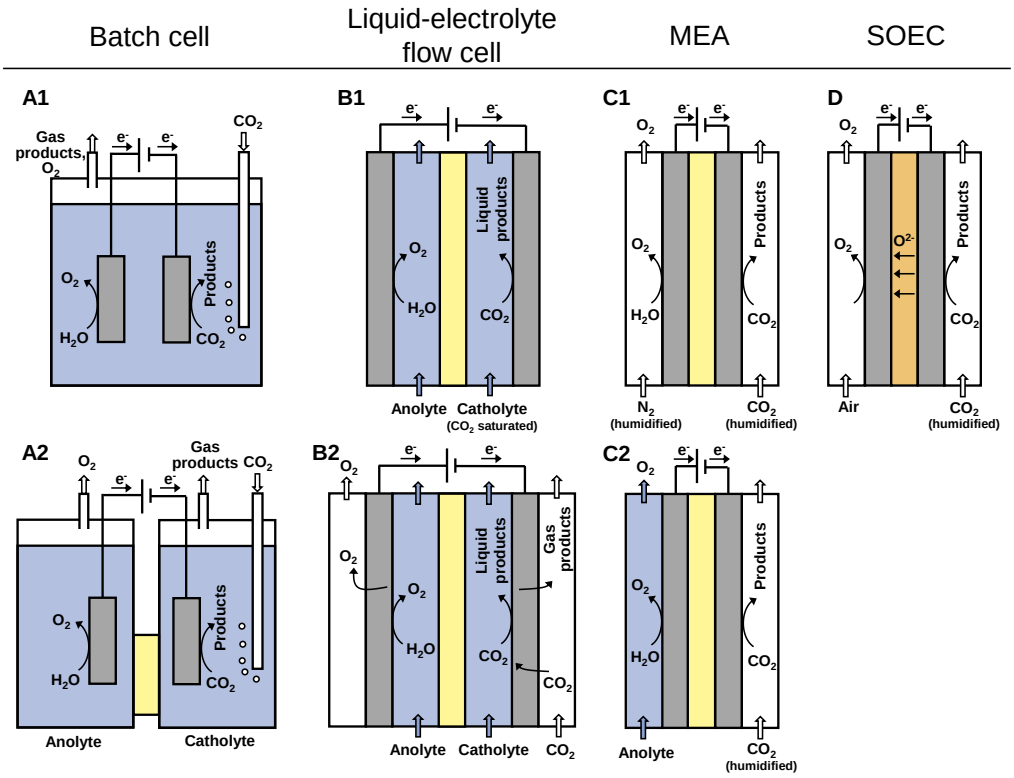

Figure 2.9: Cell configurations for electrochemical CO_2 reduction: (A1) undivided batch cell (A2) divided batch cell (H-cell), (B1) liquid-electrolyte flow cell where CO_2 is provided dissolved in liquid catholyte, (B2) liquid-electrolyte flow cell with anodic and cathodic gas diffusion electrode, where CO_2 is fed by CO_2 gas flow, (C1) full-MEA setup with humidified gas feeds, (C2) exchange-MEA setup with liquid anolyte side, and (D) solid-oxide electrolyzer cell. Adapted from Kibria et al.[97].

dissolution in the catholyte (Figure 2.9B1).[100] The reaction and transport processes are therefore similar to those in an H-cell, as CO_2 is introduced through the liquid phase. However, the flow cell provides the additional benefit of forced convection, which reduces the hydrodynamic diffusion layer at the electrode surface. This enhanced mass transport of CO_2 results in improved Faradaic efficiency.

For technical applications, gas diffusion electrodes are integrated into the flow cell (Figure 2.9B2). Here, gas and liquid electrolyte streams are supplied separately from opposite sides of the electrode. Differential pressure between catholyte and CO_2 gas side must be carefully controlled to avoid flooding and electrolyte intrusion, which can significantly impact cell performance.[101]

Membrane electrode assembly cell MEA cells, also called electrolyte-less or zero-gap cells, replace liquid electrolyte reservoirs with a polymer membrane, minimizing overpotentials associated with ionic conductivity. Depending on the design, liquid electrolyte compartments may still be present.[102]
In full-MEA setups, liquid electrolytes are completely omitted (Figure 2.9C1).[103–105] IProper humidification of the polymer membrane is essential to maintain ionic conductivity and performance. Additionally, cations play a critical role in stabilizing reaction intermediates, enhancing catalytic activity. These requirements make the full-MEA design particularly challenging.
TExchange-MEA designs retain a liquid anolyte while removing the catholyte (Figure 2.9C2) or vice versa.[93] This results in a wide range of possibilities for the design of MEA setups, all of which try to combine low cell voltages and compact cell designs with a suitable microenvironment for CO_2R.

Solid oxide electrolyzer cell SOECs operate at high temperatures of 600–800 °C, where the solid oxide membrane conducts oxygen ions (O^{2-}) generated by the cathodic CO_2 reduction reaction [106]:

$$CO_2 + 2\,e^- \longrightarrow CO + O^{2-}. \tag{2.59}$$

These ions migrate through the membrane to the anode, where they combine and react to form molecular oxygen (Figure 2.9D). The elevated temperatures in SOECs enable high reaction rates and substantial current densities, offering promising performance in CO_2 electroreduction.[107]
However, the SOEC setup faces significant challenges, namely high capital costs, cell degradation over time, and the limitation to C_1 products, primarily CO.[108]
In the field of high-temperature SOECs, co-electrolysis is an approach in which water and CO_2 are simultaneously reduced to produce syngas, most commonly using nickel-based catalysts.[109]
At these high temperatures, the chemical reverse water-gas shift reaction (RWGS) contributes to the CO formation.

$$H_2 + CO_2 \underset{\text{WGS}}{\overset{\text{RWGS}}{\rightleftharpoons}} H_2O + CO \tag{2.60}$$

The balance between electrochemical CO_2 reduction and RWGS depends strongly on catalyst, temperature, cell potential, electrode thickness, and other parameters, and remains under active investigation.[110]

Overall, simple setups such as batch and liquid-phase flow cells remain indispensable for the laboratory-scale characterization of catalyst-electrolyte systems of CO_2R typically operating at current densities up to $100\,mA\,cm^{-2}$. Industrial benchmarks require current densities above $200\,mA\,cm^{-2}$, long-term stability up to 10,000 h, and consistently high Faradaic efficiency.

Flow cells with integrated GDEs and silver catalysts already achieve $300\,\mathrm{mA\,cm^{-2}}$, 95% FE, and 1500 h operation in individual cases.[95, 111] MEA configurations are particularly promising for reducing ohmic losses and improving energy efficiency, with demonstrated stability of 4380 h at intermediate current densities of 50 up to $200\,\mathrm{mA\,cm^{-2}}$.[80, 112].

2.3.4 Modeling of CO_2 reduction

Given the complexity of reaction mechanisms, their interplay with species transport and local conditions, and the diversity of electrode and cell configurations, modeling CO_2 reduction is an invaluable tool. It enables reproducing system behavior, gaining a deeper understanding, and identifying both limitations and opportunities of CO_2R systems.
Depending on the specific focus, existing models vary in the processes implemented and the modeling domains they represent. The primary model types on macroscopic scale and some representative studies are summarized below (Table 2.1). Note that this overview is not intended to be exhaustive.

The first model for CO_2R was developed by Gupta et al.[113], who simulated planar silver and copper electrodes.[113] This reaction-diffusion model incorporates electrochemical reactions, the carbonate reaction system, and diffusive transport within the liquid diffusion layer. These macrokinetic models are widely used and often adapted to explore specific research aspects, such as electrode morphology[114, 115] or buffering capacity[67]. To accurately simulate the distribution of carbonate species in the liquid diffusion layer and assess electrolyte buffering effects, it becomes essential to include the migration of charged species to account for electric field impacts and to ensure electroneutrality. All these models have in common that they treat the electrical double layer as a simple potential drop at the electrolyte/electrode interface, without resolving local details within this region. They also generally use lumped reaction equations to describe the electrochemical reactions, prioritizing transport and its limitations over detailed reaction mechanisms.
Microkinetic models also play a significant role in CO_2R research, as they include intermediates in the reaction mechanism of CO_2R. These models enable the identification of most plausible reaction pathways for CO_2R at bulk electrodes[116, 117] and nanostructured electrodes[118], as well as the characterization of adsorbed species interactions in relation to surface coverage[37]. Kinetic parameters for these models, i.e., Gibbs free energies of adsorption and activation, are often derived from density functional theory (DFT) calculations, which constitute a separate, huge field of CO_2 reduction modeling.[119] However, DFT models generally do not account for mass transport processes, so they are not included in this overview in detail.
Another class of models considers the electrical double layer (EDL) by locally resolving ion concentration profiles. The electric potential generated by the electric field in this region can be

described by Poisson's equation (detailed information in section 2.1.2.2). This equation captures charge separation in the EDL, which typically has a thickness of around 1 to 10 nm. When coupled with the Nernst-Planck equation for ion transport, these approaches are known as Poisson-Nernst-Planck models. A prominent modification is the Generalized Modified Poisson-Nernst-Planck approach, which considers the steric effect of ions.[23, 62, 120] These EDL-models provide insights into double-layer charging and discharging behavior[23], the local reaction environment[62, 120], and the impact of cation concentration and interactions at the electrode/electrolyte interface[121]. However, because these models have the smallest length and time scales of continuum-transport models, they are computationally demanding.

All the models discussed so far simulate processes at relatively planar electrodes. However, similar modeling approaches are also applied to porous and gas diffusion electrodes. The first simulation model was introduced by Li et al.[122], who modeled CO_2R in a trickle-bed reactor, already including mass transport effects along the reactor height. Despite this, the model remained crude, as it did not account for the spatial distribution of current or potential.[122] Additionally, early models assumed that electrochemical reactions occur solely at the triple-phase boundary.[116, 122, 123] However, this assumption does not hold in CO_2R systems, as experimentally observed, high current densities cannot be simulated under this condition.[124] A prominent and comprehensive model for GDEs in CO_2R was developed by Weng et al.[125]. This model simulates a carbon-based GDE, incorporating a microporous and macroporous gas diffusion layer alongside a catalyst layer, and includes gaseous and liquid transport at a macroscopic scale.[125] The fraction of flooded pores in the catalyst layer is described by the saturation S, where the dependence between saturation and capillary-pressure (saturation curve) is adapted from fuel-cell GDEs.[126] The effective thickness of the resulting thin-film d_{tf} is calculated by geometrical derivation according to

$$d_{\mathrm{tf}} = r_{\mathrm{p,CL}}(1 - 1\sqrt{1 - S}) \tag{2.61}$$

with $r_{\mathrm{p,CL}}$ as the pore radius in the catalyst layer. This results in an approximate liquid transport distance for CO_2 of around $10\,\mathrm{nm}$ for ideally wetted GDEs.

Modifying the electrode structure of a GDE also alters mass transport and local conditions within the electrode, necessitating further model development for alternative GDE designs, such as carbon-free GDEs. A stationary model based on the thin-film flooded agglomerate (TFFA) approach was developed by Löffelholz et al.[127], adapted from application in oxygen depolarized cathodes.[127, 128] In this model, the reaction zone consists of cylindrically shaped, flooded agglomerates surrounded by a thin-film and gas pores of a defined radius. Using this approach, the impact of electrolyte concentration and gas feed concentration are evaluated. Findings show that these electrodes face significant limitations due to CO_2 mass transport at high current densities and from chemical consumption of CO_2. A dynamic model including the effect of electrowetting on these electrodes was also developed.[129] This model calculates the local saturation of the GDE

using the Leverett approach[130, 131], taking into account the potential-dependent contact angle of silver, which influences the amount of electrolyte in the GDE.

Beyond the diversity of electrode materials and designs, differences in cell configurations also play a critical role in determining transport processes within the system. Models for these systems are often extended to include transport through the membrane and the anode reaction. This enables, e.g., the comparison of potential losses in the full cell, which significantly determines the cell's overall energy efficiency.[132] The development of membrane-electrode assemblies has made understanding the transport of charged species within the membrane and cross-flow effects essential. Weng et al.[102] simulated and compared full-MEA and exchange-MEA configurations (liquid anode feed; see Figure 2.9C1 and C2) revealing distinct limitations for each setup: full-MEA configurations suffer from membrane dehydration, while exchange-MEA configurations are more affected by salt deposition and flooding issues.[102]

Bree et al.[133] further developed a modular model that allows different cell components to be combined to create various cell configurations, such as a flow cell with planar electrodes, a flow cell with a GDE, or a full MEA setup, to enable direct comparisons across cell configurations.[133]

Table 2.1: Overview of macroscopic-scale electrochemical CO_2R models and their implementation approaches for reaction mechanism, calculation of electrochemical reaction rates, potential distribution within the electrolyte phase, liquid species transport, and transport in the gas phase. Models developed in this work are marked in bold.

Model domain	Cathode	Reaction mechanism CO_2R	reaction rate	Potential in electrolyte (closing condition)	Liquid transport	Gas transport	Source
Half-cell (dynamic)	planar Cu	one-step reaction	current input and FE from experiments	-	Fick Diffusion	-	[113]
Half-cell (steady-state)	planar Cu	one-step reaction	current input and 100% FE	-	Nernst-Planck	-	[67]
Half-cell (dynamic)	Cu nanowires	one-step reaction	current input and FE from experiments	-	Fick Diffusion	-	[114]
Half-cell (dynamic)	Cu (nanoneedles)	one-step reaction	Butler-Volmer	-	Fick Diffusion with bubble-induced conv. flow	-	[115]
Half-cell (dynamic)	**planar Ag**	**two-steps mechanisms for CO**	**activity dependent Butler-Volmer**	**charge conservation**	**Nernst-Planck**	**-**	**[134]**
Half-cell (steady-state)	planar Ag & Au	two-steps mechanisms for CO	activity dependent Butler-Volmer	electroneutrality	Nernst-Planck	-	[116]
Half-cell (steady-state)	planar Ag	three alternative mechanisms	current input and Transition State Theory	charge conservation	Nernst-Planck	-	[117]
Half-cell (steady-state)	planar Ag	two-steps mechanisms for CO and HCOOH		modified Poisson-Nernst-Planck		-	[37]
Half-cell with EDL	planar Ag	one-step reaction	current input and experimental FE	generalized modified Poisson-Nernst-Planck		-	[120]
Half-cell with EDL	planar Au	three-step reaction	Brønsted-Evans-Polanyi scaling relation and Transition State Theory	generalized modified Poisson-Nernst-Planck		-	[62]
Full-cell with EDL (dynamic)	planar electrodes	none	-	generalized modified Poisson-Nernst-Planck		-	[23]
Half-cell trickle-bed reactor	tinned-copper mesh and tin granule	one-step reaction	CO_2 concentration dependent Tafel kinetics	-	not described	not further described	[122]
Full-cell (steady-state)	Ag-GDE (not resolved locally)	one-step reaction	CO_2 concentration dependent Tafel kinetics	charge conservation	Nernst-Planck with convection	Fick diffusion and convection	[123]
Full-cell (steady-state)	Ag and Au GDE with GDL and CL	two-steps mechanisms for CO	activity dependent Butler-Volmer	electroneutrality	Nernst-Planck	Stefan-Maxwell diffusion	[116]
Half-cell (steady-state)	Ag-GDE with CL,MPL, and GDL	one-step reaction	concentration dependent Tafel kinetics	charge conservation	Nernst-Planck	mixed Stefan-Marxwell, Knudsen-diffusion, and conv. Darcy law	[125]
Half-cell (steady-state)	carbon-free Ag-GDE	one-step reaction with CO desorption	concentration dependent Tafel kinetics	Poisson	modified Nernst-Planck with sterical term	mixed Stefan-Marxwell, Knudsen-diffusion	[127]
Half-cell (dynamic)	carbon-free Ag-GDE	one-step reaction	concentration dependent Tafel kinetics	electroneutrality	Nernst-Planck with convection (Darcy law)	Stefan-Marxwell Diffusion and conv. Darcy law	[129]
Half-cell (dynamic)	**Ag carbon-free GDE**	**two-steps mechanisms for CO**	**activity dependent Butler-Volmer**	**charge conservation**	**Nernst-Planck**	**Fick Diffusion**	**[87]**
Full-cell (steady-state)	planar Ag	one-step reaction for CO	Butler-Volmer	ohmic and diffusion losses	Nernst-Planck	-	[132]
Full-cell	Ag MEA with AEM, CL, and GDL	one-step reaction for CO	concentration dependent Tafel kinetics	charge conservation	Nernst-Planck and electro-osmosis for water	mixed Stefan-Marxwell, Knudsen-diffusion and conv. Darcy-Law	[102]
Full-cell (modular)	Ag and Cu	one-step reaction for CO & C_2H_4	Butler-Volmer	Ohmic law	Fick diffusion, membrane: electro-osmosis for water	neglected	[133]

2.4 Concluding remarks

Electrochemical systems can generally be described by their reaction kinetics, charge and species transport, and interfacial effects. Using stationary and transient analysis methods, these processes can be resolved by analyzing the current-potential behavior under defined reaction conditions. Performance characteristics such as current density, Faradaic efficiency, energy efficiency, and stability further enable the evaluation and comparison of, for example, catalyst materials, operating conditions, and cell configurations.
Electrochemical CO_2 reduction represents a promising yet challenging system in these respects. The choice of catalyst material, electrolyte, electrode structure, and cell configuration strongly affects electrode and cell performance, while identifying the underlying causes is often complicated by the interaction of the individual processes within the system.
This complexity makes the development and application of physical models essential, as they can reproduce and analyze the system and its relevant processes. Depending on the scope of investigation, these models differ in their modeling domain, implemented reaction mechanisms, mass transport descriptions, and calculation of the electrolyte potential. Model-based analysis enables, for example, valuable insights into the reaction mechanism, the influence of local reaction conditions on cell performance, and the limitations of specific cell configurations.

Two dynamic models were developed as part of this thesis to analyze electrochemical CO_2R at a silver catalyst in an aqueous electrolyte. The first model of a planar silver electrode enables investigation of the transient behavior of CO_2R under controlled mass transport conditions and the enhancement by metal-organic framework coating, while the second model examines the impact of operation and electrode parameters on performance-limiting processes in carbon-free gas diffusion electrodes.
The modeling approaches used to describe the relevant processes are summarized in Table 2.1 (bold entries) and include:

- The kinetics of electrochemical CO_2 reduction and the hydrogen evolution reaction were represented by a lumped two-step mechanism for each reaction (for more information, see section 3.2), modeled using the activity-dependent Butler-Volmer equation (Eq. 2.3).
- Ionic and dissolved species transport in the electrolyte was described by the Nernst-Planck equation, incorporating Fickian diffusion and migration, while the electrolyte potential gradient was calculated using charge conservation as a closing condition. For the GDE model, convective Stefan flow in the gas phase was also considered alongside Fickian diffusion and migration.

- CO_2 solubility in both models was calculated based on Henry's law, accounting for salt concentration and partial pressure. Due to the high gas/liquid interface in the GDE, water evaporation and product gas outgassing were also implemented via Raoult's law and ideal gas law.

The fully derived and detailed equations are also presented in the respective chapters of the model description (section 3.2, 4.3, and 5.3).
For validation and analysis, cyclic voltammetry measurements were conducted at a planar rotating disk electrode with low rotation rates to investigate the dynamic versus stationary operation of CO_2R under controlled mass transport conditions. In the GDE study, the differential pressure between the gas and liquid sides of the electrode, electrode thickness, and PTFE content in the electrode were varied. For each variation, galvanostatic steady-state current-potential curves and gas analysis for Faradaic efficiency were measured.

3 CO_2 Reduction at Planar Ag Electrodes[1]

3.1 Introduction

Research on electrochemical CO_2R covers a huge range of development aspects: catalyst development[135–138], electrode structure optimization[139, 140], and cell and process design[97, 141]. Electrochemical analysis methods are widely used for characterization and performance evaluation in all three aspects. Experimental stationary analysis and models are widely used to determine kinetic parameters such as exchange current density and catalytic activity from Tafel plots and polarization curves.[142–144] A prerequisite for comparing catalyst materials is establishing uniform and well-defined mass transport conditions. For example, high rotation rates in rotating disk electrode setups avoid diffusion limitations.[145] However, studies show that the local reaction conditions of CO_2R in aqueous bicarbonate electrolytes are strongly controlled by mass transport. The interplay between the electrochemical reactions, transport processes, and the chemical carbonate equilibrium leads to high complexity. Previous studies on air-operated alkaline membrane fuel cells showed that carbonation in the electrolyte is a slow process in a similar time range as migration or diffusion, leading to complex concentration profiles and pH changes near and at the electrodes.[146] This makes catalyst characterization and performance prediction challenging.[147] Thus, due to the strong influence of mass transport, it is essential to identify the hydrodynamic conditions of the cell setup. For steady-state measurements on silver electrodes, this has already been established.[145]

Steady-state polarization curves lack the ability to separate processes with similar time constants.[148] Additionally, they take a long time and the potential signal is disturbed by gas bubble formation for most gas-evolving reactions, such as oxygen and hydrogen evolution reactions[149], chlorine evolution[150], or CO_2 reduction[151, 152].

Dynamic analysis of the system provides a remedy for all these challenges. Dynamic analysis of mass transport is often carried out by chronoamperometry. Experimental observations of the current change during the applied potential steps can be analyzed, for example, by the simple

[1] Parts of this chapter have been published in Dorner et al., ChemElectroChem, 2023 [134]

Cottrell equation[9, 153] or by a physicochemical model when complex interactions such as phase change and diffusion of multiple species are involved[154, 155]. Gupta et al.[113] reported on a dynamic model including the diffusion of dissolved species for the electrochemical CO_2 reduction on a copper electrode. The transient state analysis via potential step and pulsed potentials showed a strong dependency of the local CO_2 concentration and pH on the diffusion layer thickness and on time.[113] The work emphasizes the importance of considering mass transport but needs to explain the reasons in detail. In-depth investigations of pulsed electrochemical reduction of CO_2 on copper have revealed the strong influence of pulsed potentials and their duration times on Faradaic efficiency for CO_2R and C2+ products. These studies highlight the significant impact on the dynamic behavior of interacting processes within this reaction system, which mainly defines the local state at the electrode.[156, 157]

Dynamic methods such as cyclic voltammetry or electrochemical impedance spectroscopy (EIS) are well-known analysis techniques. But they are rarely used for quantifying mass transport or kinetic parameters in the electrochemical CO_2 reduction.[148] Their transient nature requires calculations and modeling effort when electrochemical reaction, mass transport processes, and electrolyte effects are superimposed and interact. Nevertheless, these techniques, in combination with dynamic modeling, offer the possibility of separating and analyzing reaction kinetics and mass transport phenomena individually.[20] Impedance spectroscopy allows reaction and mass transport to be separated at a defined operating point; the reaction typically yields in a semicircle within a high-frequency range, while at low frequencies, a Warburg-type arc or straight line is observed.[158] Physicochemical models can provide insights into these processes and help to understand reaction and transport phenomena. For instance, they identify and explain inductive behavior at low frequencies caused by complex kinetics with adsorbed intermediates,[159] or heterogeneously flooded electrodes, which lead to a broad distribution of time constants[160]. For CO_2 reduction, Bienen et al. performed a comprehensive EIS analysis of electrochemical carbon dioxide reduction at tin electrodes.[84, 161] Both, CO_2 reduction and competing HER, result in a combined, mixed time constant. A low-frequency process may be attributed to ionic transport but cannot be reliably identified.

Cyclic voltammograms allow better identification of reaction kinetic constants for multi-step reactions, including electrochemically coupled chemical reaction steps on the surface[162], as reactions occur at specific potentials. They have also been used to identify reaction kinetics and parameters for multi-step reactions where homogeneous reactions occur in the electrolyte and where mass transport affects the measurement.[20] In addition, cyclic voltammetry provides rapid system analysis and is less affected by the perturbation of the current-potential-curve caused by gas evolution. Besides the electrochemical reaction and mass transport processes, the pH-dependent carbonate equilibrium in the electrolyte plays an important role (Eqs. 2.49-2.51). It significantly determines the local reaction conditions, such as CO_2 availability and pH value. It

is concluded that knowledge about the kinetics of the buffer reactions is required because equilibrium conditions are not achieved in steady-state operation.[67] Dynamic analysis using differential electrochemical mass spectrometry confirms that the carbonate buffer reaction is an additional pathway of CO_2 consumption. It is observed experimentally only at slow scan rates $<20\,\mathrm{mV\,s^{-1}}$ and is suppressed at high scan rates. It is supposed that the occurrence of CO_2 consumption by carbonation at slow scan rates only results from the slow rate of the carbonate buffer reaction.[163] In addition, time-resolved pH measurements at gold electrodes in acidic 0.1 M Li_2SO_4 observed a slow dynamic adaptation of the local pH value after potential steps.[36, 164] A simulative study that clarifies the detailed interactions between reaction rates of carbonation, transport, and local reaction conditions has been lacking.
This study will show how to adjust conditions for dynamic operation for rapid and almost gas bubble-unaffected characterization of catalysts in electrochemical CO_2 reduction. Mass transport limitations can be easily revealed by varying the scan rate. Furthermore, the reasons for the discrepancy between the steady-state polarization curve and the cyclic voltammogram are explained using a dynamic physicochemical, experimentally validated model for CO_2 reduction on planar silver electrodes. By varying the rotation rates in rotating disk electrode setups, which imitates the effect of diffusion layers of real flow cell setups, it is shown that the hydrodynamic conditions strongly affect dynamic and steady-state performance. Insightful conclusions are derived for the interaction of transport processes, electrochemical reaction, electrolyte reaction, and their influence on current densities and Faradaic efficiency.

3.2 Dynamic macrokinetic modeling approach for planar electrode

In this section, the mathematical model is presented, and a detailed explanation of the individual model equations and underlying assumptions is given. All constant model parameters can be found in Table 3.1.
The model includes the description of a planar silver electrode, as well as the diffusion layer in front of the electrode and the adjacent bulk electrolyte phase (see Figure 3.1). The concentration of the bulk electrolyte is assumed to be constant due to its large electrolyte volume and the low total CO_2 consumption relative to its overall concentration in the bulk solution. The bulk concentrations are used as boundary conditions for the model at the interface between the diffusion layer and the bulk. The electrochemical reaction system is assumed as a two-step mechanism for the CO_2R and the alkaline HER, respectively.[116] The latter is described by the Volmer-Heyrovsky mechanism.

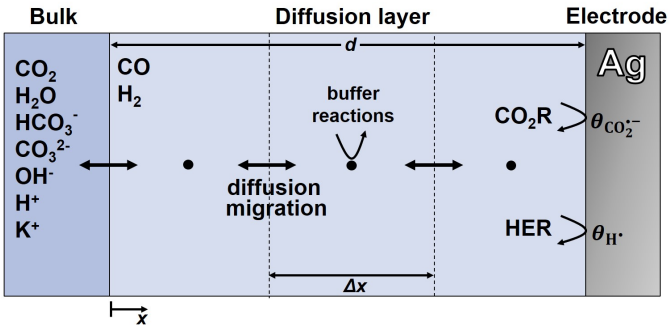

Figure 3.1: Model representation for the CO_2R at planar silver electrode with all involved species, transport mechanisms in the diffusion layer, carbonatization, and competing hydrogen evolution reaction.

This leads to the following reaction equations and allows the description of competitive adsorption and surface blockage (Eq. 3.1-3.4).

$$\mathrm{CO_{2(diss)} + e^- + [\,] \overset{r_{CO2R,1}}{\rightleftharpoons} CO_2^{\bullet -}} \tag{3.1}$$

$$\mathrm{CO_2^{\bullet -} + H_2O + e^- \overset{r_{CO2R,2}}{\rightleftharpoons} CO + 2\,OH^- + [\,]} \tag{3.2}$$

$$\mathrm{H_2O + e^- + [\,] \overset{r_{HER,1}}{\rightleftharpoons} H^{\bullet}_{(ads)} + OH^-} \tag{3.3}$$

$$\mathrm{H^{\bullet}_{(ads)} + H_2O + e^- \overset{r_{HER,2}}{\rightleftharpoons} H_2 + OH^- + [\,]} \tag{3.4}$$

[ ] denotes a free catalyst surface site. The surface specific electrochemical reaction rate r_j of each surface reaction j is calculated by a Butler-Volmer-equation approach following Equations 3.5-3.8:

$$\begin{aligned} r_{\mathrm{CO2R,1}} = {} & k_{0,\mathrm{f},1} \cdot \exp\left(\frac{-(1-\alpha_{\mathrm{CO_2R}})\mathrm{F}}{\mathrm{R}T}\eta_1\right) \cdot a_{\mathrm{surf,CO_2}} \cdot \theta_{[\,]} \\ & - k_{0,\mathrm{b},1} \cdot \exp\left(\frac{\alpha_{\mathrm{CO_2R}}\mathrm{F}}{\mathrm{R}T}\eta_1\right) \cdot \theta_{\mathrm{CO_2^{\bullet -}}} \end{aligned} \tag{3.5}$$

$$\begin{aligned} r_{\mathrm{CO2R,2}} = {} & k_{0,\mathrm{f},2} \cdot \exp\left(\frac{-(1-\alpha_{\mathrm{CO_2R}})\mathrm{F}}{\mathrm{R}T}\eta_2\right) \cdot \theta_{\mathrm{CO_2^{\bullet -}}} \cdot a_{\mathrm{surf,H_2O}} \\ & - k_{0,\mathrm{b},2} \cdot \exp\left(\frac{\alpha_{\mathrm{CO_2R}}\mathrm{F}}{\mathrm{R}T}\eta_2\right) \cdot a_{\mathrm{surf,CO}} \cdot a_{\mathrm{surf,OH^-}} \cdot \theta_{[\,]} \end{aligned} \tag{3.6}$$

$$\begin{aligned} r_{\mathrm{HER,1}} = {} & k_{0,\mathrm{f},3} \cdot \exp(\frac{-(1-\alpha_{\mathrm{HER}})\mathrm{F}}{\mathrm{R}T}\eta_3) \cdot a_{\mathrm{surf,H_2O}} \cdot \theta_{[\,]} \\ & - k_{0,\mathrm{b},3} \cdot \exp\left(\frac{\alpha_{\mathrm{HER}}\mathrm{F}}{\mathrm{R}T}\eta_3\right) \cdot \theta_{\mathrm{H^{\bullet}}} \cdot a_{\mathrm{surf,OH^-}} \end{aligned} \tag{3.7}$$

Table 3.1: Model parameters of planar model

Parameter	Symbol	Value	Unit	Source
Operating conditions				
Concentration of electrolyte	c_{elyt}	0.1	$\mathrm{mol\,L^{-1}}$	
Pressure of gas side for CO_2	$p_{\mathrm{CO_2}}$	1	atm	
Temperature	T	298.15	K	[a]
Geometrical surface area of electrode	A_{geom}	1.9635×10^{-5}	$\mathrm{m^2}$	
Internal ohmic resistance	R_{int}	130	Ω	[b]
Diffusion layer thickness for 50 rpm	$d_{50\mathrm{rpm}}$	103.0×10^{-6}	m	[c]
Diffusion layer thickness for 150 rpm	$d_{150\mathrm{rpm}}$	50.3×10^{-6}	m	[c]
Diffusion layer thickness for 300 rpm	$d_{300\mathrm{rpm}}$	44.7×10^{-6}	m	[c]
Electrochemical surface reaction				
Reaction rate constant for forward reaction of electrochemical CO_2 adsorption	$k_{0,\mathrm{f,CO2R},1}$	8.076×10^{-6}	$\mathrm{mol\,m^{-2}\,s^{-1}}$	[d]
Reaction rate constant for forward reaction of electrochemical CO desorption	$k_{0,\mathrm{f,CO2R},2}$	7.708×10^{-4}	$\mathrm{mol\,m^{-2}\,s^{-1}}$	[d]
Reaction rate constant for forward reaction of electrochemical H_2O adsorption (Volmer step)	$k_{0,\mathrm{f,HER},1}$	7.550×10^{-10}	$\mathrm{mol\,m^{-2}\,s^{-1}}$	[d]
Reaction rate constant for forward reaction of electrochemical H_2 desorption (Heyrovsky step)	$k_{0,\mathrm{f,HER},2}$	8.532×10^{-8}	$\mathrm{mol\,m^{-2}\,s^{-1}}$	[d]
Charge transfer coefficient for CO_2 reduction	$\alpha_{\mathrm{CO_2R}}$	0.661	-	[d]
Charge transfer coefficient for hydrogen evolution reaction	α_{HER}	0.687	-	[d]
Standard redox potential of CO_2R	$E^{00}_{\mathrm{CO_2R}}$	-0.11	V	[117]
Standard redox potential of HER	E^{00}_{HER}	0	V	[117]
Specific capacitance of electrical double layer	C_{DL}	100	$\mathrm{\mu F\,cm^{-2}}$	[b]
Concentration of surface adsorption sites	Γ	7.04×10^{-6}	$\mathrm{mol\,m^{-2}}$	[117]
Electrolyte conditions				
Activity coefficient of dissolved species i	γ_i	1	-	[a]
Standard concentration of dissolved species i	$c_i^{\ominus}$	1	$\mathrm{kmol\,m^{-3}}$	[a]
Diffusion coefficient of dissolved CO_2	$D_{\mathrm{CO_2}}$	1.91×10^{-9}	$\mathrm{m^2\,s^{-1}}$	[165]
Diffusion coefficient of H_2O	$D_{\mathrm{H_2O}}$	2.57×10^{-9}	$\mathrm{m^2\,s^{-1}}$	[166]
Diffusion coefficient of OH^-	$D_{\mathrm{OH^-}}$	5.273×10^{-9}	$\mathrm{m^2\,s^{-1}}$	[167]
Diffusion coefficient of H^+	$D_{\mathrm{H^+}}$	9.311×10^{-9}	$\mathrm{m^2\,s^{-1}}$	[167]
Diffusion coefficient of HCO_3^-	$D_{\mathrm{HCO_3^-}}$	1.185×10^{-9}	$\mathrm{m^2\,s^{-1}}$	[167]
Diffusion coefficient of CO_3^{2-}	$D_{\mathrm{CO_3^{2-}}}$	0.923×10^{-9}	$\mathrm{m^2\,s^{-1}}$	[167]
Diffusion coefficient of K^+	$D_{\mathrm{K^+}}$	1.957×10^{-9}	$\mathrm{m^2\,s^{-1}}$	[167]

[a] assumption, [b] measured, [c] estimated close to the Levich equation (see Supporting Information),
[d] model parametrization to experiments.

$$
\begin{aligned}
r_{\mathrm{HER},2} = k_{0,\mathrm{f},4} \cdot \exp\left(\frac{-(1-\alpha_{\mathrm{HER}})\mathrm{F}}{\mathrm{R}T}\eta_4\right) \cdot a_{\mathrm{surf,H_2O}} \cdot \theta_{\mathrm{H^\bullet}} \\
- k_{0,\mathrm{b},4} \cdot \exp\left(\frac{\alpha_{\mathrm{HER}}\mathrm{F}}{\mathrm{R}T}\eta_4\right) \cdot a_{\mathrm{surf,H_2}} \cdot a_{\mathrm{surf,OH^-}} \cdot \theta_{[\,]}
\end{aligned}
\tag{3.8}
$$

with $k_{0,j}$ being the reaction rate constants of forward (f) and backward (b) reaction j, the overpotential η_j, α the anodic charge transfer coefficient of CO_2R or HER, the activity of dissolved species $a_{\mathrm{surf},i}$ with $i \in \Omega = \{\mathrm{CO_2; CO; OH^-; H_2; H_2O; HCO_3^-; CO_3^{2-}; H^+; K^+}\}$ at the catalyst surface and coverage of adsorbed species and free adsorption sites θ_k with $k \in \Omega =$

$\{CO^{\bullet-}_{2(ads)}; H^{\bullet}_{(ads)}; [\,]\}$. The backward reaction rate constants turned out to be insensitive in the simulated potential range because the investigated potential range is far away from the open circuit potential and the anodic potential range. Hence, the values of backward reaction rate constants $k_{0,\mathrm{b},j}$ were set to a value of $1 \times 10^{-25}\,\mathrm{mol\,m^{-2}\,s^{-1}}$.
The activities of dissolved species were calculated assuming ideal behavior of a diluted solution. Thus, I set activity coefficient γ_i to 1 and standard concentration to $c_i^{\ominus} = 1\mathrm{kmol\,m^{-3}}$ (Eq. 3.9).

$$a_i = \gamma_i \frac{c_i}{c_i^{\ominus}} \tag{3.9}$$

The activity of water as a solvent is set to $a_{\mathrm{H_2O}} = 1$ and the concentrations of dissolved product gases CO and H_2 were neglected due to their low solubility in water.
The shift of the overpotential η due to pH using RHE reference electrode is calculated via the Nernst equation:

$$\eta_{\mathrm{j}} = E - \left(E^{00}_{\mathrm{j}} - 2.303 \frac{\mathrm{R}T}{\mathrm{F}} \mathrm{pH_{bulk}} \right) \tag{3.10}$$

with E^{00}_{j} as the standard potential of reaction j. E^{00}_{j} are set equal for single steps of CO_2 reduction with $E^{00}_{\mathrm{CO_2R}}$ and for HER to E^{00}_{HER} as it is done for lumped reaction kinetics.[117] Differences in E^{00}_{j} or free energies of reaction ΔG_j are included in the reaction rate constants.
The electrical double layer is related to a potential drop at the electrode to electrolyte boundary. It is not locally resolved. Thus, the charge balance results in

$$\frac{\mathrm{d}E}{\mathrm{d}t} = \frac{1}{C_{\mathrm{DL}}} \left(j - \mathrm{F} \sum_j r_j \right) \tag{3.11}$$

where C_{DL} is the specific electrical double layer capacitance of the electrode and j the total current. The electrode potential is calculated by correcting the external potential E_{ext}, which is the measured potential vs. RHE, with the potential drop due to uncompensated resistance with the current density j, the geometrical surface of the electrode A_{geom}, and the internal resistance R_{int}:

$$E = E_{\mathrm{ext}} - j A_{\mathrm{geom}} R_{\mathrm{int}} \tag{3.12}$$

Molar transport fluxes N of all dissolved species i are described by the Nernst-Planck equation with Fickian diffusion and migration (Eq. 2.9) and the mobility of the species is approximated with the Nernst-Einstein equation for diluted systems (Eq. 2.10).
To establish electroneutrality and to calculate the potential gradient in the electrolyte, conservation

of charge as a closing condition is applied as it is described in section 2.1.2.2.
Applying conservation of mass, the adsorbed species at the surface can be balanced as

$$\frac{\partial \Theta_k}{\partial t} = \frac{1}{\Gamma} \sum_k \nu_{k,j} r_j, \tag{3.13}$$

where Θ_k is the surface coverage of the adsorbed species k and Γ is the concentration of surface adsorption sites at the catalyst surface.
For the species in the electrolyte, the respective species balance is:

$$\frac{\partial c_i}{\partial t} = -\nabla N_i + \dot{S}_i \tag{3.14}$$

$\dot{S}_i$ is the source term of species i in the electrolyte due to consumption or production in reactions at the electrode surface K and homogeneous chemical reactions in the electrolyte L, where species i is consumed or produced (Eq. 3.15).

$$\dot{S}_i = \sum_{j=1}^{K} \frac{\nu_{i,j} r_j}{\Delta x} + \sum_{j=1}^{L} \nu_{i,j} r_j \tag{3.15}$$

with Δx as the width of the volume element next to the electrode. To account for carbonation or decarbonation reactions occurring in the electrolyte, the homogeneous chemical reactions in the electrolyte phase under alkaline and neutral conditions are considered (Eq. 2.49 - 2.51).[65, 66]
The values of the forward reaction rate constants $k_{\mathrm{f,i}}$ and equilibrium constants K_i are shown in Table 3.2 for electrolyte concentration of 0.1 M $KHCO_3$. The backward reaction rate constants $k_{\mathrm{b},i}$ are calculated by

$$K_i = k_{\mathrm{f},i} / k_{\mathrm{b},i}. \tag{3.16}$$

Table 3.2: Values of reaction rate constants and equilibrium constants for the carbonate reaction system for a concentration of 0.1 M $KHCO_3$ and $T = 298.15$ K.

Parameter	Value	Unit	Source
$k_{\mathrm{f,w}}$	2.4×10^{-2}	$\mathrm{mol\,m^{-3}\,s^{-1}}$	[66]
K_{w}	1×10^{-8}	$\mathrm{mol^2\,m^{-6}}$	[65]
$k_{\mathrm{f,c1}}$	5.93	$\mathrm{m^3\,mol^{-1}\,s^{-1}}$	[66]
K_{c1}	4.44×10^4	$\mathrm{m^3\,mol^{-1}}$	[65]
$k_{\mathrm{f,c2}}$	1×10^5	$\mathrm{m^3\,mol^{-1}\,s^{-1}}$	[66]
K_{c2}	4.66	$\mathrm{m^3\,mol^{-1}}$	[65]

The volumetric chemical reaction rates for water dissociation (w), CO_2 carbonation (c1), and HCO_3^- carbonation (c2) are thus given by

$$r_{\mathrm{w}} = k_{\mathrm{f,w}} - k_{\mathrm{b,w}} \cdot c_{\mathrm{H^+}} \cdot c_{\mathrm{OH^-}} \tag{3.17}$$

$$r_{\mathrm{c1}} = k_{\mathrm{f,c1}} \cdot c_{\mathrm{CO_2}} \cdot c_{\mathrm{OH^-}} - k_{\mathrm{b,c1}} \cdot c_{\mathrm{HCO_3^-}} \tag{3.18}$$

$$r_{\mathrm{c2}} = k_{\mathrm{f,c2}} \cdot c_{\mathrm{HCO_3^-}} \cdot c_{\mathrm{OH^-}} - k_{\mathrm{b,c2}} \cdot c_{\mathrm{CO_3^{2-}}} \tag{3.19}$$

This takes into account that the ionic species of the carbonate reaction system are not necessarily in equilibrium.
The concentration of dissolved CO_2 $c_{\mathrm{CO_2(diss)}}$ is calculated by Henry's law

$$c^0_{\mathrm{CO_2(diss)}} = H^{\mathrm{cp}}_{\mathrm{CO_2}} \cdot p_{\mathrm{CO_2}} \tag{3.20}$$

with the Henry coefficient $H^{cp}_{\mathrm{CO_2}}$ and partial pressure of CO_2 $p_{\mathrm{CO_2}}$. The partial pressure is assumed to be 1 atm. The Henry coefficient $H^{cp}_{\mathrm{CO_2}}$ for pure water, depending on temperature, is calculated by Equation 3.21 assuming isothermal conditions with a temperature of $298.15\,\mathrm{K}$ (Eq. 3.21).

$$\ln H^{\mathrm{cp}}_{\mathrm{CO_2}} = 93.4517\frac{100}{T} - 60.2409 + 23.3585\ln\frac{T}{100} \tag{3.21}$$

The decrease of solubility with increasing salt concentration in the electrolyte by the "salting-out" effect is considered by Sechenov equation (Eq. 3.22 and Table 3.3).[168]

$$\log\frac{c^0_{\mathrm{CO_{2(diss)}}}}{c_{\mathrm{CO_{2(diss)}}}} = \sum_m (h_{\mathrm{CO_2}} + h_m)c_m \tag{3.22}$$

It requires the consideration of all dissolved ionic species $m \in \Omega = \{\mathrm{OH^-}; \mathrm{HCO_3^-}; \mathrm{CO_3^{2-}}; \mathrm{H^+}; \mathrm{K^+}\}$ by their substance specific parameter h_{m} and their concentrations c_{m}. The values of parameters can be found in Table 3. Thus, the concentration of dissolved CO_2 in pure water $c^0_{\mathrm{CO_2(diss)}}$ is corrected to yield the concentration of dissolved CO_2 in electrolyte solution $c_{\mathrm{CO_2(diss)}}$ which is used in the model.

The model was implemented in MATLAB R2020b, and differential equations were solved with the ode15s solver. Spatial discretization was done with an equidistant grid and by applying the finite volume method and central differential quotients. Grid size was set to a value of $\Delta x = 1\,\mu\mathrm{m}$ and convergence of the solution regarding grid parameters was confirmed as refining the parameters led to no visual changes of the CVs and concentration profiles. The system was initialized by holding the starting potential of $-0.5\,\mathrm{V}$, where no significant electrochemical reactions take place, until a stationary state was reached. Initial surface coverages $\theta_{\mathrm{k,t=0}}$ and $E_{\mathrm{t=0}}$ were adapted

Table 3.3: Model parameters for the consideration of "salting-out" effect for the solubility of CO_2 in ionic solutions.

Constant	Value	Unit	Source
$h_{\mathrm{CO_2},0}$	-0.0172	$\mathrm{m^3\,kmol^{-1}}$	[168]
$h_{\mathrm{T,CO_2}}$	-0.000338	$\mathrm{m^3\,kmol^{-1}\,K^{-1}}$	[168]
$h_{\mathrm{H^+}}$	0	$\mathrm{m^3\,kmol^{-1}}$	[168]
$h_{\mathrm{K^+}}$	0.0922	$\mathrm{m^3\,kmol^{-1}}$	[168]
$h_{\mathrm{OH^-}}$	0.0839	$\mathrm{m^3\,kmol^{-1}}$	[168]
$h_{\mathrm{HCO_3^-}}$	0.0967	$\mathrm{m^3\,kmol^{-1}}$	[168]
$h_{\mathrm{CO_3^{2-}}}$	0.1423	$\mathrm{m^3\,kmol^{-1}}$	[168]

from the stationary state. Initial concentrations were set to electrolyte bulk concentrations, where the equilibrium of carbonate species and dissolved CO_2 is adjusted.
The reaction rate constants for the forward reaction of the electrochemical reactions $k_{0,\mathrm{f},1}$, $k_{0,\mathrm{f},2}$, $k_{0,\mathrm{f},3}$, $k_{0,\mathrm{f},4}$ and the charge transfer coefficient of CO_2R $\alpha_{\mathrm{CO_2R}}$ and HER α_{HER} were identified by optimizing the model output on experimental CV curves for the scan rates of 50 and $200\,\mathrm{mV\,s^{-1}}$ at a rotation rate of 50 rpm. For higher rotation rates of 150 and 300 rpm, only the diffusion layer thickness was adapted. The kinetic parameters were retained from the parameter identification at 50 rpm.

3.3 Experimental characterization

All electrochemical measurements were conducted in a three-electrode setup using a PTFE cell with an electrolyte volume of $250\,\mathrm{mL}$. As a working electrode, a planar silver rotating disk electrode (surface area $A_{\mathrm{geom}} = 0.1963\ \mathrm{cm^2}$) with PEEK shroud from PINE Research Instrumentation Inc., and as counter electrode, a spiral platinum wire was used. All potentials were measured and plotted against a reference electrode, the HydroFlex reversible hydrogen electrode from Gaskatel mbH. The potentials were corrected for uncompensated resistance afterward. For variation of rotation rates, a rotating disk electrode setup from PINE Research Instrumentation Inc. was connected with a Gamry Interface 1010E potentiostat. Before each measurement, the silver electrode was polished with diamond compound with a particle size of $0.25\,\mathrm{\mu m}$ from Kemet. As a solvent and for rinsing, deionized water (16 MΩcm) was used. Aqueous potassium bicarbonate solution ($0.1\,\mathrm{M}$, BioUltra ≥99.5%, Sigma Aldrich) was used as electrolyte. The electrolyte was purged with CO_2 for 15 min before starting the experiment to ensure saturation with CO_2. During the experiment, a CO_2 atmosphere was realized in the gas volume above the solution.

Cyclic voltammetry was performed in a potential window of $-0.5\,\mathrm{V}$ to $-2.0\,\mathrm{V}$ vs. RHE with rotation speeds between 50 and 150 rpm and between $-0.5\,\mathrm{V}$ to $-2.5\,\mathrm{V}$ vs. RHE for 300 rpm. The scan rate of the potential sweep was set to values of $\nu = \{50; 100; 200; 300\ \mathrm{mV\ s^{-1}}\}$. The number of cycles was eight for each scan rate to guarantee a quasi-steady state. In the figures, only the last cycle is displayed.
Electrochemical impedance spectra were recorded for each scan rate after a CV measurement. It was used to determine the uncompensated resistance for iR-drop correction of the reference electrode potential. Therefore, an AC voltage amplitude of $10\,\mathrm{mV_{rms}}$ was applied at an underlying DC voltage of -0.5 V vs. RHE in a frequency range between 1 MHz and 1 Hz.
The stationary polarisation curve was measured by holding a constant potential for 200 s. The step size of the applied potential was 0.1 V. It was observed that the current density was decreasing with time for measured current densities above $10\,\mathrm{mA\,cm^{-2}}$. This was induced by the bubble accumulation at the electrode and resulted in an increase in the uncompensated resistance with time. The uncompensated resistance was measured after each holding time. Figures show the corrected mean potential and mean error, determined from the last 20 s of each measured potential. Due to the bubble formation, the minimal applied potential of the polarization curve was limited to values around -1.3 V vs. RHE at rotation rates of 150 and 300 rpm.

3.4 Results and discussion

3.4.1 Dynamic vs. steady-state behavior

In the following, differences between the dynamic and steady-state performance will be revealed, quantified, and analyzed. The underlying differences in concentrations at the electrode that cause the performance differences will be explained. The current evolution vs. potential during steady-state and cyclic voltammetry for different scan rates is given in Figure 3.2a for the experiments and in Figure 3.2b for the simulation. Progression of the steady-state and dynamic current curves is similar for experiment and simulation, whereas some quantitative trends between experiment and simulation are slightly different, in particular for the polarisation curve. Lower current densities for this curve compared to dynamic measurement in the intermediate potential range can be caused by stronger limitation than expected in simulations or slightly overcorrected CV curves by iR-correction for experimental results.
The total current density for the forward sweep of the CV and the polarization curve shows a similar behavior, namely an exponential decrease between $-0.8\,\mathrm{V}$ to $-1.2\,\mathrm{V}$, with a plateau in the potential range of $-1.2\,\mathrm{V}$ to $-1.4\,\mathrm{V}$, followed by a consecutive exponential decrease in current. No limiting current is observed in the potential window. The simulations in Figure 3.2c

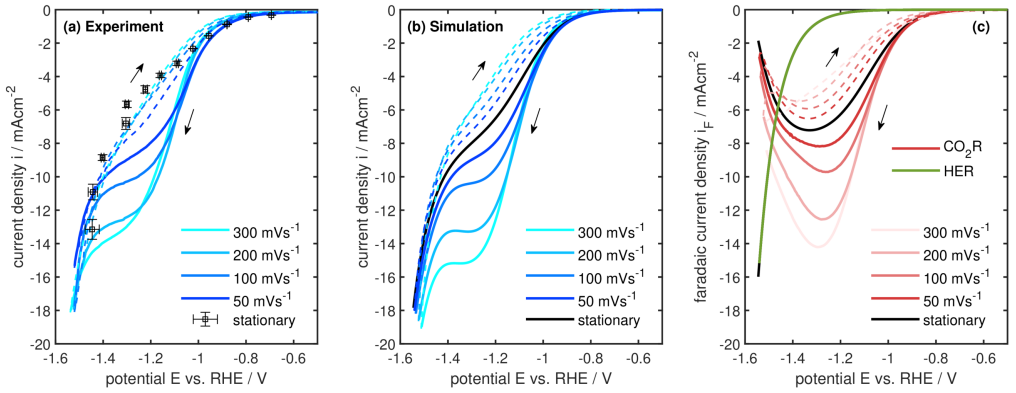

Figure 3.2: (a) Experimental and (b) simulated cyclic voltammograms for different scan rates and steady-state polarization curve for a rotation rate of 50 rpm. (c) Corresponding simulated Faradaic current densities for CO_2R and HER as a function of potential. Forward sweeps are shown in solid lines and backward sweep in dashed lines. Conditions: CO_2 saturated $0.1\,\mathrm{M}$ $KHCO_3$ solution, room temperature, rotation rate of 50 rpm (corresponding to a diffusion layer thickness of $103\,\mu\mathrm{m}$). Potentials are corrected for iR-drop.

show that the potential at which the plateau occurs coincides with a maximum in the Faradaic current for the CO_2R. A similar observation was made experimentally by Hatsukade et al.[43] in a flow cell setup and confirmed by product analysis.[43] Furthermore, my results show that, as the peak in Faradaic current density of CO_2 shifts to higher potentials for faster scan rates, the plateau in current density also shifts in the same direction. The CO_2 reduction is the prevalent electrochemical reaction at potentials between $-0.8\,\mathrm{V}$ to $-1.2\,\mathrm{V}$. At more negative potentials, the CO_2R is suppressed mainly due to the depletion of CO_2 at the electrode surface, as shown in the simulation results, Figure 3.3a. The HER thus becomes the dominant reaction in the potential range below $-1.4\,\mathrm{V}$. A large amount of electrolyte available for the HER reaction explains the absence of a limiting current. While the trend of exponential behavior with an intermediate plateau is identical for all scan rates, a strong dependency of current density on the scan rate is observable in the experiments. The higher the scan rate, the higher the current density is measured at the same potential. This trend is well reproduced by the simulation. Further, experiment and simulation show similar trends in the backward sweep: In contrast to the clear plateau while decreasing potential, there is only a very weak plateau, which is rather a slight decrease in current slope. This correlates well with the lower CO_2 reduction rate and maximum in this region.
There is also a hysteresis between forward and backward sweep, which becomes more significant at higher scan rates. All these observations result in a discrepancy between stationary and dynamic current-potential curves. Simulation in Figure 3.2c shows that the scan rate dependence is very strong for CO_2R, whereas HER is not affected. The strong influence of the scan rate can be partly explained by the difference in the CO_2 concentration at the electrode (see Figure 3.3a): (1) At the upper potential of $-0.5\,\mathrm{V}$, the CO_2 concentration decreases with increasing scan rate. (2) In the

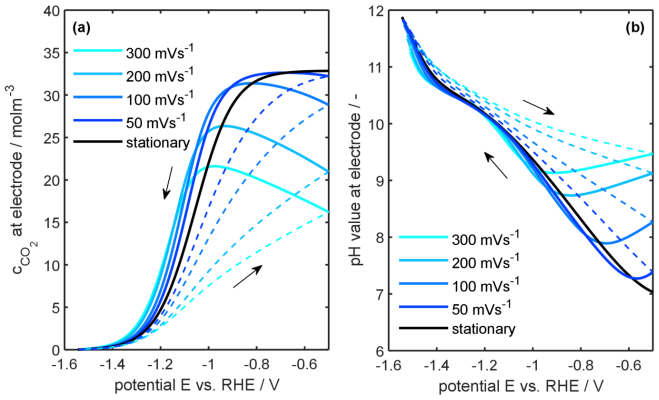

Figure 3.3: (a) Predicted CO_2 concentration at the electrode during the potential sweep for dynamic and steady-state simulation in dependency of the scan rate and (b) corresponding pH value at the electrode. Forward sweeps are shown in solid lines and backward sweeps in dashed lines. Conditions: CO_2 saturated 0.1 M $KHCO_3$ solution, room temperature, rotation rate of 50 rpm.

intermediate potential range of $-0.5\,\mathrm{V}$ to $-1.0\,\mathrm{V}$, the CO_2 concentrations during the potential sweep are significantly lower than for steady state and increase with decreasing potential for higher scan rates. (3) In all cases, CO_2 concentration drops to 0 in the low potential range of $-1.0\,\mathrm{V}$ to $-1.6\,\mathrm{V}$. This decline occurs earlier at slower scan rates. Additionally, the CO_2 concentration is much lower for the backward sweep than for the forward sweep at the same potential. The difference increases with scan rates, which explains the observed increasing current hysteresis with scan rate in Figure 3.2.

The curves for pH value at the electrode surface in Figure 3.3b show similar, but opposite trends compared to the CO_2 concentration as the scan rate changes. In the high potential region, pH values increase with increasing scan rate. In the intermediate range, pH is reaching a plateau value, which is the highest for the stationary case. With further decreasing potentials, pH increases nearly linearly again with the highest values for stationary operation compared to dynamic operation. The pH value is a measure of hydrogen and CO_2 production, as OH^- is produced in both reactions. In addition, OH^- is consumed by carbonation in the electrolyte according to Equation 2.50 and 2.51. Therefore, most processes strongly change the pH near and at the electrode. The observed trend in the pH and CO_2 surface concentrations can be explained as follows:

(1) The concentration differences in the upper potential region originate from the reaction history. For analysis of cyclic voltammograms, the 8^{th} cycle is selected for accurate process analysis. It ensures that experimental and simulative current-potential curves are stable and reproducible regardless of the cycle number. However, this also means that the processes

and state during the previous cycle influence the concentrations at the beginning of the next cycle. From about $-0.8\,\mathrm{V}$, the current of the backward sweep drops to almost zero, allowing more CO_2 to diffuse to the surface than is consumed. As a result, the CO_2 concentration at the electrode has time to recover during the backward sweep. This recovery time is longer for lower scan rates. For example, at $-0.5\,\mathrm{V}$, the CO_2 concentration for the sweep of $50\,\mathrm{mV\,s^{-1}}$ is almost fully recovered and similar to that of the steady-state curve. In contrast, recovery time and thus CO_2 concentration decreases with increasing scan rate. Analogous to the CO_2 concentration, the pH is the highest for high scan rates, as OH^- has not yet been transported away or reacted further to form carbonates. This effect also causes the hysteresis in current density, CO_2 reduction, and the concentrations of CO_2 and hydroxide ions (pH) for the forward and backward sweep. Higher pH values and lower CO_2 concentrations during the backward sweep for higher scan rates reduce the current density.

(2) The increase in CO_2 concentration with decreasing potential up to approx. $-1\,\mathrm{V}$ for fast sweep rates is directly related to the recovery process. The diffusive transport of CO_2 from the bulk to the electrode and only small consumption rates of CO_2 cause the concentration to increase with time. Similarly, pH decreases due to the transport of OH^- to the bulk and carbonation.

(3) The smaller decline in CO_2 concentration in the low potential range with increasing scan rate is caused by the fact that the CO_2 consumption time in this potential range is much lower for higher scan rates. This results in higher CO_2 concentrations and a later depletion of CO_2 at the electrode during the sweep. It leads to a shift of the plateau value to higher absolute total current and higher absolute Faradaic current densities of CO_2R. The pH increases earlier due to longer reaction time for lower scan rates. The stationary curve shows the highest pH value in this potential region. At a potential of around $-1.3\,\mathrm{V}$, a slight stagnation of the increase can be seen for all curves. This is due to the limitation of CO_2 reduction and the HER becoming the dominant reaction, and corresponds to the plateau in current.

After the reversal point from forward to backward sweep, an increase in pH is observed, especially for high scan rates, although the current density decreases. This phenomenon will be discussed later in the section “Impact of carbonation reactions”. The observed behavior is not changed qualitatively with increasing electrolyte concentration of 0.5 or 1.0 M $KHCO_3$, which is shown in Figure A.5 of the Supporting Information.

Concluding, I have shown that the conditions at the electrode differ significantly between steady-state and dynamic operation. One reason for this is that the transport of CO_2 and OH^- is slower than the potential change during the sweep for high scan rates. In addition, the reaction time, , the time over which a potential is held, determines the extent of consumption and thus concentration change. This means that in cyclic voltammetry, species transport and carbonation impact on the measurements can be easily detected by varying the scan rate. A fast CV scan can only replace a steady state if there is no transport effect and no change in local conditions at the electrode. This is not possible for electrochemical CO_2 reduction under the investigated conditions. It has been shown that fast species transport has an essential impact under given conditions, so the influence of changing the hydrodynamic conditions will be investigated in the following.

3.4.2 Impact of species transport

Adjusting a suitable diffusion layer thickness is essential for preventing transport limitations at planar electrodes in batch and flow cells. A thick layer will cause transport limitations, leading to reduced reactant transport and thus reduced performance during stationary or dynamic operation. Consequently, the diffusion layer thickness strongly impacts the steady-state behavior and the dynamic response of the system to a change in current or – as here – in potential.
As shown in the previous section, variation in scan rate changes the impact that species transport through the diffusion layer has on performance and local concentrations at the electrode. This, in turn, means that changing the diffusion layer thickness should also lead to significant qualitative and quantitative changes in species transport and hence in performance. This finding will have practical implications for designing and adjusting cell configurations for CO_2R.
For the investigation of transport effects, the impact of diffusion layer thicknesses was studied through variation of the rotation rate of the electrode between 50 and $300\,\mathrm{rpm}$. Figure 3.4 shows the current densities during dynamic and stationary operation for $300\,\mathrm{rpm}$. Current densities at a medium speed of $150\,\mathrm{rpm}$ are shown in Figure A.1 in the Supporting Information. The current densities increase significantly with rotation rate from a maximum of $-16\,\mathrm{mA\,cm^{-2}}$ at $50\,\mathrm{rpm}$ to $-27\,\mathrm{mA\,cm^{-2}}$ at $300\,\mathrm{rpm}$, when operating at $-1.4\,\mathrm{V}$. As expected, smaller diffusion layer thicknesses and faster species transport lead to significantly higher absolute current densities at intermediate and low potentials. With more CO_2 being available over a wide potential range, the limitation of CO_2R due to low CO_2 concentrations at the electrode (see Figure 3.4c) is shifted to lower potentials, apparent in the shift of the current plateau in Figure 3.4b to more negative potentials and current densities.
The experimental and simulative results agree well; both show that the dependency of current on the scan rate and the difference between steady-state and dynamic currents, as well as the

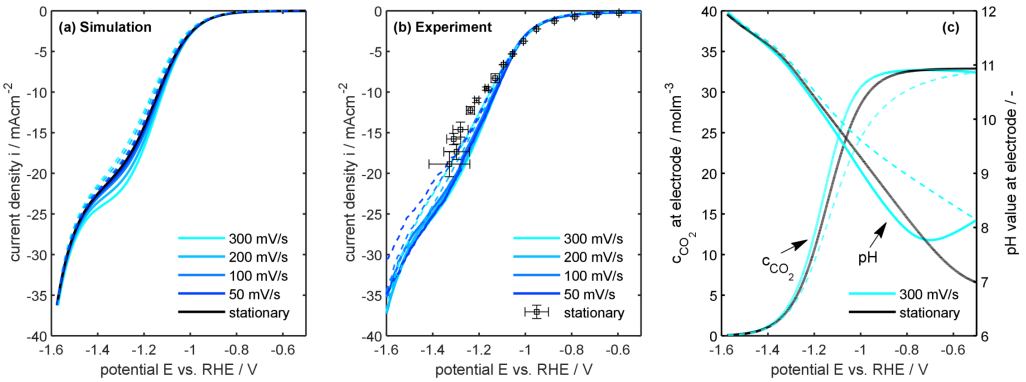

Figure 3.4: (a) Experimental and (b) simulated cyclic voltammograms for different scan rates and steady-state polarization curve for a rotation rate of 300 rpm (d = 45 µm). (c) Predicted CO_2 concentration at the electrode during the potential sweep for dynamic (scan rate of 300 $\mathrm{mV\,s^{-1}}$) and steady state simulation and corresponding pH value at the electrode. Forward sweeps are shown in solid lines and backward sweeps in dashed lines. Conditions: CO2 saturated 0.1 M $KHCO_3$ solution, room temperature. Potentials are corrected for iR-drop.

hysteresis during CV becomes smaller for higher rotation rates. At 300 rpm, there is almost no dependence on the scan rate. Thus, a small diffusion layer thickness allows to get similar results for steady-state and dynamic operation. Comparing the time constants of the diffusive transport τ_{diff} with the time it takes for a potential sweep from $-0.5\,\mathrm{V}$ to $-2.0\,\mathrm{V}$ makes this dependence clear. The time constant can be calculated from

$$\tau_{\mathrm{diff}} \approx \frac{d^2}{D_{\mathrm{CO_2}}} \tag{3.23}$$

with the diffusion layer thickness d and the diffusion coefficient of CO_2 $D_{\mathrm{CO_2}}$. Increasing the rotation rate from 50 rpm to 300 rpm decreases τ_{diff} from 5.6 s to 1.0 s. The time constant is now 5 times smaller than the time it takes for an unidirectional potential sweep of 5 s for a scan rate of $300\,\mathrm{mV\,s^{-1}}$, whereas for 50 rpm, the times are similar. This means that at 300 rpm, sufficient CO_2 can diffuse to the electrode and can partly be replenished during the sweeps. The CO_2 concentration at the electrode is very similar for stationary and $300\,\mathrm{mV\,s^{-1}}$ operation, and there is no maximum anymore for 300 rpm. Also, the differences between steady-state and dynamic pH for a higher rotation have significantly decreased, resulting in a pH difference at $-0.5\,\mathrm{V}$ of 1 for 300 rpm compared to a pH difference of 2.5 for 50 rpm.

Still, the pH recovery takes much longer and is not fully completed under the conditions shown here, as can be seen in the still visible pH minimum for dynamic operation. The readers should notice the logarithmic scale of pH, which emphasizes differences in low absolute concentrations of hydroxide ions much more.

In comparison to 300 rpm, the results at 150 rpm, which corresponds to a diffusion layer thickness

of $50\,\mu m$, still has visible, although small hysteresis for the here investigated conditions of room temperature and 0.1 M $KHCO_3$, shown in FigureA.1. Thus, diffusion layer thicknesses $\geq 45\,\mu m$ lead to non-negligible differences in the dynamic and steady-state current response.
It is known from other simulative studies that the diffusion layer thickness in cell setups can vary in a wide range of 40 and $200\,\mu m$.[113, 125, 155, 169] Therefore, to see if the cell suffers from thick diffusion layers and thus transport losses, CVs can be used in the investigated cell setup at different scan rates. If they are equal, then there is no significant transport limitation. Besides increasing the electrolyte flow rate, the integration of turbulence promoters is possible to decrease the diffusion layer thickness in cells.
For the dynamic operation, the situation changes. For the strongly negative potential region, OH^- consumption by c2 is much higher than for the c1 reaction. This is caused by the different time constants of these reactions. The c2 reaction is much faster due to a higher reaction rate constant and good availability of bicarbonate ions. This results in a domination of the c2 reaction in dynamic operation and a large deviation from equilibrium concentrations of carbonate species. In the backward sweep after the reversal point, the consumption of hydroxide ions by c2 is decreasing strongly in the diffusion layer and becomes positive at a potential of $-1.2\,V$, so hydroxide ions are produced by c2. This effect is created by equilibration, i.e., the thrive to restore equilibrium concentrations of the carbonate system. At these conditions (referring to the local pH and CO_2 concentration), the equilibrium predominantly favors the formation of bicarbonate ions, so carbonate ions react to bicarbonate, and CO_2 reacts with released OH^- to bicarbonate.

3.4.3 Impact of carbonation reaction

The local pH is known to strongly influence the reaction conditions for CO_2 reduction at the electrode.[169–171] Due to the production of OH^- during CO_2R and HER (Eq. 3.1 – 3.4), the pH at the electrode increases, especially when high current densities are reached. The change in pH can be mitigated by the consumption of OH^- via the carbonation reaction with CO_2 to form CO_3^{2-}, as given in Equation 2.50 and 2.51. Furthermore, molar transport of OH^- into the bulk may reduce the accumulation of OH^- at the surface, and thus a fast pH increase. It is still unclear how strong the interaction of carbonation reactions and species transport is, resulting in a local pH change, and how it influences the stationary and dynamic behavior of the reaction system. In the following, I analyze this interplay and its effect on cell performance.
The changes in hydroxide ion concentration within the diffusion layer due to electrochemical and chemical reactions and due to transport from the bulk are shown for stationary operation in Figure 3.5a and for dynamic operation in Figure 3.5b. The main production of OH^- for both, stationary and dynamic operation, is due to the electrochemical reactions. It is equal to the

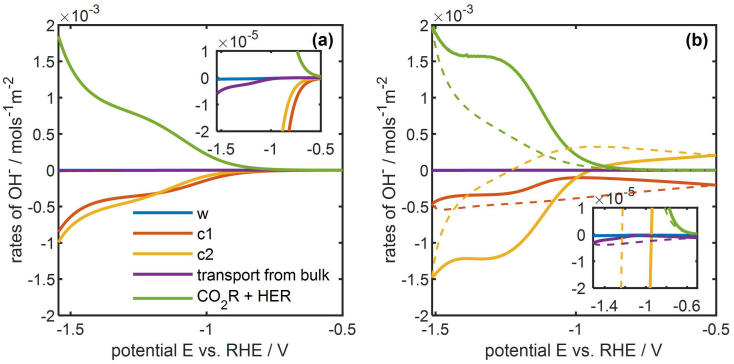

Figure 3.5: Molar transport or reaction rates of hydroxide ions in the diffusion layer caused by water dissociation (w), by CO_2-to-bicarbonate reaction (c1) and by bicarbonate-to-carbonate reaction (c2), by transport of hydroxide ions from the bulk and by the electrochemical reactions HER and CO_2R for a rotation rate of 50 rpm for (a) stationary and (b) dynamic operation. Forward sweeps at $300\,\mathrm{mV\,s^{-1}}$ are shown in solid lines and backward sweeps in dashed lines. Conditions: CO_2 saturated 0.1 M $KHCO_3$ solution, rotation rate of 50 rpm, room temperature. Potentials are corrected for iR-drop.

current response, as both HER and CO_2R produce one OH^- per e^-. It thus also increases with more negative potential. Most of these hydroxide ions are consumed by the chemical carbonation reactions (c1 and c2 in Figure 3.5). Their combined consumption curves resemble a mirror image of the electrochemical production rate. In contrast, the rates of hydroxide ions leaving the diffusion layer to the bulk or being produced or consumed by water dissociation are much lower; these OH^- sources/sinks are thus negligible. At potentials between $-1.1\,\mathrm{V}$ and $-0.7\,\mathrm{V}$, the CO_2-to-bicarbonate reaction (c1) is slightly higher than the bicarbonate-to-carbonate reaction (c2) for stationary operation. This is caused by the good availability of CO_2 in the diffusion layer for this potential range. For more negative potentials, the c1 reaction becomes slower than c2: Here, CO_2 is depleted in the entire diffusion layer, and bicarbonate, which is produced by c1 and which is anyway present in the supplied electrolyte, can consume more of the ions.

For the dynamic operation, the situation changes. For the strongly negative potential region, OH^- consumption by c2 is much higher than for the c1 reaction. This is caused by the different time constants of these reactions. The c2 reaction is much faster due to a higher reaction rate constant and good availability of bicarbonate ions. This results in a domination of c2 reaction in dynamic operation and a large deviation from equilibrium concentrations of carbonate species. In the backward sweep after the reversal point, the consumption of hydroxide ions by c2 is decreasing strongly in the diffusion layer and becomes positive at a potential of $1.2\,\mathrm{V}$, so hydroxide ions are produced by c2. This effect is created by equilibration, i. e. the thrive to restore equilibrium concentrations of the carbonate system. At these conditions (referring to the local pH and CO_2 concentration), the equilibrium predominantly favors the formation of bicarbonate ions, so carbonate ions react to bicarbonate, and CO_2 reacts with released OH^- to bicarbonate.

In summary, due to a good availability of bicarbonate and a fast bicarbonate-carbonate buffer reaction, bicarbonate consumes most of the OH^- at low potentials, whereas it releases them at higher potentials again, when less OH^- is produced in dynamic operation.
In summary, due to a good availability of bicarbonate and a fast bicarbonate-carbonate buffer reaction, bicarbonate consumes most of the OH^- at low potentials, whereas it releases them at higher potentials again, when less OH^- is produced in dynamic operation.

Figure 3.6 compares the carbon efficiency, i.e., the ratio of the total electrochemical CO_2 consumption to the total CO_2 consumption over the entire diffusion layer thickness (Eq. 2.52). The absolute values of the consumption rates can be found in Figure A.4. CE is in the order of 0.5, i.e., chemical and electrochemical consumption are in the same order of magnitude. All values are further positive, which means that there is no release or source of CO_2 from decarbonisation of the $KHCO_3$ electrolyte. This effect has also been observed in gas diffusion electrodes[127] and is acutely exacerbated in planar electrodes due to low CO_2 concentrations. For the stationary case, in the high potential region $> -1\,\mathrm{V}$, CE is slightly less than 0.5 and nearly constant. In this potential region, the reaction rate of CO_2R is low and chemical CO_2 consumption takes place to consume these hydroxide ions from CO_2R and HER. With decreasing potential, CE reaches a maximum of 50% at a potential of $-1.3\,\mathrm{V}$. At this potential, the electrochemical CO_2 reduction has its maximum, and a value of 50% indicates that for each CO molecule produced, two CO_2 molecules are converted in the diffusion layer – one by electrochemical reduction and one by chemical reaction with a hydroxide ion. At low potentials, CE decreases further due to the limitation of CO_2 reduction and HER dominance. In this potential range, CO_2 is mainly consumed

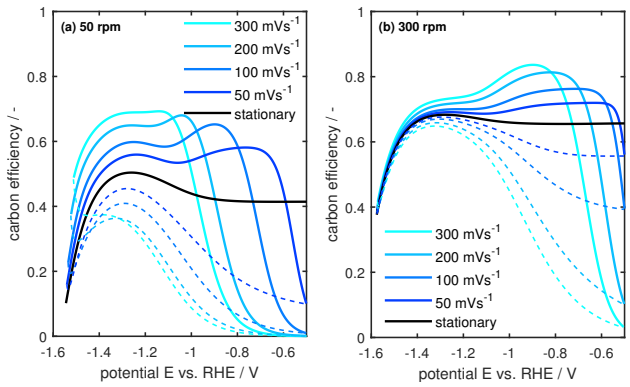

Figure 3.6: Carbon efficiency, i.e., ratio of electrochemical CO_2 consumption to chemical CO_2 consumption, in the diffusion layer along the potential for steady-state and for dynamic operation at different scan rates for (a) 50 rpm and (b) 300 rpm. Forward sweeps are shown in solid lines and backward sweeps in dashed lines. Conditions: CO_2 saturated 0.1 M $KHCO_3$ Potentials are corrected for iR-drop.

by the chemical reaction using the hydroxide ions released by HER, which further suppresses the electrochemical CO_2R.

The situation under dynamic operation is significantly different compared to stationary operation. For the forward sweep, electrochemical consumption exceeds that of chemical consumption in the medium potential range. Here, the Faradaic current of the CO_2R is strong as most of the OH^- ions are more rapidly consumed by the bicarbonate-to-carbonate reaction than the CO_2-to-bicarbonate reaction (see discussion above). The chemical consumption exceeds the electrochemical reaction for very negative potentials – similarly as for the stationary case – due to high HER and thus hydroxide production, which consumes fresh CO_2 entering the diffusion layer.

During the backward sweep, this accumulation of OH^- leads to high carbonation rates, thus CE drops to almost zero. This history and the ongoing balancing of the buffer also explain the very low values of CE at the beginning of the forward sweep. At low potentials $<-1.4\,\mathrm{V}$, CE decreases and continues to decrease further in the backward sweep at high scan rates, resulting in a significant hysteresis. The reason for the hysteresis effect is the readjustment of the carbonate equilibrium. This results in low values of the carbon efficiency for the backward sweep and a strong hysteresis in dynamic operation.

Interestingly, electrochemical CO_2 reduction is significantly more favored than carbonation when increasing rotation to $300\,\mathrm{rpm}$, as shown in Figure 3.6b. CE is also higher for steady state, with a value of about 65%. This is because the buffering is mainly done by the bicarbonate-to-carbonate reaction in this case. A thinner diffusion layer ensures high availability of bicarbonate ions and low concentrations of carbonate species which promotes high reaction rates of reaction c2 (see Figure A.4 in SI). For dynamic operation, the potential range where chemical CO_2 consumption is higher than the electrochemical one becomes smaller because the diffusion layer recovers much faster. For scans at $50\,\mathrm{mV\,s^{-1}}$, during the full scan, electrochemical CO_2 consumption is higher than the chemical one. In addition, for all scan rates, the maximum is shifted to more positive potentials. At high potentials, the CO_2 reduction is not transport-limited, and due to better transport, the local pH is not high, which prevents carbonation. These points strongly favor the electrochemical CO_2 reduction over the chemical consumption. Thus, either at low potentials, where high current densities can be achieved, higher values of the CE are reached due to better species transport.

I conclude that with higher scan and rotation rates, the efficiency of the CO_2 consumption can be pushed in favor of electrochemical CO_2 reduction. This can be reached due to a better transport of CO_2 and bicarbonate species and a fast reaction rate of the bicarbonate-to-carbonate reaction.

3.4.4 Faradaic efficiency

In the following, I discuss the practical impact of the complex influence of carbonation and species transport on electrochemical CO_2 reduction. The focus is on impact on catalyst characterization and performance assessment. The questions answered are whether dynamic operation or operation at thin vs. thick diffusion layers should be targeted.

The Faradaic efficiency characterizes the selectivity for the electrochemical CO_2R over HER. Figure 3.7 shows the simulated Faradaic efficiencies for $50\,\mathrm{rpm}$ and $300\,\mathrm{rpm}$ in stationary and dynamic operation. At high potentials, in all cases, high $\mathrm{FE_{CO_2R}}$ near 1 is reached for dynamic and stationary operation at low and higher rotation rates. This is maintained by high CO_2 concentrations and low reaction rates. At lower potentials, the Faradaic efficiencies decrease due to the transport-controlled limitation of CO_2R and the strong onset of HER. For low rotation rates and low potentials below $-1.4\,\mathrm{V}$, the Faradaic efficiency is higher for the dynamic vs. stationary operation. For dynamic operation at $-1.4\,\mathrm{V}$ (forward sweep), it is 10% higher. This is due to the slower depletion of CO_2 at the electrode, slightly lower pH values, and a higher carbon-efficiency of electrochemical over chemical CO_2 consumption. The $\mathrm{FE_{CO_2R}}$ in the backward sweep is slightly lower than that for stationary operation, caused by higher pH values shifting the CO_2 consumption towards chemical consumption. This results in lower CO_2 concentrations at higher

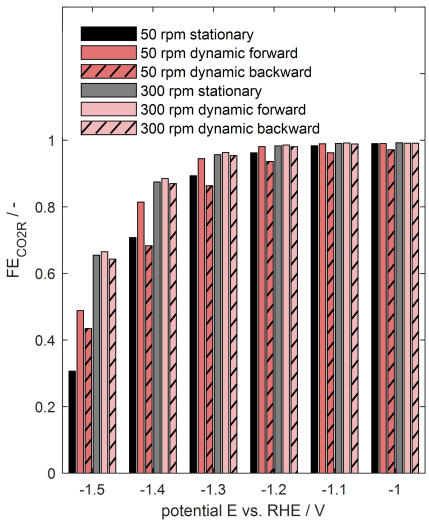

Figure 3.7: Simulated Faradaic efficiencies of electrochemical CO_2 reduction for stationary and dynamic operation for 50 and 300 rpm. Values for forward sweeps at $300\,\mathrm{mV\,s^{-1}}$ are shown without a pattern and values for backward sweep with a striped pattern. Conditions: CO_2 saturated 0.1 M $KHCO_3$ room temperature. Potentials are corrected for iR-drop.

potentials in the backward sweep. Increasing the rotation rate to $300\,\mathrm{rpm}$ further increases the $\mathrm{FE}_{\mathrm{CO_2R}}$. Improving the species transport increases the local CO_2 concentration and the efficiency of CO_2 consumption towards electrochemical consumption. However, at this rotation rate, the $\mathrm{FE}_{\mathrm{CO_2R}}$ for the dynamic and stationary analyses are almost the same. The differences in local conditions in this potential region are minor, and the transport processes are faster than the potential sweep. This reduces the impact of the scan rate and is reflected in very similar Faradaic efficiencies.
These observations show that the differences in the local state between the dynamic and the stationary operation result in a significant shift in the Faradic efficiency, if species transport is insufficient. It shows that from catalyst material characterization with high rotation rates, no conclusion for performance under mass transport influence can be made. For systems without transport limitation, dynamic characterization can be used to infer steady-state performance. Additionally, I showed that if species transport effects cannot be excluded, dynamic operation can help to shift the $\mathrm{FE}_{\mathrm{CO_2R}}$ to higher values. The improvement is strongly dependent on the time constants of transport processes compared to the time constants of the potential sweep and is only a snapshot of performance. The performance under steady-state conditions can differ significantly from this. Whether a permanent improvement of performance can be made with dynamic operation techniques has to be investigated in further studies.

3.5 Concluding remarks

This chapter used a dynamic model for electrochemical CO_2 reduction at silver electrodes to analyze the difference between steady-state and transient behavior systematically, and to unravel the impact of transport and carbonation on the performance of the silver electrode. The model was able to reproduce polarization curves and cyclic voltammograms with different scan rates and rotation rates, i.e., species transport influences. A high scan rate dependence on the current response was observed for low rotation rates. Such conditions can easily occur under real operating conditions, e.g., in flow cell setups. This sensitivity to scan rate results from species transport affecting several aspects of the system, namely CO_2 depletion, carbonate buffer reaction, and local pH evolution.
Under transport limitation, stationary operation suffers most from depletion of CO_2 at the electrode due to slow transport and increased chemical consumption of CO_2 by carbonation reaction. Applying high scan rates, Faradaic efficiency for CO_2R can be increased for the forward sweep. This is reached due to several effects: The holding times at low potential are much shorter and the CO_2 concentration at the electrode surface partially recovered by species transport during the backward sweep in dynamic operation. Thus, the concentration profile across the diffusion layer

is mainly influenced by the reaction history and the scan rate. Additionally, it is shown that the effect of carbonation is highly time-dependent. The reaction $HCO_3^- + OH^- \rightleftharpoons CO_3^{2-} + H_2O$ is much faster than the reaction $CO_2 + OH^- \rightleftharpoons HCO_3^-$ due to the good availability of bicarbonate compared to CO_2 in the electrolyte and a higher reaction rate constant of the former reaction. This results in a domination of this reaction in the buffer process and less consumption of CO_2 by the chemical reaction in dynamic operation. The carbon efficiency is increased significantly from $50\,\mathrm{rpm}$ to $300\,\mathrm{rpm}$. This is caused by better CO_2 transport to the electrode, a better transport of bicarbonate and carbonate ions which promotes the bicarbonate-to-carbonate reaction in the diffusion layer.

As species transport and carbonation effects can be easily detected by varying the scan rate, I propose such a test for catalyst research to ensure that the results contain negligible transport effects. Transport effects can easily be removed by increasing rotation rates in RDE setups. In contrast, when it is of interest to understand how the catalyst behaves during realistic conditions, where carbonation and species transport will lead to strongly different pH and local concentrations, the proposed low rotation rates and a variation in scan rate can be applied. I recommend replacing steady-state analysis with the dynamic analysis for RDE studies - with the choice of the appropriate rotation rate - because it is faster and less prone to failure in gas evolution reactions. Concluding, the CO_2 reduction in alkaline electrolyte has been shown as a system where electrolyte conditions may easily change and deviate from nominal conditions; these in turn can strongly impact performance and analysis results. This requires countermeasures as suggested here for adjusting proper analysis conditions.

4 CO_2 Reduction Enhancement with Metal-Organic Framework Coating[1]

In the previous chapter, it became evident that CO_2R at flooded planar electrodes suffers significantly from a depletion of CO_2 at the catalyst surface, caused by transport limitations and the chemical consumption of CO_2. The following section demonstrates how the coating of planar silver electrodes with the metal-organic framework UiO-67 (Universitetet i Oslo type 67) can enhance the local CO_2 concentration at the electrode and thereby increases the Faradaic efficiency for CO formation. A systematic modeling study discusses potential factors by which the MOF layer influences local reaction conditions, thereby revealing the main causes of the performance enhancement of the electrode with UiO-67 coating.

4.1 Introduction

Improving electrode performance and FE requires ongoing catalyst optimization, focusing on new, highly active materials. Among them metal oxides[172], metal alloys[173], single-atom catalysts[49], or metal-organic frameworks (MOFs)[174] are being studied. Metal-organic frameworks offer particular promise due to their large surface area, well-defined porous structure, and versatile tailoring options. They consist of an inorganic metal building block combined with an organic linker, forming highly crystalline two- or three-dimensional structures.[174, 175]
Several metal-organic frameworks have been investigated for electrochemical CO_2 reduction. The nature of active sites and their product selectivity is diverse. For instance, MOFs that exhibit high selectivity for CO production include Co-PMOF (polyoxometalate-metalloporphyrin organic framework), which has a FE_{CO} of over 94% across a wide potential range between -0.8 and $-1.0\,V$ vs. RHE, with a partial current density of -17 down to $-29\,mA\,cm^{-2}$.[176] Other examples include Re-SURFMOF (surface-grafted metal-organic frameworks with incorporated $ReL(CO)_2Cl$ (L=2,2'-bipyridine-5,5'-dicarboxylic acid), which demonstrates an FE_{CO} of 93%

[1] The work in this chapter was done in close collaboration with the Institute of Functional Interfaces, Department of Chemistry of Oxidic and Organic Interfaces, Karlsruhe Institute of Technology.
Results that do not correspond to my own work are marked accordingly

at $-2\,\mathrm{mA\,cm^{-2}}$ in acetonitrile[177] or the one-dimensional Ag-NIM-MOF (2-Nitroimidazole-based) that improves FE_{CO} from 79.4 to 94.5% compared to Ag nanoparticles, with a current density of $-28\,\mathrm{mA\,cm^{-2}}$ versus $-16.6\,\mathrm{mA\,cm^{-2}}$ at $-1.4\,\mathrm{V}$ vs. RHE[178].

To enhance selectivity towards more valuable products such as formate, methane, alcohols or C2+ products, Cu- or Cu_2O-MOFs are frequently employed.[86, 179–182] Cu_2O incorporated into Cu-MOF ($Cu_3(BTC)_2$) showed higher selectivity for methane from 3% for bare Cu_2O to 63.2% for Cu_2O@Cu-MOF at $-1.71\,\mathrm{V}$ vs. RHE. This improvement is attributed to the high CO_2 adsorption capacity and a lower charge-transfer resistance of the Cu_2O@Cu-MOF during CO_2R.[179] Copper naphthalenedicarboxylate, a 2D metal-organic framework, offers high selectivity for ethanol due to the high surface concentration of Cu+ species and provides beneficial electron density at the active sites, primarily influenced by the π-conjugated ligand of the organic linker.[180]

However, while metal sites within MOFs can contribute to electrochemical activity, the insulating nature of most pristine MOFs hinders effective electron transfer, limiting the amount of active sites and current density.[174, 175] Consequently, the current density is relatively low compared to the inner surface of the MOF in most of the available studies.

Many MOFs also show a high CO_2 uptake capacity at room temperature, attributed to the interaction between the large quadrupole moment of carbon dioxide and the framework and their well-suited pore sizes.[183] For example, MOF-200 exhibited a CO_2 adsorption of 55.4 $\mathrm{mmol_{CO_2}\,g_{MOF}^{-1}}$ at 50 bar and ambient temperature.[184] Even at low pressures, MOFs are able to store significant amounts of CO_2, as shown by mesoporous MIL-101(Cr), which adsorbed 10 $\mathrm{mmol_{CO_2}\,g_{MOF}^{-1}}$ at ambient pressure.[185] The adsorption capacity is 300 times greater than that of water. This elevated CO_2 uptake increases the local CO_2 concentration at the catalyst's active sites, which should increase selectivity for CO_2R over the competing HER.

Mukhopadhyay et al.[186] reported a 27-fold increase in CO_2 concentration compared to the bulk electrolyte when using a nitrile-modified UiO-66 MOF (Universitetet i Oslo type 66) coated on a Bi catalyst. This enhanced the partial current density for formic acid formation from -0.9 to $-2.4\,\mathrm{mA\,cm^{-2}}$ in an H-cell setup and from -26 to $-166\,\mathrm{mA\,cm^{-2}}$ in a GDE setup at $-0.9\,\mathrm{V}$ vs. RHE, with a Faradaic efficiency of approximately 90%.[186]

It is striking that most of the potential ranges analyzed are far more positive than the electrode potentials that are typically reached in GDEs operating at technically relevant current densities and where CO_2 transport limitations dominate.

In this study, an isoreticular series of Zr-based UiO-type framework was investigated due to its stability in acidic and basic environments. Preliminary tests showed that UiO-67 with zirconium as the metal node and biphenyl-4,4'-dicarboxylic acid (BPDC) as the linker gave the best results in terms of synthesis on silver plates used as substrate.

The preparation of the UiO-67 coatings on silver plates was carried out by the Institute of Functional Interfaces using a modified version of the process for producing oriented thin MOF films by the Vapor Assisted Conversion method.[187]

UiO-67 metal-organic framework is employed to enhance electrochemical CO_2 reduction at silver electrodes. The UiO-67 shows a larger surface area and pore volume compared to UiO-66 and is chemically and thermally stable in the same way.[188] Previous studies have shown that UiO-67 has high CO_2 uptake capacity of 1.17 $\mathrm{mmol_{CO_2}\,g_{MOF}^{-1}}$ at $100\,\mathrm{kPa}$[189] and can achieve high activity and selectivity for photocatalytical CO_2 reduction [190], making it a promising candidate for electrochemical CO_2 reduction.
In this study, UiO-67 will be investigated as a coating on planar Ag electrodes under CO_2-transport-limited conditions. Model-assisted analysis will clarify the effects of the MOF coating and assess the underlying causes of performance improvement. To the best of my knowledge, no study has yet investigated the impact of MOF layers on CO_2 reduction through simulation.

4.2 Experimental details

4.2.1 Synthesis of UiO-67/Ag system via Vapor Assisted Conversion[2]

The synthesis and coating preparation of UiO-67 MOF on the silver substrate was conducted by the Institute of Functional Interfaces, Department of Chemistry of Oxidic and Organic Interfaces, Karlsruhe Institute of Technology using Vapor Assisted Conversion, originally described by Virmani et al.[187] The concentrations of the building units were varied to investigate the influence of the MOF coating structure on electrode behavior. These concentrations are listed in Table 4.1 and serve as numerical identifiers for the corresponding sample names.

Table 4.1: Composition of precursor solution of different samples for the synthesis of UiO-67 via Vapor Assisted Conversion

Sample name appendix	Concentration $ZrOCl_2 \cdot 8\,H_2O$ / $\mathrm{mmol\,L^{-1}}$	Concentration BPDC / $\mathrm{mmol\,L^{-1}}$	Concentration acetic acid / $\mathrm{mmol\,L^{-1}}$
-07	0.7	0.7	142
-22	2.2	2.2	427
-66	6.6	6.6	1281

[2] Synthesis of UiO-67/Ag system was done by the Institute of Functional Interfaces, Department of Chemistry of Oxidic and Organic Interfaces, Karlsruhe Institute of Technology

4.2.2 Electrochemical characterization

Polarization curves, cyclic voltammetry, and double-layer capacitance measurements were conducted. A three-electrode configuration in a beaker-type cell with an electrolyte volume of $150\,\mathrm{mL}$ was used. A $1\,\mathrm{cm}^2$ silver plate (99.995% Ag, ChemPur) was used as the working electrode as a bare silver sample and the same silver plates with UiO-67 coating as described above. A platinum wire served as the counter electrode, and an Ag/AgCl electrode in saturated KCl_{aq} was used as the reference electrode. A Gamry Interface 1010E potentiostat was employed to apply the potential and measure the current density response. All potentials were corrected for uncompensated resistance after each run. Aqueous potassium bicarbonate solution ($KHCO_3$, BioUltra $>99.5\%$, Sigma Aldrich and deionized water, Merck MilliQ, $16\,\mathrm{M\Omega\,cm^{-1}}$) was used as electrolyte.
Before measurements, the electrolyte was purged with CO_2 ($\geq 99.995\%$, Air Liquide Deutschland GmbH) for $15\,\mathrm{min}$, and a CO_2 atmosphere was maintained in the cell gas volume during the experiment. The electrode potentials were converted to the RHE scale according to Equation 4.1, with a pH value of 6.8 for the electrolyte bulk.

$$E_{\mathrm{RHE}} = E_{\mathrm{Ag/AgCl}} + 0.059\,\mathrm{V} \cdot \mathrm{pH} + 0.1976\,\mathrm{V} \tag{4.1}$$

Electrochemical double-layer capacitances were determined by conducting cyclic voltammetry in the non-Faradaic potential region between $-0.37\,\mathrm{V}$ and $-0.27\,\mathrm{V}$ for Ag/UiO$-$67 samples and from $-0.025\,\mathrm{V}$ to $-0.125\,\mathrm{V}$ vs. Ag/AgCl for bare silver electrodes (Appendix, Figure A.8). Scan rates of $\nu = \{10, 20, 30, 40, 50, 60, 70, 80, 100, 120, 140, 160, 180, 200\,\mathrm{mV\,s^{-1}}\}$ were applied for five cycles each.
Chronoamperometry for product analysis was conducted in a low-volume H-type cell (Pine Research) with a catholyte chamber volume of $16\,\mathrm{mL}$ at potentials of $-0.6\,\mathrm{V}$, $-0.8\,\mathrm{V}$, $-1.0\,\mathrm{V}$, $-1.2\,\mathrm{V}$, and $-1.4\,\mathrm{V}$ vs. RHE. The anolyte and catholyte compartments were separated by a glass frit with a porosity of $4\,\mu\mathrm{m}$ to $8\,\mu\mathrm{m}$. A platinum mesh served as the counter electrode, and a reversible hydrogen electrode (Mini-HydroFlex, Gaskatel) was used as the reference electrode. Before measurements, the $0.1\,\mathrm{M}$ $KHCO_3$ electrolyte in the catholyte chamber was purged with CO_2 for $15\,\mathrm{min}$, and during measurements, a CO_2 gas flow of $6.7\,\mathrm{mL\,min^{-1}}$ was continuously bubbled into the electrolyte through a glass frit at the cathode side. Product gases were quantified by online gas chromatography, with samples analyzed every $6.5\,\mathrm{min}$ (Figure A.7, Supporting Information). A GC-2023 (Shimadzu) with a BID detector and Hayesep N 100/80 and Hayesep Q 80/100 columns was used to detect CO, H_2, and CH_4. The columns were maintained at a constant temperature of $50\,^{\circ}\mathrm{C}$, and helium was used as the carrier gas. The Faradaic efficiency of the product gas j was calculated by Equation 4.2:

$$\mathrm{FE}_j = \frac{x_j \cdot z_j \cdot \mathrm{F} \cdot \dot{V} \cdot p}{\overline{I} \cdot \mathrm{R} \cdot T} \tag{4.2}$$

where x_j is the volume fraction of the gaseous product j, z_j is the number of electrons per mole needed to form product j, F is the Faraday constant ($96\,485\,\mathrm{C\,mol^{-1}}$), $\dot{V}$ is the volumetric flow rate, p is the ambient pressure, $\overline{I}$ is the average current calculated by the mean value over the last $100\,\mathrm{s}$ before each sample loop injection, R is the universal gas constant ($8.314\,\mathrm{J\,mol^{-1}\,K^{-1}}$), and T is the ambient temperature.
After holding the potential for $1\,\mathrm{h}$, the chronoamperometry measurement was stopped, and samples from the anolyte and catholyte compartments were collected for analysis. These samples were analyzed using high-performance liquid chromatography (Vanquish HPLC, ThermoFisher) equipped with a HyperREZ™ XP carbohydrate-H^+ LC column. A $10\,\mu\mathrm{L}$ aliquot of each sample was injected into the column, and $5\,\mathrm{mM}$ H_2SO_4 in water was used as eluent. The flow rate was set to $0.6\,\mathrm{mL\,min^{-1}}$, with the column maintained at $55\,^\circ\mathrm{C}$, and UV-Vis detection at a wavelength of $210\,\mathrm{nm}$. The Faradaic efficiency for the liquid products i was determined by Equation 4.3:

$$\mathrm{FE}_i = \frac{N_i \cdot z_i \cdot \mathrm{F}}{Q_{\mathrm{total}}} \tag{4.3}$$

where Q_{total} is the total charge transferred during the measurement, N_i is the number of moles of the liquid product i, and z_i is the number of electrons per mole needed to form product i.
Electrochemical impedance spectroscopy measurements were conducted for each cyclic voltammetry experiment before each scan rate variation and after each chronoamperometry measurement to determine the uncompensated resistance of the iR-drop correction of the reference electrode potential. An AC voltage amplitude of $7\,\mathrm{mV_{rms}}$ was applied at an underlying DC voltage of $0\,\mathrm{V}$ vs. RHE over a frequency range from $100\,\mathrm{kHz}$ to $0.5\,\mathrm{kHz}$.

4.3 Model details

The model presented in Chapter 3 was modified to evaluate the influence of the UiO-67 layer on CO_2 reduction. For this, a porous layer was incorporated in front of the electrode to represent the MOF coating on its surface (Figure 4.1). In this modified framework, adjustments were made to the transport processes as well as to the chemical and electrochemical reactions, as outlined below and listed in Table 4.2.
Within the porous UiO-67 layer, reversible chemical adsorption and desorption of CO_2 are assumed to occur, in order to describe the storage capacity within the inner structure of the MOF:

$$\mathrm{CO_{2(diss)}} + [\,]_{\mathrm{MOF}} \rightleftharpoons \mathrm{CO_{2(ads),MOF}}. \tag{4.4}$$

The reaction rate of CO_2 adsorption and desorption r_{MOF} was calculated according to Eq. 4.5. The rate constants for adsorption was assumed to be sufficiently fast to maintain equilibrium.

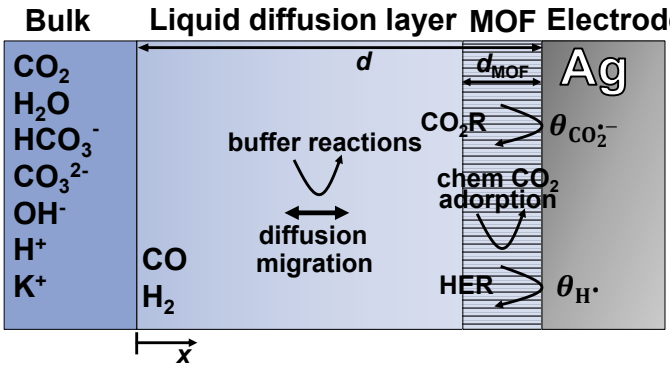

Figure 4.1: Model representation for the CO_2R at planar silver electrode coated with MOF layer.

The position of this equilibrium was defined by the equilibrium constant K_{MOF} (Eq. 4.6). The parameter K_{MOF} was adjusted such that the initial surface coverage of adsorbed CO_2 θ_{CO_2} matched the activity of dissolved CO_2 in the electrolyte (Table 4.3). This enables a direct comparison between the CO_2 availability at the MOF-coated and uncoated electrodes. The area-specific surface area of the MOF a_{MOF} was estimated based on the BET surface area[188] and crystallographic density of UiO-67.

The transport of the dissolved species was described analogously to that in the diffusion layer of the electrolyte, including diffusion and migration while incorporating the effect of porosity and effective diffusion coefficients for the porous medium (Eqs. 4.9 and 4.11). It should be noted that the assumption of the same effect of porosity on the transport for all species represents a simplification in the context of MOF structures. In reality, the impact of the pore structure on transport and accessibility of pores depends strongly on the molecular size of the individual species and their interactions with the pore environment.[191] In this model, this effect was explicitly considered only for CO_2, by introducing an adjustment parameter $f_{D_{CO_2}}$ to adjust the effective diffusion coefficient (Eq. 4.10).
In addition to the CO_2 storage and impact on transport, the MOF layer may also affect the electrochemically active surface area and modulate the kinetics of HER. These effects were incorporated via the adjustment parameters f_{ECSA} and f_{HER} (Eq. 4.12-4.15).

In the first stage of parameter identification, the kinetic parameters of the electrochemical reactions, along with the diffusion layer thickness, were optimized using the experimentally obtained polarization curve and the FE_{CO}-potential curve for the bare silver electrode. The optimization procedure followed the methodology described in section 3.2.
In the second stage, the adjustment parameters representing the influence of the MOF layer were calibrated through parameter optimization based on the polarization and FE_{CO}-potential curves

Table 4.2: Model equations for MOF model

MOF layer		
Reaction rate for chemical CO_2 adsorption in MOF layer	$r_{\text{MOF}} = k_{\text{f,MOF}} \cdot a_{\text{MOF}} \cdot c_{\text{CO}_2} \cdot \theta_{[\,]_{\text{MOF}}} - k_{\text{b,MOF}} \cdot a_{\text{MOF}} \cdot \theta_{\text{CO}_2}$	(4.5)
Reaction rate constant for chemical CO_2 adsorption and desorption in MOF layer	$K_{\text{MOF}} = \dfrac{k_{\text{f,MOF}}}{k_{\text{b,MOF}}} f_{\text{K}_{\text{MOF}}}$	(4.6)
Balance of adsorbed CO_2 in MOF layer	$\dfrac{\partial \theta_{\text{CO}_2}}{\partial t} = \dfrac{1}{\Gamma^{\text{MOF}}} r_{\text{MOF}}$	(4.7)
Reaction rate for first step of electrochemical CO_2 reduction into CO	$r_{\text{CO}_2\text{R},1} = k_{\text{f,CO}_2\text{R},1} \cdot \exp\left(\dfrac{-(1-\alpha_{\text{CO}_2\text{R}})\text{F}}{\text{R}T}\eta_{\text{CO}_2\text{R}}\right) \theta_{\text{CO}_2,\text{surf}}\, \theta_{[\,]} - k_{\text{b,CO}_2\text{R},1} \cdot \exp\left(\dfrac{\alpha_{\text{CO}_2\text{R}}\text{F}}{\text{R}T}\eta_{\text{CO}_2\text{R}}\right) \cdot \theta_{\text{CO}_2^{-}\bullet}$	(4.8)
Molar transport flux of species i	$N_i = -D_i^{\text{liq}} \varepsilon^{1.5} \nabla c_i - z_i \dfrac{D_i^{\text{liq}} \varepsilon^{1.5}}{\text{R}T} \text{F} c_i \nabla \phi$	(4.9)
Molar transport flux of CO_2	$N_{\text{CO}_2} = -f_{\text{D}_{\text{CO}_2}} D_{\text{CO}_2}^{\text{liq}} \varepsilon^{1.5} \nabla c_{\text{CO}_2}$	(4.10)
Balance of species i with transport and sources by chemical reactions L and adsorption in MOF	$\varepsilon \dfrac{\partial c_i}{\partial t} = -\nabla N_i + \sum_{i=1}^{L} \nu_{i,j} r_j + \nu_{i,\text{MOF}} r_{\text{MOF}}$	(4.11)
Reaction rate for first step of electrochemical CO_2 reduction	$r_{\text{CO2R,1,MOF}} = r_{\text{CO2R,1}} \cdot f_{\text{ECSA}}$	(4.12)
Reaction rate for first step of electrochemical CO_2 reduction	$r_{\text{CO2R,2,MOF}} = r_{\text{CO2R,2}} \cdot f_{\text{ECSA}}$	(4.13)
Reaction rate for Volmer step of HER	$r_{\text{HER,1,MOF}} = r_{\text{HER,1}} \cdot f_{\text{HER}} \cdot f_{\text{ECSA}}$	(4.14)
Reaction rate for Heyrovsky step of HER	$r_{\text{HER,2,MOF}} = r_{\text{HER,2}} \cdot f_{\text{ECSA}}$	(4.15)

measured for the UiO-67-22 coating.

The identification of these parameters, followed by an evaluation of their individual impacts on electrode performance by a systematic variation of each single parameter (Figure A.10 in the SI), enables a detailed interpretation of the UiO-67 coating's role and elucidates its contribution to the overall electrochemical CO_2R performance.

4.4 Results and discussion

The electrochemical activity of the UiO-67 coated silver electrode for electrochemical CO_2 reduction was investigated by cyclic voltammetry, polarization curves, and product analysis with GC and HPLC. This analysis evaluates the coating's effect on current density, overpotentials, and Faradaic efficiency.

Figure 4.2a compares the cyclic voltammograms for a scan rate of $200\,\text{mV}\,\text{s}^{-1}$. The bare silver electrode exhibits a slightly earlier onset potential but a less pronounced increase in cathodic

Table 4.3: Model parameters and variables of planar model coated with MOF layer

Parameter/Variable	Symbol	Value	Unit	Source
Geometrical surface area of electrode	A_{geom}	1×10^{-4}	m^2	
Internal ohmic resistance	R_{int}	20	Ω	b
Liquid diffusion layer thickness	d	72.6×10^{-6}	m	c
MOF layer thickness	d_{MOF}	15×10^{-6}	m	b
Reaction rate constant for forward reaction of electrochemical CO_2 adsorption	$k_{0,\mathrm{f,CO2R},1}$	5.443×10^{-6}	$\mathrm{mol\,m^{-2}\,s^{-1}}$	c
Reaction rate constant for forward reaction of electrochemical CO desorption	$k_{0,\mathrm{f,CO2R},2}$	9.966×10^{-2}	$\mathrm{mol\,m^{-2}\,s^{-1}}$	c
Reaction rate constant for forward reaction of electrochemical H_2O adsorption (Volmer step)	$k_{0,\mathrm{f,HER},1}$	5.550×10^{-7}	$\mathrm{mol\,m^{-2}\,s^{-1}}$	c
Reaction rate constant for forward reaction of electrochemical H_2 desorption (Heyrovsky step)	$k_{0,\mathrm{f,HER},2}$	9.975×10^{-4}	$\mathrm{mol\,m^{-2}\,s^{-1}}$	c
Charge transfer coefficient for CO_2 reduction	$\alpha_{\mathrm{CO_2R}}$	0.504	-	c
Charge transfer coefficient for hydrogen evolution reaction	α_{HER}	0.700	-	c
Concentration of surface adsorption sites in MOF	Γ^{MOF}	0.704	$\mathrm{mol\,m^{-3}}$	a
Area specific surface area of MOF	a_{MOF}	1.5×10^4	$\mathrm{m^2\,m^{-2}}$	[188]
Reaction rate constant of chemical CO_2 adsorption in MOF layer	$k_{\mathrm{f,MOF}}$	1×10^5	$\mathrm{s^{-1}}$	a
Equilibrium constant of chemical CO_2 adsorption/desoption in MOF layer	K_{MOF}	1.035×10^{-3}	$\mathrm{m^3\,mol^{-1}}$	a
Parameter for the increase in the diffusion coefficient of CO_2	$f_{\mathrm{D_{CO_2}}}$	2.829	-	c
Parameter for the increase in ECSA	f_{ECSA}	1.508	-	c
Parameter for the increase/decrease in HER	f_{HER}	1.085	-	c
Parameter for the increase/decrease of Equilibrium constant of chemical CO_2 adsorption	$f_{\mathrm{K_{MOF}}}$	8.010	-	c

[a] assumption, [b] measured, [c] model parametrization to experiments.

current density at potentials between -0.5 and $-1.0\,\mathrm{V}$ compared to the MOF-coated samples. The electrochemical CO_2 reduction is known to have its highest activity in this potential range due to high CO_2 availability.[37, 43] At more negative potentials, CO_2 reduction is limited by the mass transport of CO_2 to the electrode surface, visible in the small plateau at approximately $-1.12\,\mathrm{V}$ for the bare silver electrode. At this point, HER dominates.[134] For the UiO-67-22 coating, this plateau is less pronounced, and the absolute current density in the CO_2 reduction potential regime is highest for the UiO-67-06 and UiO-67-22 samples prepared with low and intermediate precursor concentrations. This may indicate that the coated electrodes exhibit higher selectivity for electrochemical CO_2 reduction. This hypothesis will be examined below through product analysis. The CVs also suggest that MOF does not contribute significantly to a higher ECSA, because the observed current densities are only slightly higher than those of the silver electrode. The same trend is observed for the stationary polarization curves shown in Figure 4.2b. Comparing the polarization curves of the different samples, most curves are nearly identical, reaching similar total current densities. Only UiO-67-07 exhibits an earlier onset potential, indicating a greater catalytic activity in the intermediate potential range between -0.4 and $-1.0\,\mathrm{V}$ vs. RHE.

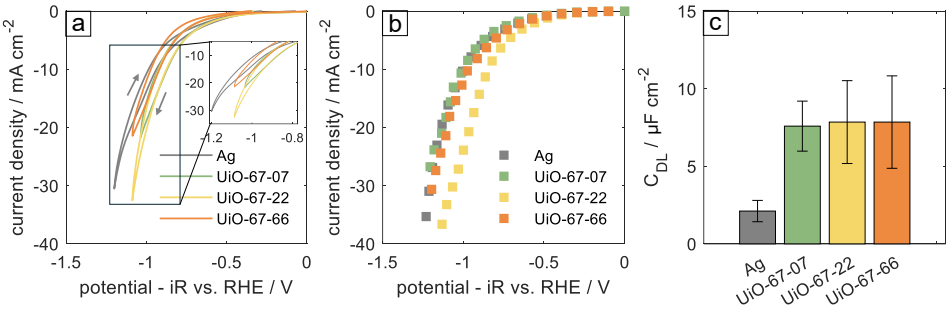

Figure 4.2: (a) Cyclic voltammogram with scan rate of $200\,\mathrm{mV\,s^{-1}}$ with zoom inset and (b) polarization curve of a bare silver electrode (Ag) and UiO-67 coated silver electrodes with different precursor concentrations in 0.1 M $KHCO_3$. All potentials were corrected for iR-drop. (c) Electrical double-layer capacitance for different electrode samples extracted from cyclic voltammetry measurements in the non-Faradaic potential region.

To confirm that the MOF coating does not lead to an increase in electrochemically active surface area, measurements of the electrochemical double-layer capacitance were conducted. UiO-67 coated electrodes show an increase in their capacitance from $2.5\,\mu\mathrm{F\,cm^{-2}}$ for bare silver to approximately $7\,\mu\mathrm{F\,cm^{-2}}$ (Figure 4.2c). In contrast, the BET surface area of UiO-67 is reported to be approximately $2500\,\mathrm{m^2\,g^{-1}}$.[188] Assuming a crystallographic density of $7.24 \times 10^5\,\mathrm{g\,m^{-3}}$, this corresponds to a specific surface area of about $1.8 \times 10^4\,\mathrm{m^2\,m^{-2}}$ for a $10\,\mu\mathrm{m}$-thick layer. Consistent with this, MOFs containing electrochemically active metal sites typically exhibit markedly higher double-layer capacitances on the order of $10\,\mathrm{mF\,cm^{-2}}$ as a consequence of their high internal surface area.[192, 193]
The comparatively low capacitance observed for UiO-67 coating in this study, therefore indicates that, under the investigated conditions, the framework does not contribute significantly through electrochemically active sites.

By reproducing the experimental data using the developed simulation model and performing parameter identification, valuable insights can be gained into the mechanistic role of the MOF layer and its contribution to the changes observed in the polarization curve and Faradaic efficiency.

Figure 4.3 shows the product distribution as a function of potential for the bare silver and the most promising UiO-67 coatings UiO-67-07 and UiO-67-22. The Faradaic current j_F was calculated by multiplying the total current density at each potential by the Faradaic efficiency of each product. The bare silver electrode shows high FE for the HER in both high and low potential ranges. At high potentials, HER is dominant due to its higher standard potential. At a potential of $-1.0\,\mathrm{V}$ vs. RHE, CO_2 reduction reaches its maximum in FE, then decreases at lower potentials due to a stronger decrease in Faradaic current for HER. At negative potentials, formic acid is also produced in small amounts. This behavior is sometimes observed on planar electrodes at very negative

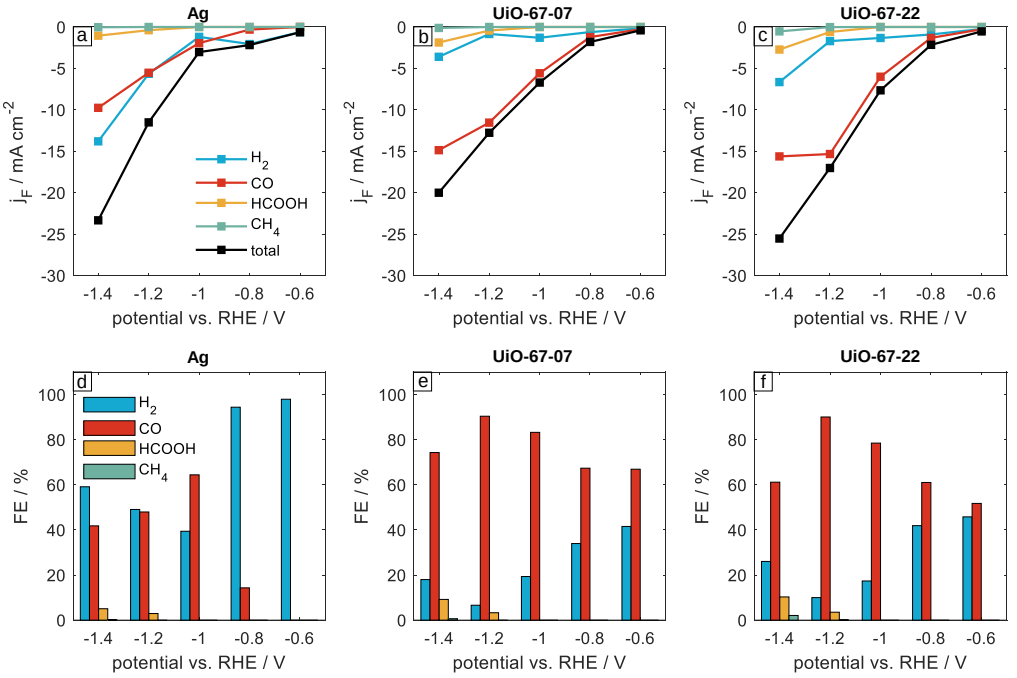

Figure 4.3: Faradaic current density j_F for hydrogen, carbon monoxide, formic acid and methane for (a) bare silver electrode (Ag) and (b)-(c) UiO-67 coated silver electrodes with different precursor concentrations and Faradaic efficiency for (d) bare silver electrode (Ag) and (e)-(f) UiO-67 coated silver electrodes with different precursor concentrations.

potentials, where electrodes suffer from CO_2 depletion strongly.[43]
Integrating a UiO-67 coating significantly increases the FE for CO production across all investigated potentials, e.g., from 0% to around 60% at $-0.6\,\mathrm{V}$ and from 50% to 90% at $-1.2\,\mathrm{V}$ vs. RHE. At the same time, HER is suppressed across the entire potential range, showing lower absolute Faradaic currents.
When comparing the UiO-67-07 and UiO-67-22 samples, it becomes evident that varying the precursor concentration has little impact on the electrochemical performance, resulting in nearly the same current densities and Faradaic efficiencies. UiO-67-07 exhibits a slightly higher FE_{CO}, particularly at $-1.4\,\mathrm{V}$. As the differences among the coatings are small, they were not included in the subsequent simulation study.

The parameter identification was performed based on steady-state simulations of the polarization and potential-FE_{CO} curves and successfully reproduced the experimentally observed increase in both absolute current density and FE_{CO} caused by the presence of the MOF layer, compared to the bare silver electrode (Figure 4.4).To further elucidate and quantify the influence of the individual

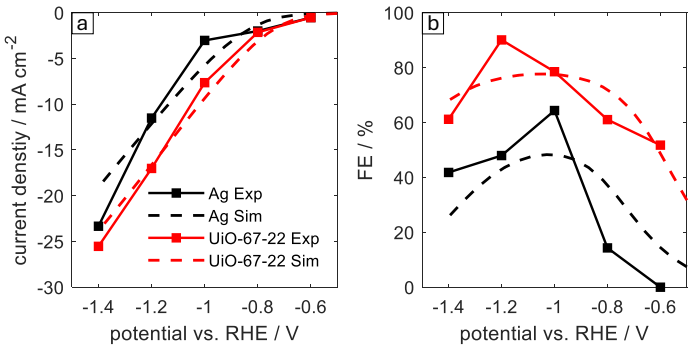

Figure 4.4: Experimental and simulative polarisation curve and FE_CO of CO_2R at bare Ag and UiO-67-22 sample. Dotted lines show simulated curves.

parameters, a systematic variation of each single parameter was conducted, the results of which are presented in Figure A.10 of the Supporting Information.

Figure 4.4 shows that the change in performance introduced by the MOF layer can be captured reasonably well, at least in its fundamental features. The slight increase in current density across the entire potential range is reproduced by the simulation (Figure 4.4 a). In addition, the Faradaic efficiency exhibits a significant shift toward higher values, which is likewise reflected in the model (Figure 4.4 b). The identified parameters indicate that the observed change in performance predominantly arises from an enhanced chemical CO_2 adsorption within the MOF layer by a factor of 8.01 (see Table 4.3). The enhancement particularly promotes FE_{CO} in the potential region above $-0.9\,\mathrm{V}$, while the overall current density remains nearly unchanged at more negative potentials. This trend is in good agreement with the experimental data. Furthermore, the effective transport of dissolved CO_2 within the MOF layer is estimated to increase by a factor of approximately 2.83. This enhancement affects the regime of highly negative potentials ($< -0.85\,\mathrm{V}$), where mass transport limitation of CO_2 becomes significant. Under these conditions, the facilitated CO_2 transport results in higher FE_{CO} values and an increased total current density. The two additional model parameters, f_{HER} and f_{ECSA}, appear to be only marginally affected by the presence of the MOF layer. The simulation indicates an increase in the electrochemically active surface area by a factor of 1.51, which is in the same order of magnitude as the experimentally determined values of the double-layer capacitance. This finding supports the assumption that the inner surface of the MOF does not exhibit significant electrochemical activity. Furthermore, the model suggests that the MOF layer does not alter the intrinsic kinetics of the HER with a value of 1.08 for f_{HER}.

4.5 Concluding remarks

The electrochemical activity of UiO-67-coated silver electrodes for CO_2 reduction was thoroughly investigated using electrochemical polarization curves, cyclic voltammetry, and product analysis combined with a macrokinetic model. The wide potential range applied between -0.6 and $-1.4\,\mathrm{V}$ vs. RHE spans both the kinetically controlled and transport-limited regimes of CO_2 reduction. The results demonstrated that the coating significantly enhances the performance of silver electrodes by increasing the Faradaic efficiency for CO production in the whole investigated potential range. The simulations showed, that the improvement of FE_{CO} is predominantly based on the increase in the CO_2 adsorption in the MOF layer, leading to higher CO_2 activity at the electrode surface, which enhances the reaction rate for CO_2 reduction mostly in the kinetically controlled potential region of CO_2R. The simulation further suggests that CO_2 transport within the MOF layer is enhanced. As a result, in the more negative potential regime where CO_2 reduction is limited by mass transport, both the absolute cathodic current and FE_{CO} are increased. Both experiments and simulations indicate that the MOF does not significantly contribute to the ECSA.

This study highlights the potential of MOF-based systems for optimizing CO_2 availability at the electrode surface, thereby enhancing CO_2 reduction performance through a combination of experimental and simulation-based investigations. For future work, a more detailed physical characterization of the MOF coating should be conducted to determine the properties of its porous structure and to reduce the assumptions in the physico-chemical model. In addition, future studies should address the long-term stability of the MOF layer under electrochemical operating conditions.

This study also makes it clear that, even with high-performance coatings, the current density of CO production is quickly limited by the planar structure and thick liquid diffusion layer in front of the electrodes. The next chapter describes how gas diffusion electrodes can be optimized to reach technically relevant current densities of CO_2R.

5 CO_2 Reduction in Ag Gas Diffusion Electrodes[1]

In the research of catalyst and electrode material screening and optimization, as described in Chapter 4, planar model electrodes are often used. These electrodes are typically characterized by small geometric surface areas and their bulk characteristic. However, to develop a practical technical process, technical electrodes are required. These electrodes offer significantly higher electrochemical surface areas due to their larger geometric dimensions and porous structures. In the context of CO_2R, the use of gas diffusion electrodes holds great promise. They improve CO_2 availability and by this achieve industrially relevant current densities of $\geq 200\,\mathrm{mA\,cm^{-2}}$. [194]
Although the basic electrochemical and chemical reactions and transport processes remain the same when using an identical catalyst and electrolyte, the behavior of the GDE differs significantly from that on planar electrodes. This is mainly due to the local potential and current distribution in the porous electrode, the presence of the gas/liquid interface, and the varying transport distances depending on the selected process and electrode parameters.
How exactly local states and electrolyte intrusion in GDEs influence their performance will be clarified in the following chapter.

5.1 Introduction

In gas diffusion electrodes, the CO_2 gas is supplied from one side of the electrode, and electrolyte is supplied from the other side as mentioned above (Figure 2.8C). Both phases converge at distinct locations within the gas diffusion electrode, where they form the gas/electrolyte interface. This ensures a high availability of CO_2 over a wide catalyst area in the GDE and mitigates the CO_2 transport limitation in the electrolyte-flooded part of the GDE caused by the low CO_2 solubility in the electrolyte. However, the quantitative description, adjustment, and prediction of GDE performance become considerably more complex compared to a flat or flooded porous electrode

[1] Parts of this chapter have been published in Dorner et al., J. CO2 Util., 2025 [87]
Experimental investigations were conducted jointly with Jens Osiewacz during a research stay at Clausthal University of Technology.

due to the high sensitivity to the electrolyte intrusion state in the GDE, which also depends on the porous electrode structure.[147] This motivates intensive research to understand and design optimal GDE compositions and structures.[127]

Several studies investigated the impact of electrode structure of carbon-based electrodes on electrolyte distribution, flooding behavior, and performance: A recent study found that thicker MPLs reduced Faradaic efficiency for CO (FE_{CO}) at low current densities due to increased CO_2 transport resistance, but that they improve performance at higher current densities by resisting flooding and salt precipitation.[195] Additionally, cracks in the MPL were shown to mitigate the decline in the FE_{CO} at higher current densities by enhancing access to fresh electrolyte solution, allowing deeper electrolyte penetration into the microporous layer of the electrode structure. This increased the overall capacity to store salt precipitates and decreased the blockage of the electrochemically active surface area.[196]
The hydrophobicity of the electrode is adjusted by adding hydrophobic polymers like PTFE. Yet, PTFE may cover the catalyst surface and is thus expected to reduce the ECSA.[32] However, opposing trends, such as an increase of ECSA with higher PTFE amounts, have also been observed.[197] Both observations suggest a complex interplay among electrolyte intrusion, catalyst surface area, surface roughness, PTFE coverage, and PTFE degradation, as all of them impact the effective electrochemically active surface area. This interaction is not yet fully understood, hampering knowledge-driven design of electrodes and operating conditions for a high and long-term stable performance of CO_2R.
Heßelmann et al.[198] proposed in a simulative study with a one-dimensional steady-state model that increasing the porosity of a 3 µm thick catalyst layer and reducing the catalyst loading results in a decrease in FE_{CO}.[198] This implies that the decrease in surface area outweighs the benefits gained from improved mass transport in their case.
All studies mentioned before[32, 195–198] provide insights into electrolyte intrusion-related processes that influence Faradaic efficiency and current density at a given potential for carbon-based electrodes.

For carbon-free silver electrodes, transport processes, electrolyte distribution, and reaction interaction have been extensively investigated for these electrodes, both experimentally and via simulations in the context of ORR. A critical challenge is the slow water transport in and close to these relatively thick electrodes, resulting in elevated ion concentrations within the reaction zone of the electrode.[155] Utilizing electrochemical impedance spectroscopy in combination with kinetic modeling, Röhe et al.[160] were able to detect a strongly heterogeneous flooding behavior, discernible as flattened semicircles in the Nyquist plot.[160] This behavior signifies the absence of a straight electrolyte/gas front within the electrode, distinguishing it significantly from the state in carbon-based electrodes. Instead, it displays a pore-selective, capillary force-driven intrusion of the electrolyte, which is promising for high gas/liquid interfaces. Such strong inhomogeneity

is also expected to prevail for CO_2R; it remains unanswered so far how the inhomogeneity in electrolyte distribution affects CO_2R.
The characteristics of alkaline electrolyte intrusion into carbon-free GDEs were visualized experimentally by Paulisch et al.[199] for ORR, and by Hoffmann et al.[200] for CO_2R using *operando* laboratory x-ray imaging. In the latter study, it was found that a GDE with $97\,\mathrm{wt}\%$ Ag content ($3\,\mathrm{wt}\%$ PTFE) was more beneficial for CO_2R than one with $92\,\mathrm{wt}\%$ Ag. This was attributed to a larger triple-phase boundary during operation, resulting in better CO_2 availability.[200]
Osiewacz et al.[129] developed a comprehensive model for analyzing these electrodes in CO_2R. They revealed that electrodes with $97\,\mathrm{wt}\%$ Ag primarily suffer from slow CO_2 mass transport and a strong carbonation reaction, resulting in low carbon efficiency and a low Faradaic efficiency at high current densities $\geq 300\,\mathrm{mA\,cm^{-2}}$. They also predicted with their model that thinner electrodes may become more selective for CO production.[129]
When comparing carbon-free with carbon-based electrodes, Baumgartner et al. deemed the carbon-free electrode unsuitable for CO_2 reduction due to its significantly higher susceptibility to flooding.[201] However, a systematic investigation of the influence of electrode and operating parameters on carbon-free GDEs is still pending. The impact of electrolyte intrusion and distribution on electrode performance remains an open question so far. Yet, this aspect is crucial for improving these electrodes to make them suitable for CO_2R.

In this chapter, I reveal how operating and design parameters impact the performance by changing the intrusion of the electrolyte into Ag-GDEs. Operating parameters and electrode composition are systematically varied, and their effect is studied. The parameters include the differential pressure between gas and electrolyte sides, electrode thickness, and PTFE content. These parameters were selected based on their reported relevance to process performance in prior studies[101, 129, 202] and their practical adaptability. In these studies, their primary influence is attributed to effects on the CO_2 availability in the electrode, transport distance for ions, and electrolyte distribution within the electrode. To gain a comprehensive understanding of the relation between these parameters, intrusion state, and performance, I utilize a physicochemical model that is parameterized and validated by experiments (Figure 5.1). The model provides detailed insights into current-dependent profiles of local species concentrations, pH gradients, Faradaic efficiencies, and their impact on electrode potential. This investigation sheds light, mechanistically and quantitatively, on limiting processes within these electrodes, offering valuable insights for optimization of electrode design and operation. To the best of my knowledge, such a rigorous analysis of electrolyte intrusion and distribution within such GDEs and its model-assisted interpretation is novel and has not yet been addressed in the literature.

5.2 Experimental section

5.2.1 Electrode preparation[2]

Carbon-free Ag-GDEs were produced according to the procedure described by Franzen et al.[202] by using the wet spraying method developed by Mousallem et al..[202, 203] The PTFE content was adjusted to values of 1, 2, and $3\,\mathrm{wt\%}$ PTFE in the electrode by varying PTFE proportion in the suspension recipe. To change the electrode thickness of the GDEs, the number of coating layers was changed from 80 layers as a standard thickness to values of 50 and 110. The resulting thickness was determined with a thickness dial gauge (FD 50, Käfer GmbH) by averaging between six measuring points. Electrode details can be found in Table 5.1.

5.2.2 Electrochemical characterization and product analysis[3]

The GDEs were characterized in a commercial flow cell (Micro Flow Cell V1_2017, ElectroCell) with an active electrode area of $10\,\mathrm{cm^2}$. A new GDE was used for each polarization curve in order to avoid changes due to ageing. A three-electrode setup was used, employing a flat IrO_2 coated electrode as counter electrode and a micro-Ag/AgCl electrode (ET072-1, eDAQ) as reference. Catholyte and anolyte chambers were separated by an anion exchange membrane (fumasep®FAA-3-130-PK, fumatech), and were supplied with 1 M $KHCO_3$ ($>99\,\mathrm{wt\%}$, Carl Roth) electrolyte at $960\,\mathrm{mL\,min^{-1}}$. CO_2 (99.995%, Linde) was supplied to the gas side of the GDE at a flow rate of $83.58\,\mathrm{mL\,min^{-1}}$. Pressure in the electrolyte chambers was set to 1 bar, while the gas pressure was varied between experiments from 1.02 to 1.1 bar. Both pressures were controlled by control circuits, employing needle valves in the gas outlet stream and pressure sensors at the cell inlets. The temperature was not externally controlled. Galvanostatic current was supplied by an electrochemical workstation (ZenniumPro, Zahner) from 10 to $200\,\mathrm{mA\,cm^{-2}}$; the polarization curves used the cathode potential obtained after keeping a steady current for 40 min at each current density. The cathode potential was measured continuously against the reference electrode, which was placed at the catholyte side of the cell and time-averaged for each current density after being iR-corrected using the high frequency response ($>10\,\mathrm{kHz}$).[204] Gas products were sampled from the gas and electrolyte side of the cell and quantified using gas chromatography (Trace1310, ThermoFisher) employing two thermal conductivity detectors (TCD) in a two column setup with

[2] The electrodes were produced by B. Ellendorff, Institute of Chemical and Electrochemical Process Engineering, TU Clausthal

[3] Experimental investigations were conducted during a research stay at Clausthal University of Technology and in collaboration with J. Osiewacz, Institute of Chemical and Electrochemical Process Engineering, TU Clausthal

a Haysep Q column and a 5 Å mole sieve with a temperature ramp from 50 to 120 °C within 9 min. For FE_{CO}-current density curves, the last GC injection sample of each current step was evaluated.

5.3 Macrokinetic modeling approach for GDE

I developed a 1D-model to simulate the reaction and transport processes and states in the electrodes including the electrolyte distribution for different operating conditions and designs of GDEs (Figure 5.1). The kinetic description for the surface reactions and carbonation, as well as diffusion coefficients and gas/liquid phase transition properties of the electrolyte were taken from the previous model of CO_2R at a silver rotating disc electrode.[134] These were integrated into a GDE model, which was inspired by a GDE model for a cathode involved in oxygen reduction reaction.[154]
To reduce model complexity while retaining the essential physics, the following assumptions were applied:

- Migration and diffusion, and Stefan flow in the gas phase are considered as the main transport processes; capillary forces or gravity effects are neglected.
- Electrochemical reactions are assumed to take place in the flooded agglomerate, and carbonation reactions in the flooded agglomerate and the liquid diffusion layer.
- The model is one-dimensional; considering concentration and state changes only perpendicular to the electrode surface, i.e., transport occurs only through-plane.
- Temperature and electrode properties are uniform and constant.

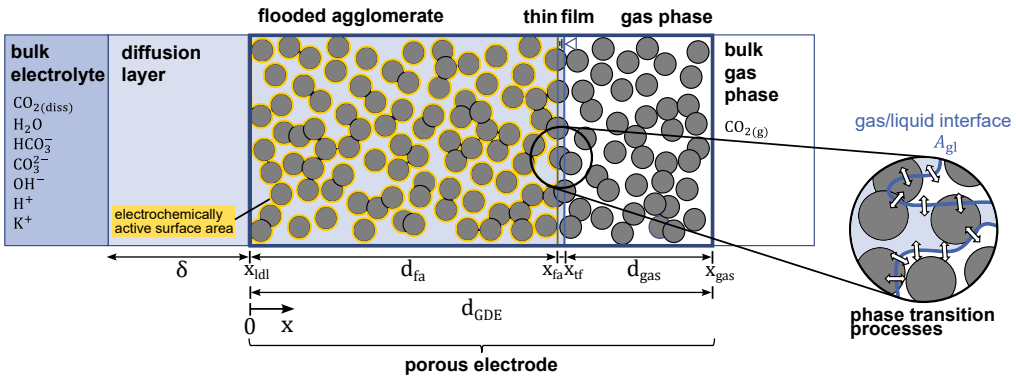

Figure 5.1: Scheme of gas diffusion electrode model for CO_2 reduction.

- The intrusion state and gas-liquid interface position are assumed constant over time and independent of the applied current density.
- Precipitation of salt is neglected.

5.3.1 Model description

The GDE is partly flooded by electrolyte. It contains a porous Ag structure that facilitates the reaction and transport of dissolved and gaseous reactants and products. It provides a two-phase boundary between electrolyte and catalyst, which is the ECSA. The at least partially flooded area is called flooded agglomerate (fa) in the following. It is the area where the electrochemical reactions take place. These are the electrochemical CO_2 reduction into CO and hydrogen evolution reaction, which I model using the same lumped microkinetic mechanisms as in the planar electrode model (Eq. 3.1-3.4) and electrochemical reaction rates are calculated by a Butler-Volmer-type kinetic equation (Eq. 5.1-5.4) analogue to planar electrode model.
The electrolyte is transported to the GDE through a liquid diffusion layer (ldl) adjacent to the GDL (Eq. 5.14-5.16). Everywhere in the electrolyte phase, alkaline carbonation reactions were considered as in the planar model using the concentration-dependent power law (Eq. 5.10-5.13).

Table 5.1: Electrode parameters and the respective identified parameters of electrolyte intrusion and electrochemically active surface area for electrodes with different PTFE content, number of spray-coated layers and pressure differences between gas and electrolyte side: electrode thickness d_{GDE} (determined with a thickness dial gauge by averaging between six measuring points), Ag catalyst loading, porosity ε, thickness of flooded agglomerate d_{fa}, flooding degree, specific surface area of the gas/liquid interface S_{gl}, volumetric surface area of Ag catalyst a_{cat}, electrochemically active surface area ECSA, and thickness of the electrolyte layer between gas and catalyst L.

	d_{GDE} [a/] µm	Catalyst loading [a] mg cm^{-2}	ε [b/] -	d_{fa} [c/] µm	Flooding degree [d] $\frac{d_{\mathrm{fa}}}{d_{\mathrm{GDE}}} \cdot 100\%$	S_{gl} [c/] -	a_{cat} [c/] m^2 m^{-3}	ECSA$_{\mathrm{v}}$ [d/] m^2 m^{-3}	ECSA$_{\mathrm{a}}$ [d/] m^2 m^{-2}	L [d/] µm
1 wt% PTFE; 50 layers; 100 mbar	200 ± 6	70.64	0.4	192.62	96.31%	57.3	10.5×10^5	10.08×10^5	201.5	3.4
1 wt% PTFE; 80 layers; 100 mbar	275 ± 7	122.03	0.4	246.65	89.69%	50.0	9.09×10^5	8.15×10^5	224.2	5.0
1 wt% PTFE; 110 layers; 100 mbar	390 ± 7	189.64	0.4	289.37	74.20%	60.0	9.04×10^5	6.71×10^5	261.6	4.8
3 wt% PTFE; 80 layers; 20 mbar	391 ± 10	183.41	0.355	247.61	63.17%	18.8	3.13×10^5	1.98×10^5	77.5	13.2
3 wt%; 80 layers; 60 mbar	350 ± 5	165.86	0.355	277.03	70.67%	18.3	4.14×10^5	2.92×10^5	114.6	15.1
3 wt%; 80 layers; 100 mbar	323 ± 10	149.30	0.355	317.44	98.28%	38.4	5.27×10^5	5.18×10^5	167.3	8.3
2 wt%; 80 layers; 100 mbar	200 ± 6	130.38	0.37	222.96	71.69%	30.9	9.07×10^5	10.08×10^5	202.4	7.2

[a] measured, [b] prior work, [c] model parametrization to experiments, [d] calculated from other parameters.

Table 5.2: Model equations for GDE model

Electrochemical reaction kinetics and charge balance		
Reaction rate for first step of electrochemical CO_2 reduction into CO	$r_{\mathrm{CO_2R,1}} = k_{\mathrm{f,CO_2R,1}} \cdot \exp\left(\frac{-(1-\alpha_{\mathrm{CO_2R}})\mathrm{F}}{\mathrm{R}T}\eta_{\mathrm{CO_2R}}\right) \cdot a_{\mathrm{cat}} \cdot a_{\mathrm{CO_2}} \cdot \theta_{[\,]}$ $- k_{\mathrm{b,CO_2R,1}} \cdot \exp\left(\frac{\alpha_{\mathrm{CO_2R}}\mathrm{F}}{\mathrm{R}T}\eta_{\mathrm{CO_2R}}\right) \cdot a_{\mathrm{cat}} \cdot \theta_{\mathrm{CO_2^{-\bullet}}}$	(5.1)
Reaction rate for second step of electrochemical CO_2 reduction into CO	$r_{\mathrm{CO_2R,2}} = k_{\mathrm{f,CO_2R,2}} \cdot \exp\left(\frac{-(1-\alpha_{\mathrm{CO_2R}})\mathrm{F}}{\mathrm{R}T}\eta_{\mathrm{CO_2R}}\right) \cdot a_{\mathrm{cat}} \cdot \theta_{\mathrm{CO_2^{-\bullet}}}$ $- k_{\mathrm{b,CO_2R,2}} \cdot \exp\left(\frac{\alpha_{\mathrm{CO_2R}}\mathrm{F}}{\mathrm{R}T}\eta_{\mathrm{CO_2R}}\right) \cdot a_{\mathrm{cat}} \cdot \theta_{[\,]} \cdot a_{\mathrm{CO}} \cdot a_{\mathrm{OH^-}}^2$	(5.2)
Reaction rate for Volmer step of HER	$r_{\mathrm{HER,1}} = k_{\mathrm{f,HER,1}} \cdot \exp\left(\frac{-(1-\alpha_{\mathrm{HER}})\mathrm{F}}{\mathrm{R}T}\eta_{\mathrm{HER}}\right) \cdot a_{\mathrm{cat}} \cdot \theta_{[\,]}$ $- k_{\mathrm{b,HER,1}} \cdot \exp\left(\frac{\alpha_{\mathrm{HER}}\mathrm{F}}{\mathrm{R}T}\eta_{\mathrm{HER}}\right) \cdot a_{\mathrm{cat}} \cdot \theta_{\mathrm{H^\bullet}} \cdot a_{\mathrm{OH^-}}$	(5.3)
Reaction rate for Heyrovsky step of HER	$r_{\mathrm{HER,2}} = k_{\mathrm{f,HER,2}} \cdot \exp\left(\frac{-(1-\alpha_{\mathrm{HER}})\mathrm{F}}{\mathrm{R}T}\eta_{\mathrm{HER}}\right) \cdot a_{\mathrm{cat}} \cdot \theta_{\mathrm{H^\bullet}}$ $- k_{\mathrm{b,HER,2}} \cdot \exp\left(\frac{\alpha_{\mathrm{HER}}\mathrm{F}}{\mathrm{R}T}\eta_{\mathrm{HER}}\right) \cdot a_{\mathrm{cat}} \cdot a_{\mathrm{H_2}} \cdot a_{\mathrm{OH^-}} \cdot \theta_{[\,]}$	(5.4)
Charge balance	$\frac{\mathrm{d}E}{\mathrm{d}t} = \frac{1}{C_{\mathrm{DL}}^{\mathrm{flat}} \cdot d_{\mathrm{fa}} \cdot a_{\mathrm{cat}}}\left(j - \mathrm{F}\sum_j r_j\right)$	(5.5)
Nernst equation to calculate overpotential for reaction j	$\eta_j = E - \left(E_j^{00} - \frac{2.303\mathrm{R}T}{\mathrm{F}} \cdot \mathrm{pH}\right)$	(5.6)
Faradaic current density	$j_{\mathrm{F,CO}} = \mathrm{F} \cdot (r_{\mathrm{CO_2R,1}} + r_{\mathrm{CO_2R,2}})$	(5.7)
	$j_{\mathrm{F,H_2}} = \mathrm{F} \cdot (r_{\mathrm{HER,1}} + r_{\mathrm{HER,2}})$	(5.8)
Faradaic efficiency of carbon monoxide	$\mathrm{FE_{CO}} = \frac{j_{\mathrm{F,CO}}}{j_{\mathrm{F,CO}} + j_{\mathrm{F,H_2}}}$	(5.9)
Chemical carbonation reaction kinetics		
Reaction rates	$r_{\mathrm{w}} = k_{\mathrm{f,w}} - k_{\mathrm{b,w}} \cdot c_{\mathrm{H^+}} \cdot c_{\mathrm{OH^-}}$	(5.10)
	$r_{\mathrm{c1}} = k_{\mathrm{f,c1}} \cdot c_{\mathrm{CO_2}} \cdot c_{\mathrm{OH^-}} - k_{\mathrm{b,c1}} \cdot c_{\mathrm{HCO_3^-}}$	(5.11)
	$r_{\mathrm{c2}} = k_{\mathrm{f,c2}} \cdot c_{\mathrm{HCO_3^-}} \cdot c_{\mathrm{OH^-}} - k_{\mathrm{b,c2}} \cdot c_{\mathrm{CO_3^{2-}}}$	(5.12)
Equilibrium constant	$K_j = \frac{k_{\mathrm{f},j}}{k_{\mathrm{b},j}}$	(5.13)
Mass balance, species and charge transport		
Liquid diffusion layer:		
Molar transport flux of species i	$N_j = -D_i^{\mathrm{liq}}\nabla c_i - z_i\frac{D_i^{\mathrm{liq}}}{\mathrm{R}T}\mathrm{F}c_i\nabla\phi$	(5.14)
Balance of species i with transport and a source by chemical reactions L	$\frac{\partial c_i}{\partial t} = -\nabla N_i + \sum_{j=1}^{L}\nu_{i,j}r_j$	(5.15)
Ionic charge transport	$j(x) = \mathrm{F}\sum_i z_i\left(-D_i^{\mathrm{liq}}\nabla c_i - z_i\frac{D_i^{\mathrm{liq}}}{\mathrm{R}T}Fc_i\nabla\phi\right)$ with $\nabla j = 0$	(5.16)

Flooded agglomerate:		
Molar transport flux of species i	$N_i = -D_i^{\text{liq}}\varepsilon^{1.5}\nabla c_i S_{\text{int}} - z_i\frac{D_i^{\text{liq}}\varepsilon^{1.5}}{\mathrm{R}T}\mathrm{F}c_i\nabla\phi S_{\text{int}}$ with $S_{\text{int}} = \begin{cases} S_{\text{gl}}, & \text{if } i \in \{\mathrm{CO_2}, \mathrm{H_2}, \mathrm{CO}\}, \\ 1, & \text{otherwise.} \end{cases}$	(5.17)
Balance of species i with transport and sources by electrochemical reactions K and chemical reactions L	$\varepsilon\frac{\partial c_i}{\partial t} = -\nabla N_i + \sum_{j=1}^{K}\frac{\nu_{i,j}r_j}{\Delta x} + \sum_{i=1}^{L}\nu_{i,j}r_j$	(5.18)
Balance of adsorbed species with $k = \{[\,]; \mathrm{CO_2}^{\bullet-}; \mathrm{H}^{\bullet}\}$	$\frac{\partial\theta_k}{\partial t} = \frac{1}{\Gamma^{\text{flat}}\cdot a_{\text{cat}}}\sum_j\frac{\nu_{k,j}r_j}{\Delta x}$	(5.19)
Ionic charge transport	$j(x) = \mathrm{F}\sum_i z_i\left(-D_i^{\text{liq}}\varepsilon^{1.5}\nabla c_i - z_i\frac{D_i^{\text{liq}}\varepsilon^{1.5}}{\mathrm{R}T}Fc_i\nabla\phi\right)$	(5.20)
Liquid thin-film:		
Molar transport flux of species i	$N_i = -D_i^{\text{liq}}\nabla c_i S_{\text{gl}}$	(5.21)
Balance of species i	$\frac{\partial c_i}{\partial t} = -\nabla N_i$	(5.22)
Gas phase:		
Molar transport flux of species j	$N_i = -D_{i,\mathrm{CO_2}}^{\text{gas}}\varepsilon^{1.5}\nabla\frac{p_i j}{\mathrm{R}T} + \frac{p_i}{\mathrm{R}T}v_{\text{gas}}$	(5.23)
Balance of species i	$\varepsilon\frac{\partial p_i}{\partial t} = -\nabla N_i$	(5.24)
Sum of molar flux due to phase transition from liquid to gas or vice versa	$\sum_j N_j^{\text{gl}} = N_{\mathrm{H_2O}}^{\text{evap}} + N_{\mathrm{CO}}^{\text{gl}} + N_{\mathrm{H_2}}^{\text{gl}} - N_{\mathrm{CO_2}}^{\text{sol}}$	(5.25)
Convective velocity of liquid phase (Stefan flow)	$v_{\text{gas}} = \frac{\sum_i N_i^{\text{gl}}\mathrm{R}T}{p_{\text{tot}}}$ with $\frac{\mathrm{d}v_{\text{gas}}}{\mathrm{d}x} = 0$	(5.26)
Phase transition		
Gas/liquid equilibrium CO_2 (Henry's law)	$p_{\mathrm{CO_2}}^* = H_{\mathrm{CO_2}}\cdot c_{\mathrm{CO_2}}^*$	(5.27)
Gas/liquid equilibrium H_2O (Raoult's law)	$p_{\mathrm{H_2O}}^* = x_{\mathrm{H_2O}}\cdot p_{\mathrm{H_2O}}^{\text{sat}}$	(5.28)
Ideal gas law with $i = \{\mathrm{H_2}; \mathrm{CO}\}$	$p_i^* = c_i^*\mathrm{R}T$	(5.29)
Boundary conditions		
$KHCO_3$ in electrolyte bulk	$c_{\mathrm{KHCO_3}}(x = -\delta, t) = c_{\mathrm{KHCO_3,bulk}} = \text{const.}$	(5.30)
CO_2 in gas phase bulk	$p_{\mathrm{CO_2}}(x = x_{\text{gas}}, t) = p_{\text{tot}} = \text{const.}$	(5.31)
Partial pressure of species i in gas bulk with $i = \{\mathrm{CO_2}; \mathrm{H_2}; \mathrm{H_2O}\}$	$p_i^* = c_i^*\mathrm{R}T$	(5.32)
Correction of internal resistance	$E = E_{\text{ext}} - j_{\text{ext}}A_{\text{geom}}R_{\text{int}}$	(5.33)

On the opposing side of the electrode, CO_2 gas is introduced into the GDE. The gas/liquid interface in the electrode is delineated by a liquid thin film (tf). In this thin film, only species transport takes place (Eqs. 5.21 and 5.22). At the gas/liquid interface, phase transition phenomena occur, i.e.,

dissolution of gaseous CO_2 into the liquid phase described by Henry's law (Eq. 5.27), evaporation of water into the gas phase described by Raoult's law (Eq. 5.28), and complete outgassing of dissolved CO and H_2 is assumed at the gas/liquid interface due to low solubility of these gases (Eq. 5.29).

Flooding of single pores leads to an increase in the gas/liquid interface A_{gl} compared to the geometrical area of the electrode A_{geom}, and thus to an increase in gas/liquid phase transition. The increase in area is accounted for in the model by introducing the parameter S_{gl}, the ratio of the specific surface area of the interface per geometrical electrode area (details see Röhe et al.[154]):

$$S_{\mathrm{gl}} = \frac{A_{\mathrm{gl}}}{A_{\mathrm{geom}}} \tag{5.34}$$

This approach corresponds to a homogenization of heterogeneous electrolyte intrusion and, in a simple manner, allows us to identify changes in the gas/liquid interphase from experiments and assess the effect of electrolyte intrusion behavior on the polarization curve and Faradaic efficiency. As different morphologies, compositions, and operating conditions lead to different intrusion patterns, this parameter needs to be adjusted for each electrode (for more details, see section 5.3.2) and operating parameter set individually to reproduce the measurements.

Kinetic and intrusion-specific model parameters are listed in Table 5.1 and Table 5.3. Species transport in the gaseous phase is described by Fickian diffusion and convective Stefan flow (Eq. 5.23) and in the liquid phase by the Nernst-Planck equation with Fickian diffusion and ion migration (Eqs. 5.14, 5.17, and 5.21). The binary diffusion coefficients for the gaseous phase were calculated with the Chapman-Enskog method (details are shown in SI). In the porous electrode, effective diffusion coefficients of the species are calculated by considering the porosity of the electrode ε and the Bruggemann correlation for tortuosity τ (Eqs. 5.17 and 5.23):

$$\tau = \varepsilon^{-0.5} \tag{5.35}$$

Table 5.3: Material, design, and kinetic parameters that were kept constant for all simulations.

Parameter	Symbol	Value	Unit	Source
Operating conditions				
Concentration of electrolyte	c_{elyt}	1	$\mathrm{mol\,L^{-1}}$	-
Pressure of electrolyte side	p_{liq}	1	atm	-
Pressure of gas side	p_{tot}	$p_{\mathrm{liq}} + \Delta p$	atm	-
Temperature	T	298.15	K	-
Geometrical surface area of electrode	A_{geom}	10	$\mathrm{cm^2}$	-
Internal ohmic resistance	R_{int}	1	Ω	a
Liquid diffusion layer thickness	δ	50×10^{-6}	m	b
Electrochemical surface reaction				
Reaction rate constant of forward reaction for first step of electrochemical CO_2 reduction into CO	$k_{0,\mathrm{f},CO_2\mathrm{R},1}$	5.325×10^{-8}	$\mathrm{mol\,m^{-2}\,s^{-1}}$	b

Reaction rate constant of forward reaction for second step of electrochemical CO_2 reduction into CO	$k_{0,\mathrm{f},\mathrm{CO_2R},2}$	2.465×10^{-4}	$\mathrm{mol\,m^{-2}\,s^{-1}}$	b
Reaction rate constant of forward reaction for Volmer step of HER	$k_{0,\mathrm{f},\mathrm{HER},1}$	1.497×10^{-8}	$\mathrm{mol\,m^{-2}\,s^{-1}}$	b
Reaction rate constant of forward reaction for Heyrovsky step of HER	$k_{0,\mathrm{f},\mathrm{HER},2}$	6.937×10^{-5}	$\mathrm{mol\,m^{-2}\,s^{-1}}$	b
Reaction rate constant of backward reaction for first step of electrochemical CO_2 reduction into CO	$k_{0,\mathrm{b},\mathrm{CO_2R},1}$	2.566×10^{-23}	$\mathrm{mol\,m^{-2}\,s^{-1}}$	b
Reaction rate constant of backward reaction for second step of electrochemical CO_2 reduction into CO	$k_{0,\mathrm{b},\mathrm{CO_2R},2}$	1.079×10^{-25}	$\mathrm{mol\,m^{-2}\,s^{-1}}$	b
Reaction rate constant of backward reaction for Volmer step of HER	$k_{0,\mathrm{b},\mathrm{HER},1}$	6.582×10^{-21}	$\mathrm{mol\,m^{-2}\,s^{-1}}$	b
Reaction rate constant of backward reaction for Heyrovsky step of HER	$k_{0,\mathrm{b},\mathrm{HER},2}$	2.776×10^{-25}	$\mathrm{mol\,m^{-2}\,s^{-1}}$	b
Charge transfer coefficient for CO_2 reduction	$\alpha_{\mathrm{CO_2R}}$	0.50	-	b
Charge transfer coefficient for hydrogen evolution reaction	α_{HER}	0.76	-	b
Standard redox potential of CO_2R	$E^{00}_{\mathrm{CO_2R}}$	-0.11	V	[117]
Standard redox potential of HER	E^{00}_{HER}	0	V	[117]
Specific capacitance of electrical double layer for flat surface	$C^{\mathrm{flat}}_{\mathrm{DL}}$	0.5	$\mathrm{F\,m^{-2}}$	a
Concentration of surface adsorption sites for flat surface	Γ^{flat}	$7.04 \cdot 10^{-6}$	$\mathrm{mol\,m^{-2}}$	[117]
Electrolyte conditions				
Activity coefficient of dissolved species j	γ_j	1	-	c
Standard concentration of dissolved species j	$c_j^{\ominus}$	1	$\mathrm{kmol\,m^{-3}}$	-
Reaction rate constant for forward reaction of water dissociation	$k_{\mathrm{f,w}}$	2.4×10^{-2}	$\mathrm{mol\,m^{-3}\,s^{-1}}$	[66]
Equilibrium constant for water dissociation	K_{w}	1×10^{-8}	$\mathrm{mol^2\,m^{-6}}$	[65]
Reaction rate constant of chemical CO_2-to-bicarbonate reaction	$k_{\mathrm{f,c1}}$	5.93	$\mathrm{m^3\,mol^{-1}\,s^{-1}}$	[66]
Equilibrium constant of chemical CO_2-to-bicarbonate reaction	K_{c1}	4.44×10^4	$\mathrm{m^3\,mol^{-1}}$	[65]
Reaction rate constant of chemical bicarbonate-to-carbonate reaction	$k_{\mathrm{f,c2}}$	1×10^5	$\mathrm{m^3\,mol^{-1}\,s^{-1}}$	[65]
Equilibrium constant for chemical bicarbonate-to-carbonate reaction	K_{c2}	4.66	$\mathrm{m^3\,mol^{-1}}$	[65]
Transport parameters				
Binary diffusion coefficient of dissolved CO_2 in water	$D^{\mathrm{liq}}_{\mathrm{CO_2,H_2O}}$	1.91×10^{-9}	$\mathrm{m^2\,s^{-1}}$	[165]
Self diffusion coefficient of liquid H_2O	$D^{\mathrm{liq}}_{\mathrm{H_2O}}$	2.57×10^{-9}	$\mathrm{m^2\,s^{-1}}$	[166]
Binary diffusion coefficient of dissolved CO in water	$D^{\mathrm{liq}}_{\mathrm{CO,H_2O}}$	1.99×10^{-9}	$\mathrm{m^2\,s^{-1}}$	[205]
Binary diffusion coefficient of H_2 in water	$D^{\mathrm{liq}}_{\mathrm{H_2,H_2O}}$	2.28×10^{-9}	$\mathrm{m^2\,s^{-1}}$	[205]
Binary diffusion coefficient of OH^- in water	$D^{\mathrm{liq}}_{\mathrm{OH^-,H_2O}}$	5.27×10^{-9}	$\mathrm{m^2\,s^{-1}}$	[167]
Binary diffusion coefficient of H^+ in water	$D^{\mathrm{liq}}_{\mathrm{H^+,H_2O}}$	9.31×10^{-9}	$\mathrm{m^2\,s^{-1}}$	[167]
Binary diffusion coefficient of HCO_3^- in water	$D^{\mathrm{liq}}_{\mathrm{HCO_3^-,H_2O}}$	1.19×10^{-9}	$\mathrm{m^2\,s^{-1}}$	[167]
Binary diffusion coefficient of CO_3^{2-} in water	$D^{\mathrm{liq}}_{\mathrm{CO_3^{2-},H_2O}}$	0.92×10^{-9}	$\mathrm{m^2\,s^{-1}}$	[167]
Binary diffusion coefficient of K^+ in water	$D^{\mathrm{liq}}_{\mathrm{K^+,H_2O}}$	1.96×10^{-9}	$\mathrm{m^2\,s^{-1}}$	[167]

[a] measured, [b] model parametrization to experiments, [c] assumption.

The mobility of dissolved species is approximated by the Nernst-Einstein equation (Eq. 2.10).

5.3.2 Numerical simulation and parametrization

The model was implemented in MATLAB R2022b, and differential equations were solved with the ode15s solver. Spatial, one-dimensional discretization from liquid to gas phase (coordinate x in Figure 5.1) was done with an equidistant grid with a grid size of $\Delta x = 1\,\mu\mathrm{m}$. Lower grid sizes do not lead to a visual change of simulated polarization and Faradaic efficiency-current density curves. For spatial discretization, the finite volume method with central differential quotient was implemented. Boundary conditions for the simulations can be found in Table 5.2, Eqs. 5.30-5.33. For parameter identification, the MATLAB-implemented optimizer patternsearch was used. The kinetic parameters of CO_2R and HER including reaction rate constants of forward and backward reactions and charge transfer coefficients $\alpha_{\mathrm{CO_2R}}$ and α_{HER} were identified by using the polarization curve and FE_{CO}-current density curve for the reference case $98\,\mathrm{wt}\%$ Ag, 80 layers, and 100 mbar. Additionally, the thickness of the liquid diffusion layer δ was identified in this optimization step. These parameters were held constant for all simulated electrode and operation parameter variations.
For identifying flooding state and electrode parameters for the different operating conditions and designs, the thickness of the flooded agglomerate d_{fa}, the specific surface area of the gas/liquid interface S_{gl}, and the intrinsic, volume specific catalyst surface of the electrode a_{cat} were identified by reproducing the polarization curve and Faradaic efficiency-current density curve of the individual measurements by simulation. Identified parameters can be found in Table 5.1. Further model, design, and operating parameters, which were kept constant for all simulations, can be found in Table 5.3.

5.4 Results and discussion

The following analysis of the impact of flooding behavior on electrode performance employs a combined approach of experimental and simulation methods. For the experiments, I varied the differential pressure between the electrolyte and gas side of the GDE, the electrode thickness, and the mass content of PTFE in the GDE. The GDEs were operated in a flow cell setup in a three-electrode configuration with aqueous 1 M $KHCO_3$ as an electrolyte (cf. section 4.2 and Table 2). Performance assessment was based on polarization curves and FE_{CO}, recorded with current densities in the range of $10\,\mathrm{mA\,cm^{-2}}$ to $200\,\mathrm{mA\,cm^{-2}}$, a range in which stable operation of the GDEs can be ensured. A 1D physicochemical model for CO_2R in Ag-GDEs (cf. section 5 and Figure 5.1) was used to identify changes in electrolyte intrusion for the different electrodes

and operating conditions and their impact on local concentration and current distribution as well as on electrode performance. Transport and reaction parameters of the model were parametrized based on experimental polarization curves and Faradaic efficiency-current density relationships obtained for the individual parameter sets (cf. section 5.3.2).

5.4.1 Current and concentration distribution along the GDE

First, I reveal the effects of concentration profiles and current distribution along the electrode thickness on the electrode potential and Faradaic efficiency for different current densities. The analysis was conducted at the example of a Ag-GDE with a thickness of $392\,\mu\mathrm{m}$ (equivalent to 80 layers of spray coating, cf. section 4.1), a PTFE mass fraction of $3\,\mathrm{wt}\%$, and an overpressure of $60\,\mathrm{mbar}$ from the gas side to the electrolyte side. The catalyst loading was $166\,\mathrm{mg\,cm^{-2}}$. The experimental polarization curve (Figure 5.2A) reveals a monotonic logarithmic decrease in potential with increasing current density, with no apparent limiting current observed within the investigated range. FE_{CO} reaches a peak of $70\,\%$ at a low current density of $20\,\mathrm{mA\,cm^{-2}}$ and decreases subsequently monotonically as current density increases (Figure 5.2B). The simulation accurately reproduces both the current-potential and FE_{CO}-current density trends.
The peak in FE_{CO} can be attributed to the kinetic interplay between CO_2R and HER: At high potentials close to open circuit potential, i.e., at low current densities, HER significantly competes with CO_2R due to its more positive onset potential, reducing FE_{CO} (Figure A.11). As current density increases, CO_2R becomes the dominant process, resulting in an upsurge in FE_{CO}. A similar observation is made in kinetic studies conducted on planar silver electrodes.[43, 163]

Already, at a current density of $25\,\mathrm{mA\,cm^{-2}}$, where FE_{CO} reaches its maximum in the simulation, a nonuniform current (Figure 5.3A) and concentration distribution (Figure 5.3C, dashed lines) are present along the flooded agglomerate. Close to the liquid diffusion layer ($x = 0$), there is a

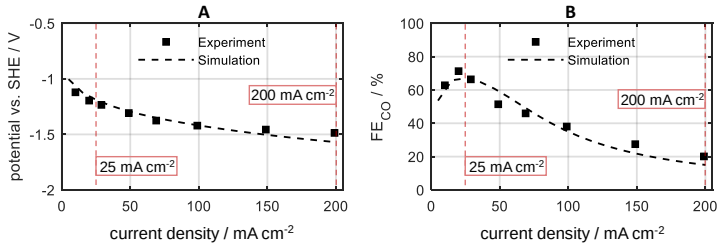

Figure 5.2: Experimental and simulated (A) polarization curves and (B) Faradaic efficiency of carbon monoxide (FE_{CO}) for a GDE with $392\,\mu\mathrm{m}$ electrode thickness, $3\,\mathrm{wt}\%$ PTFE, and a differential pressure of $60\,\mathrm{mbar}$ between gas and electrolyte side. Two current densities are highlighted. Measurements were done in a flow cell with 1 M $KHCO_3$, and potentials are iR-corrected.

slight increase in Faradaic current for CO due to an elevated CO_2 concentration at this boundary provided by the equilibrium concentration of CO_2 in 1 M $KHCO_3$ electrolyte. In proximity to the gas/liquid interface ($x = d_{fa}$), the highest CO_2 concentration is present, resulting in the highest FE_{CO} at this interface compared to the rest of the electrode. The high CO_2 concentration also lowers the pH in this area. Thus, the lowest local currents and Faradaic efficiency are found in the middle of the electrode.

The situation inside the flooded part of the electrode changes dramatically for higher current densities: FE_{CO} decreases for higher current densities and is almost zero over a large part of the flooded agglomerate at a current density of $200\,\mathrm{mA\,cm^{-2}}$ (Figure 5.3B). Thus, a significant part of the flooded GDE is not active for CO_2R. This decline can be attributed to the increasing CO_2 depletion within the electrode, evident in low local CO_2 concentrations in most of the electrode (Figure 5.3C). At this current density, almost all incoming CO_2 is directly reduced adjacent to the gas/liquid interface, and a huge part of the wetted catalyst surface lacks CO_2. This phenomenon is mainly induced by a thick electrolyte layer between the gas and the catalyst surface within the

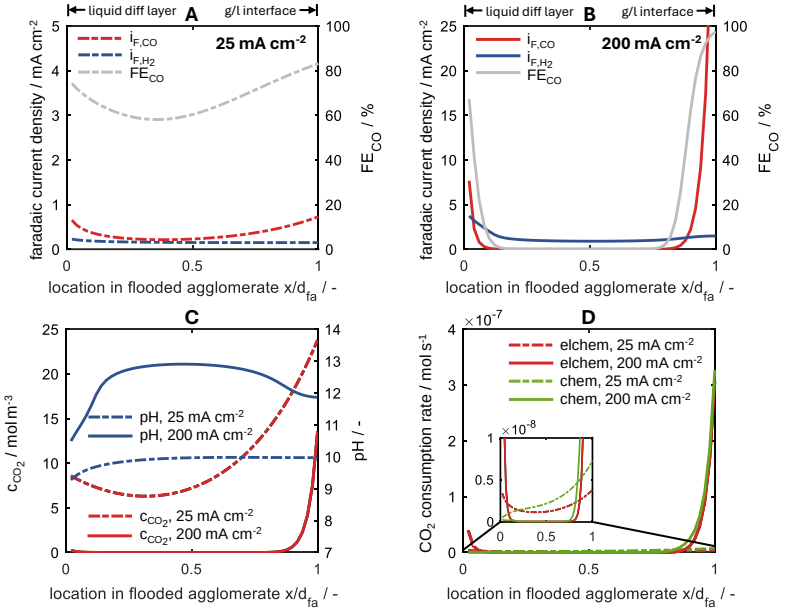

Figure 5.3: Simulated local profiles of Faradaic current densities for CO and H_2 production, respectively, and FE_{CO} along the flooded agglomerate (fa; boundary to liquid diffusion layer at $x = 0$, gas at $x = 1$) for operation at (A) $25\,\mathrm{mA\,cm^{-2}}$ and (B) $200\,\mathrm{mA\,cm^{-2}}$. (C) Local CO_2 concentration and pH along the flooded agglomerate for $25\,\mathrm{mA\,cm^{-2}}$ and $200\,\mathrm{mA\,cm^{-2}}$. (D) Chemical and electrochemical CO_2 consumption rate and carbon efficiency CE along flooded agglomerate for $25\,\mathrm{mA\,cm^{-2}}$ and $200\,\mathrm{mA\,cm^{-2}}$. GDE and operation parameters are: $350\,\mu\mathrm{m}$ thickness, $3\,\mathrm{wt\%}$ PTFE, and $60\,\mathrm{mbar}$ differential pressure in a flow cell with 1 M $KHCO_3$.

electrolyte-flooded electrode. A high value leads to long diffusion distances for dissolved CO_2 and strong transport limitations in most parts of the electrode, which in turn promotes HER.
Additionally, the local pH within the electrode increases from 10 to approximately 13 with increasing current density (Figure 5.3C). At $200\,\mathrm{mA\,cm^{-2}}$, the pH profile displays a peak located in the flooded agglomerate's center. Close to the liquid diffusion layer and the electrolyte bulk, OH^- concentration diminishes due to OH^- diffusion out of the flooded electrode and fresh electrolyte supply. Fresh electrolyte provides a high bicarbonate concentration, which promotes its reaction with OH^- to carbonate. Near the gas/liquid interface, the low pH results from a high carbonation reaction, facilitated by ample CO_2 availability. Both effects can be clearly seen in the local distribution of the chemical consumption rate of CO_2 (Figure 5.3D). At the gas/liquid interface ($x/d_{\mathrm{fa}} = 1$), electrochemical CO_2 consumption increases similarly to the chemical CO_2 consumption due to good CO_2 availability and a pronounced buffer effect by the CO_2-to-bicarbonate reaction. In contrast, at the electrolyte side ($x/d_{\mathrm{fa}} = 0$), although CO_2R increases due to higher CO_2 concentrations, chemical CO_2 consumption does not increase. The increasing pH is buffered mostly by the bicarbonate-to-carbonate reaction due to the high supply of fresh bicarbonate electrolyte.
These insights vividly illustrate that the local condition profile in the electrode determines overall electrode performance. Not only does the CO_2 supply from the gas phase affect it, but also the pH determines the distribution of CO_2R and HER. As the FE_{CO} is so sensitive to local pH and thus to local transport conditions and CO_2 availability, this motivates improving FE_{CO} by manipulating the transport and local conditions. It is thus reasonable to expect that by optimizing operating and design parameters, a low Faradaic efficiency can be significantly increased. Hence, in section 5.4.2, I will show how the operating and design variation impacts electrolyte intrusion, and how this in turn impacts local conditions and performance. This allows knowledge-driven design, i.e., to reveal ways in which the GDE properties and operational conditions can be tailored to improve the CO_2R performance and Faradaic efficiency.

5.4.2 Electrolyte intrusion behavior of the GDE

As revealed in the last section, electrolyte intrusion behavior has a crucial impact on the local state and thus on the electrode performance. To gain insight into this aspect, I conducted a comprehensive study on selected electrode and operational parameters. The varied parameters include electrode thickness, PTFE mass fraction in the electrode, and differential pressure between liquid and gas sides. Experimental polarization curves and FE-current density curves were successfully reproduced through simulations. From the simulation, I extracted parameter values for the volumetric electrochemically active surface area ($ECSA_v$, $\mathrm{m^2\,m^{-3}}$) and the apparent thickness L of the electrolyte layer between the gas and the catalyst.[124] $ECSA_v$ characterized

the catalytic activity provided by the wetted parts of the electrode. L depends on the electrolyte arrangement in the electrode, i.e., electrolyte intrusion depth d_{fa} and size of the gas/liquid interface S_{gl}, and defines at the same time the maximum transport distance of the dissolved CO_2 to the catalyst surface (Figure 5.4, more information in section A.3.2 of the Supporting Information). In the following, $\mathrm{ECSA_v}$ and L are discussed, as they proved to be the most meaningful parameters with regard to electrode behavior. These parameters were calculated using the following equations:

$$\mathrm{ECSA_v} = d_{\mathrm{fa}} \cdot a_{\mathrm{cat}} \cdot d_{\mathrm{GDE}}^{-1} \tag{5.36}$$

$$L = d_{\mathrm{fa}} \cdot S_{\mathrm{gl}}^{-1}. \tag{5.37}$$

Here, d_{GDE} represents the thickness of the electrode, d_{fa} is the thickness of the flooded agglomerate, a_{cat} is the specific surface area of the Ag catalyst per electrode volume, and S_{gl} denotes the specific surface area of the gas/liquid interface per geometrical electrode area (Eq. 5.34). d_{fa}, a_{cat}, and S_{gl} were identified by parameter optimization. The specific surface area of the Ag catalyst a_{cat} was identified in a narrow range to a value of $6.25 \times 10^5\,\mathrm{m^2\,m^{-3}}$ for a PTFE content of $3\,\mathrm{wt\%}$. A similar value was determined by Neumann et al.[206] using tomographic reconstruction of a porous electrode structure with the same PTFE content (for detailed information, see section 5.3.1).[206]

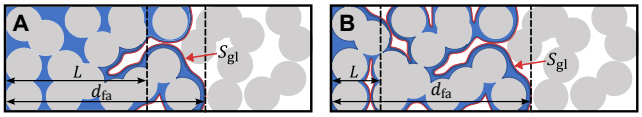

Figure 5.4: Illustration of possible electrolyte arrangement in porous GDE with (A) low gas/liquid interface S_{gl} resulting in a larger, apparent thickness L of electrolyte layer between the gas and the catalyst surface and with (B) high S_{gl} resulting in low values of L.

5.4.2.1 Influence of electrode thickness

To investigate the impact of electrode thickness, I adjusted the GDE thickness by varying the number of layers between 50 and 110 during the spray coating process of electrode preparation. The resulting electrode thickness was measured after sintering. The examined electrodes had thicknesses of $200\,\mu\mathrm{m}$, $275\,\mu\mathrm{m}$, and $390\,\mu\mathrm{m}$. The differential pressure and PTFE content were kept constant at $100\,\mathrm{mbar}$ and $1\,\mathrm{wt\%}$ PTFE, respectively. The corresponding current density-potential and $\mathrm{FE_{CO}}$-current density curves are presented in Figure 5.5A and B.

At low current densities, the thicker electrodes exhibit slightly more positive electrode potentials, indicating better performance. However, at higher current densities, potentials are nearly identical for all thicknesses. $\mathrm{FE_{CO}}$ values are quite similar but slightly higher for thicker electrodes

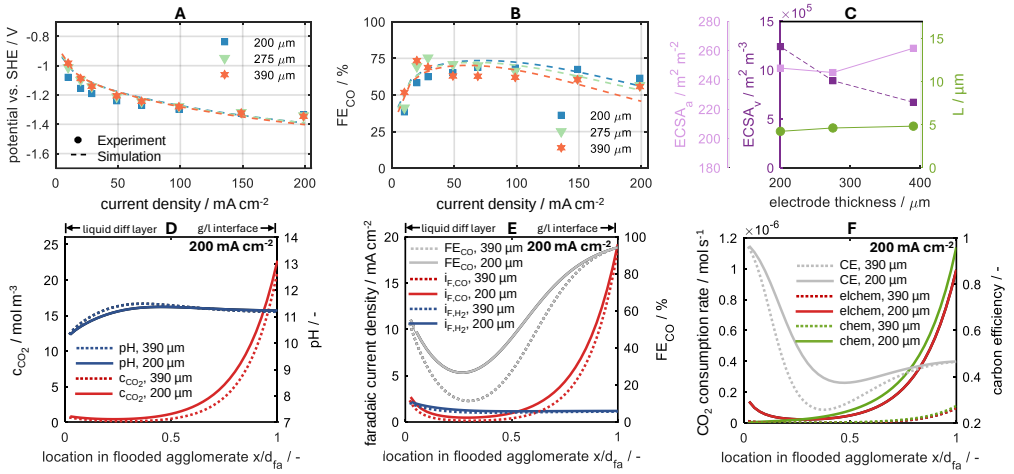

Figure 5.5: Impact of electrode thickness on GDE performance and state: Experimental and simulated (A) polarization curves and (B) FE_{CO} (differential pressure: 100 mbar, PTFE content: 1 wt%). (C) Identified volumetric and surface-specific electrochemically active surface area ($ECSA_v$ and $ECSA_a = d_{fa}a_{cat}$) and apparent thickness L of liquid electrolyte layer between catalyst and gas phase in flooded agglomerate as a function of the electrode thickness. (D) Local CO_2 concentration and pH as well as (E) local profiles of Faradaic current densities and FE_{CO}, and (F) absolute chemical and electrochemical CO_2 consumption rate and the carbon efficiency CE along flooded agglomerate for 200 µm (solid lines) and 390 µm electrode thickness (dashed lines) at 200 $mA\,cm^{-2}$. Measurements were done in a flow cell with 1 M $KHCO_3$, and potentials are iR-corrected.

at low current densities ($<50\,mA\,cm^{-2}$) and lower at higher current densities. Consequently, thinner electrodes seem to be slightly more selective for CO_2 reduction compared to HER in the technically relevant current density regime ($>150\,mA\,cm^{-2}$). However, the performance is relatively robust against variations in electrode thickness under the given operating conditions. It can be further concluded that there is no simple relation between a change in thickness and improvement across the total current range regarding both performance measures, i.e., electrode potential and FE_{CO}. This again suggests a complex interplay of parameters and processes with changes in limiting processes, which I analyzed in the following.

The model reproduced the trend, both for the polarization curve and FE_{CO}. The corresponding simulation results suggest that for thick electrodes, smaller potential losses at low currents ($<50\,mA\,cm^{-2}$) can be attributed to their larger area-specific electrochemically active surface area ($ECSA_a$), provided by the larger amount of wetted catalyst material compared to thinner electrodes (Figure 5.5C).

The slightly increased FE_{CO} for thinner electrodes at high current densities can be explained as follows: Firstly, the CO_2 concentration in the electrode is higher for a thinner electrode thickness (Figure 5.5D) as the molecules are spread over a smaller volume. This results in an increase of FE_{CO} in the whole electrode for thinner electrodes (Figure 5.5E). Secondly, the local pH is shifted

to slightly lower values for thinner electrodes, which can be explained by the shorter distance of transport for dissolved species to and from the electrolyte bulk. This distance depends on electrolyte intrusion, characterized by the length of the flooded agglomerate (d_{fa}). Thinner electrodes experience significantly smaller d_{fa}, leading to enhanced electrolyte transport, i.e., a better removal of hydroxide ions and an improved supply of bicarbonate and carbonate species. This, in turn, results in a stronger buffering effect by the bicarbonate-to-carbonate reaction and a lower pH. The shift to the bicarbonate-to-carbonate reaction is reflected in a higher carbon efficiency within the flooded agglomerate with a mean value of $52\,\%$ compared to $43\,\%$ at $200\,\mathrm{mA\,cm^{-2}}$ for the thick electrode (Figure 5.5F and Eq. 2.52).
The effect of slow electrolyte transport in the porous Ag electrode structure was also observed in oxygen depolarized cathodes.[155] My observation of improved performance with better transport of dissolved electrolyte species aligns with Kong et al.[196], who reported enhanced electrode performance when fresh electrolyte was introduced through cracks.[196]
Consequently, the performance of CO_2-consuming GDEs is not only limited by CO_2 transport itself, but also by slow electrolyte transport in and out of the electrode, which diminishes FE_{CO} and carbon efficiency for thick electrodes. This explains the downside of carbon-free silver electrodes, which typically have relatively high electrode thicknesses and thus suffer more from slow CO_2 and electrolyte transport.

5.4.2.2 Influence of differential pressure

One of the most critical operating parameters for gas diffusion electrodes is the differential pressure between the gas and the electrolyte side. Maintaining an overpressure from the gas side is essential to prevent complete flooding of the electrode pores with liquid electrolyte.[101, 207] The differential pressure has a substantial influence on the intrusion of electrolyte into the electrode. In this section, I delve into the detailed effects of differential pressure on local reaction conditions and current density distribution. I aim to draw conclusions about electrolyte distribution and the potential for performance enhancement through optimized operating conditions.
The overpressure from the gas side was varied between 20 and 100 mbar while keeping the electrode properties constant ($3\,\mathrm{wt\%}$ PTFE and 80 layers of spray coating). Due to the electrode preparation process, there are slight deviations in the electrode thickness d_{GDE} in this series of measurements (Table 5.1). Yet, they are shown to have a negligible impact compared to the effect of pressure (Figure A.12 and Figure A.13). For this reason, larger differences in performance can be attributed to the variation of the operating parameter, i.e., the differential pressure.
The experimental polarization curve in Figure 5.6A reveals a marginal improvement in potential with increasing differential pressure at all applied current densities. Using the model, the

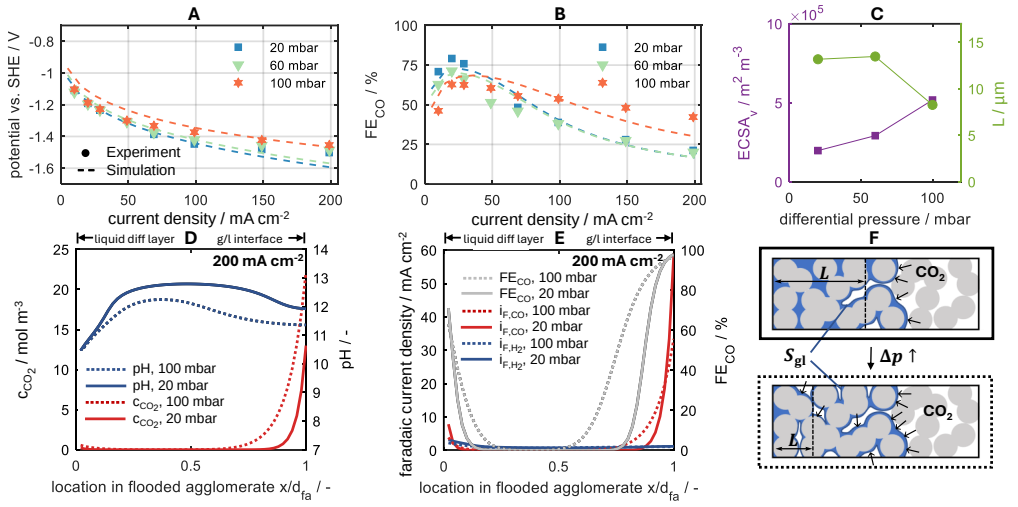

Figure 5.6: Impact of differential pressure on GDE performance and state: Experimental and simulated (A) polarization curves and (B) FE_{CO} (electrode layers: 80, i.e. electrode thickness around 350 µm, PTFE content: 3 wt%). (C) Identified volumetric electrochemically active surface area ($ECSA_v$) and apparent thickness L of liquid electrolyte layer between catalyst and gas phase in flooded agglomerate as a function of the differential pressure. (D) Local CO_2 concentration and pH as well as (E) local profiles of Faradaic current densities and FE_{CO} along flooded agglomerate for 20 mbar (solid line) and 100 mbar differential pressure (dashed line) at 200 $mA\,cm^{-2}$. (F) Illustration of the increase in the gas/liquid interface by increasing the differential pressure. Measurements were done in a flow cell with 1 M $KHCO_3$, and potentials are iR-corrected.

improvement can be attributed to an increase in ECSA (Figure 5.6C), which is caused mostly by an increase in flooded agglomerate thickness: Changing the differential pressure from 20 to 100 mbar results in a change in the flooded agglomerate thickness d_{fa} from 248 µm to 317 µm (Table 5.1). The origin of this strong increase in wetting motivates future studies in this area.

The FE_{CO} is much more sensitive to changes in differential pressure than the electrode potential, as evidenced by only a 10% improvement in potential vs. a 25% improvement in FE_{CO} when increasing pressure from 20 to 100 mbar at 200 $mA\,cm^{-2}$ (Figure 5.6B). At low current densities up to 30 $mA\,cm^{-2}$, a high differential pressure of 100 mbar yields the lowest FE_{CO}. Conversely, at higher current densities, the decline in FE_{CO} with increasing current density is less pronounced for the elevated differential pressure. Thus, the optimal differential pressure changes with the current density applied.

The simulation replicates the increase of FE_{CO} at high current densities for increasing differential pressure primarily by a larger gas/liquid interface: The interfacial area ratio S_{gl} doubles from 19 to 38 for an increase in the differential pressure from 20 to 100 mbar although the thickness of flooded agglomerate increased (Table 5.1). This, in turn, shortens the apparent thickness of the electrolyte layer between gas and catalyst L by 50%, reducing it to a value of around 8.28 µm for a differential pressure of 100 mbar (Figure 5.6C). Although the thickness of flooded agglomerate

increases, the increase in differential pressure promotes the selective flooding of pores in the electrode resulting in a more dispersed distribution of electrolyte and thus increasing the size of the gas/liquid interface (Figure 5.6F). This effect was also visible in the experiments by the occurrence of electrolyte permeation on the gas-exposed side, even at high applied differential pressures. Thus, the enlargement of S_{gl} outweighs the enlargement of d_{fa} with increasing differential pressure.

The concentration profile of CO_2 along the flooded agglomerate for high current densities shows that higher differential pressures result in a locally higher CO_2 concentration close to the gas/liquid interface (Figure 5.6D). This is, on the one hand, due to the larger gas-liquid boundary available for the CO_2 phase transition. On the other hand, a higher differential pressure, and thus higher partial pressure, leads, according to Henry's law, to higher solubility of CO_2. The higher CO_2 availability is also reflected in significantly higher values for the FE_{CO} in the local profile (Figure 5.6E).

In conclusion, higher differential pressures facilitate CO_2 dissolution on the gas side and create a larger gas/liquid interface. This leads to an increased local CO_2 concentration throughout the flooded agglomerate. Enhanced CO_2 availability, in turn, results in higher FE_{CO} and lower local pH values. Higher pressures indeed have improved the CO_2R-active region of the electrode from 20% to more than 50% of the flooded electrode at $200\,\mathrm{mA\,cm^{-2}}$.

5.4.2.3 Influence of PTFE mass fraction

PTFE plays a decisive role in imparting hydrophobic properties to the porous electrode, thereby mitigating the risk of complete pore flooding by the electrolyte. Here, I study the impact of PTFE content on electrolyte intrusion, local electrode states, and performance. The PTFE content was varied between 1 and $3\,\mathrm{wt\%}$ PTFE mass fractions for an overpressure of $100\,\mathrm{mbar}$, using electrodes with a thickness of approximately $300\,\mu\mathrm{m}$.

Experimental and simulation results of polarization and FE_{CO}-current density curves are shown in Figure 5.7A and B. The experimental study shows that a lower PTFE content in the electrode correlates with reduced potential losses across the entire current range (Figure 5.7A). Reproducing the experiment with the model reveals a significant decrease of up to 36% in the electrochemically active surface area with increasing PTFE content (Figure 5.7C). A reconstruction of the microstructure from FIB-SEM experiments confirms the ECSA changes, as a small fraction of only 62% of pore walls is not covered by PTFE for an electrode with a PTFE content of $3\,\mathrm{wt\%}$ (Table S2). Beyond catalyst surface coverage, excessively high PTFE content hinders catalyst surface wetting, leading to a reduced effective ECSA (Figure 5.7F).

Apart from a higher ECSA, the electrode with lower PTFE content shows higher FE_{CO} values

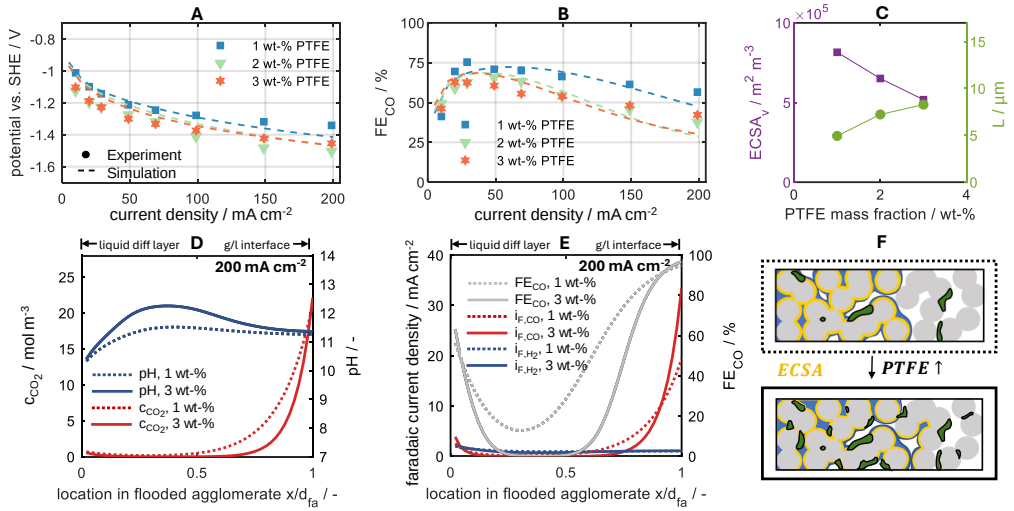

Figure 5.7: Impact of PTFE mass fraction on GDE performance and state: Experimental and simulated (A) polarization curves and (B) FE_{CO} (differential pressure: 100 mbar, electrode layers: 80, i.e. electrode thickness around 300 µm). (C) Identified volumetric electrochemically active surface area ($ECSA_v$) and apparent thickness L of liquid electrolyte layer between catalyst and gas phase in flooded agglomerate as a function of the PTFE mass fraction. (D) Local CO_2 concentration and pH as well as (E) local profiles of Faradaic current densities and FE_{CO} along flooded agglomerate for 3 wt% (solid line) and 1 wt% differential pressure (dashed line) at 200 mA cm^{-2}. (F) Illustration of the increase in PTFE proportion resulting in a decrease in ECSA. Measurements were done in a flow cell with 1 M $KHCO_3$, and potentials are iR-corrected.

for current densities above 20 mA cm^{-2} (Figure 5.7B). The concentration profile of CO_2 at a current density of 200 mA cm^{-2} exhibits a higher dissolved CO_2 concentration for a lower PTFE content (Figure 5.7D). This is caused by a decrease in the thickness of the flooded agglomerate d_{fa} for less PTFE from 317 to 289 µm in the electrodes (Table 5.1), resulting in a lower value of L and in shorter transport distances of dissolved CO_2 as shown in Figure 5.7C. The observation that a higher PTFE content leads to increased flooding of the electrode was also noted by Bienen et al.[208]. They observed an earlier electrolyte breakthrough with higher PTFE content with the same kind of electrodes. Possible reasons for this unintuitive behavior could be increasing capillary forces with decreasing pore size at a higher PTFE amount or a 'slipping' of electrolyte over the less rough PTFE surface.[208] Nevertheless, having at least small amounts of PTFE is essential for GDE operation. Pure Ag-GDEs without PTFE experienced strong electrolyte permeation on the gas side and showed an FE_{CO} of around 0, even at low current densities (not shown here). This indicates that the electrodes were completely flooded with electrolyte and lost their functionality. The shorter diffusive transport distances of CO_2 observed with lower PTFE content result in a lower local pH (Figure 5.7D) and an increase in local FE_{CO} at 200 mA cm^{-2} (Figure 5.7E). Therefore, tuning PTFE content and distribution is essential to stabilize the gas/liquid boundary

in the electrode. The goal is to adjust PTFE content to establish a stable phase boundary with a good gas supply, and as little PTFE as possible to avoid blocking of the catalyst surface resulting in higher potential losses.
Interestingly, electrode performances of the 2 and $3\,\mathrm{wt}\%$ PTFE electrodes are nearly identical although the values of $\mathrm{ECSA_v}$ and apparent electrolyte layer thickness L are different. This is caused by two aspects. Firstly, the higher $\mathrm{ECSA_v}$ decreases $\mathrm{FE_{CO}}$ whereas the lower diffusion length of CO_2 increases $\mathrm{FE_{CO}}$. Thus, a combination of both results in similar $\mathrm{FE_{CO}}$. Both phenomena do not contribute equally to the change in performance, which is why a further increase in L and a decrease in $ECSA_\mathrm{v}$ leads to a change in $\mathrm{FE_{CO}}$, as is the case with the electrode with $1\,\mathrm{wt}\%$ PTFE.

5.4.3 Local sensitivity analysis

A local sensitivity analysis was performed to show clearly the impact of the single model parameters on electrode performance. Each parameter ξ was varied by $\pm 5\%$ from its original value ξ^0, and changes in electrode potential and $\mathrm{FE_{CO}}$ along the current density were evaluated using relative sensitivities for electrode potential $s_{\mathrm{E},\xi}$ and Faradaic efficiency $s_{\mathrm{FE_{co}},\xi}$:

$$\xi^{+/-} = \xi^0 \pm 0.05\xi^0, \tag{5.38}$$

$$s_{y,\xi}(i) = \left.\frac{\partial y(i,\xi)}{\partial \xi}\right|_{\xi=\xi^0} \cdot \frac{\xi^0}{y(i,\xi^0)}, \tag{5.39}$$

$$s_{y,\xi}(i) \approx \frac{y^+(i) - y^-(i)}{\xi^+ - \xi^-} \cdot \frac{\xi^0}{y(i,\xi_0)}, \tag{5.40}$$

with $y = \{E, \mathrm{FE_{CO}}\}$.
The analysis revealed that all parameters ξ reduce the overpotential when increasing their values (negative value of $s_{\mathrm{FE_{co}},\xi}$), however, only to a very limited extent (Figure 5.8A). Parameters affecting the ECSA, such as electrode thickness d_{GDE}, volume specific surface area of the Ag catalyst a_{cat}, and thickness of flooded agglomerate d_{fa}, exhibited relatively high sensitivity values. This indicates that a large active catalyst area predominantly improves the electrode potential. Additionally, increased porosity ε and area of the gas/liquid interface S_{gl} enhance the potential due to better transport, suppressing the HER. Yet, all effects are limited to a few millivolts.
$\mathrm{FE_{CO}}$ exhibited higher relative sensitivity to parameter variations than potential (Figure 5.8B). Conversely, this means that the electrode structure parameters are most important for improving FE, whereas they have less impact on potential. The highest relative sensitivity values were observed at high current densities and for parameters directly influencing mass transport: For

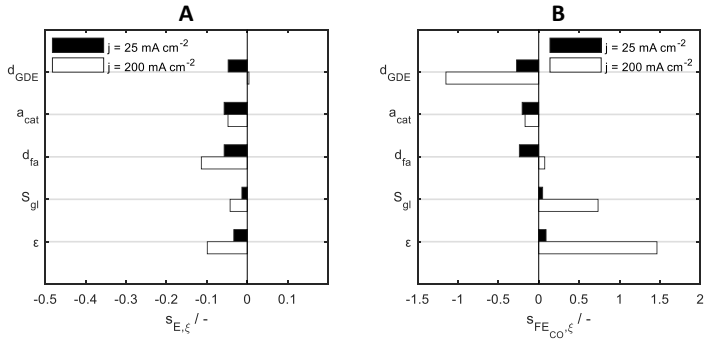

Figure 5.8: Local relative sensitivity of parameter ξ to a 5% variation from its original value on the electrode potential $s_{\mathrm{E},\xi}$ and Faradaic efficiency $s_{\mathrm{FE_{CO}},\xi}$ at 25 and 200 $\mathrm{mA\,cm^{-2}}$. Negative values of $s_{\mathrm{E},\xi}$ indicate that increasing parameter ξ increases electrode potential, while positive $s_{\mathrm{FE_{CO}},\xi}$ values indicate that increasing parameter ξ increases FE_{CO}. For the analysis, a GDE with 275 µm electrode thickness, 1 wt% PTFE, and a differential pressure of 100 mbar between gas and electrolyte side with 1 M $KHCO_3$ aqueous electrolyte was used.

instance, higher electrode porosity significantly increased FE_{CO} at high current densities by improving gaseous and dissolved CO_2 transport, enhancing CO_2 availability, and reducing transport limitations. The gas/liquid interface S_{gl} had a similar, though slightly lower impact compared to porosity, as S_{gl} primarily enhances dissolved CO_2 transport rather than gaseous or carbonate species transport, which are critical for local pH and thus performance, as discussed in section 5.4.2.2.

Increasing electrode thickness while maintaining constant relative electrolyte intrusion, reduced FE_{CO} mostly at high current densities due to longer diffusion lengths of gaseous and dissolved CO_2. The deviation from the impact of d_{fa}, which does not lower FE_{CO} at high current densities, indicates that gas transport within the electrode becomes crucial at high current densities with this electrode design.

An increase in specific catalyst surface area a_{cat}, for instance through smaller catalyst particles, improved potential but decreased FE_{CO} across the whole current range due to more severe CO_2 transport limitations. This implies that electrode designs generating high local current densities, such as those using nanoparticles, are more prone to transport constraints and necessitate short diffusion paths to achieve a high Faradaic efficiency.

Despite these dependencies, the local sensitivity analysis demonstrates that optimizing electrode potential by increasing the ECSA through a_{cat}, d_{fa}, or d_{GDE} results in a performance decline in FE_{CO}. The most promising strategy for performance enhancement is increasing electrode porosity, although the effects on the gas/liquid interface and electrolyte intrusion length require further clarification.

5.5 Concluding remarks

This study revealed that a high Faradaic efficiency for CO_2 reduction in carbon-free Ag-GDEs requires fast transport of dissolved CO_2 and liquid electrolyte. The former can be achieved by increasing the pressure on the gas side by approx. 100 mbar to increase the gas/liquid interface. An adequate gas-liquid interface is also enabled by adjusting a low fraction of approx. $1\,\mathrm{wt}\%$ of PTFE in the GDE. Both insufficient and excessive PTFE contents were found to be disadvantageous, as they promoted flooding and consequently enhanced the HER. Excessive PTFE also led to a reduction in the ECSA. Moreover, thinner electrodes with a shorter transport distance of liquid electrolyte enhance Faradaic efficiency and carbon efficiency for electrochemical CO_2 reduction by better access to fresh electrolyte. These findings help to position carbon-free gas diffusion electrodes as a competitive design for CO_2 reduction. I focused on three influential operation and electrode parameters, as well as current densities $\leq 200\,\mathrm{mA\,cm^{-2}}$, in order to ensure stable operation of the given electrodes and to develop a mechanistic understanding of how these parameters affect electrode performance. Furthermore, the presented method identifies fundamental transport phenomena and design-performance relationships. These are qualitatively transferable across a broad range of GDE architectures, further operation and electrode parameters, the analysis of non-steady states, long-term durability, and higher current densities in future research, enabling a deep understanding of the underlying processes.

6 Conclusion and Perspective

6.1 Summary and conclusion

Advancing electrochemical CO_2 reduction for technical applications requires a fundamental understanding of the interaction between CO_2R, HER, transport processes, carbonation reactions, and local concentrations with their impact on system performance. This work provided model-based analyses of planar silver electrodes, MOF-coated electrodes, and gas diffusion electrodes to systematically dissect these interactions.

Through model-assisted, dynamic and steady-state investigations under well-defined mass transport conditions at RDEs, this work uncovered the impact of the transient behavior of CO_2R on performance and local state at Ag planar model electrodes. Transient potential inputs significantly influence local reaction conditions because mass transport of CO_2 and bicarbonate are overlapping and occur at time constants similar to potential sweep rates. These dynamics enhance local CO_2 concentration, improve carbon efficiency through bicarbonate buffering, and increase Faradaic efficiency at high scan rates compared to steady-state analysis. These investigations elucidate the origin of the discrepancy between dynamic and steady-state analyses and demonstrate that dynamic measurements are advantageous, offering higher sensitivity to ongoing processes and greater robustness.
Building on these findings, I explored the optimization of planar silver electrodes using UiO-67 MOF coatings. This modification significantly improves Faradaic efficiency across the potential range. Physico-chemical modeling revealed that the performance enhancement originates predominantly from an increase in local CO_2 activity due to CO_2 storage within the UiO-67 layer. A smaller contribution arises from a selective improvement in the effective CO_2 diffusion. In contrast, both the HER and the ECSA remain largely unaffected by the porous MOF coating.
Furthermore, the developed model approach for planar electrodes could be successfully transferred to technical silver gas diffusion electrodes. This illustrates the similarities and differences in the interaction of similar processes arising from different electrode designs: As with planar electrodes, the transport of CO_2 and carbonate species is a key factor influencing electrode performance in gas diffusion electrodes. The transport distances in GDEs are determined by the electrolyte distribution within the electrode and the shape of the gas/liquid interface. By

systematically varying operating and design parameters and reproducing performance through modeling, it was shown that electrode thickness primarily affects the liquid transport distance for the electrolyte and dissolved CO_2. Thin electrodes are identified as the most selective for CO_2R. Higher differential pressures between the gas and electrolyte sides of the electrodes enhance Faradaic efficiency for CO production by increasing the gas/liquid interface area within the porous electrode structure. Additionally, an optimal, low PTFE content improves electrode potential and FE_{CO} by minimizing the coverage of the electrochemically active surface area and reducing electrolyte intrusion into the electrode. This study revealed the different key processes that lead to performance limitations in the electrode and showed in detail how changes in electrode design and operating parameters individually address these processes.

Overall, the model-assisted investigations of this thesis enable new, deep insights into the transient and steady-state behavior of the electrochemical CO_2 reduction in aqueous electrolyte for planar and gas diffusion electrodes. These were used for knowledge-driven advice for better performance assessment, operating conditions, and electrode design.

6.2 Perspective

This work extensively investigated the interactions of fundamental processes on planar and gas diffusion electrodes using silver as a catalyst in aqueous hydrogen carbonate electrolytes. It identified limiting processes and proposed approaches for optimizing these systems. However, it opens up further interesting research questions for future studies.

For all the systems considered, the influence of other cell components and the impact of the anode reaction on the overall system remains an open question. Future work could address ion crossover effects and transport through the membrane, which are particularly relevant for applications in promising MEA setups.

Regarding gas diffusion electrodes, the observed inhomogeneous electrolyte distribution suggests extending the model to additional dimensions and, if feasible, integrating realistic electrode structures with pore size distributions. Furthermore, the potential-dependent flooding of the electrode, or electrowetting, which significantly impacts system behavior and degradation, has not been addressed yet.

While dynamic analysis of planar electrodes provided valuable insights into the interactions of individual processes, a similar analysis for gas diffusion electrodes is still pending and is highly promising. However, the complexity of the system introduces challenges such as transient flooding behavior and significant bubble formation, complicating transient measurements and their interpretation.

The modification of electrode surfaces with the MOF UiO-67 offers a promising approach for

catalyst and performance optimization. However, its applicability to technical gas diffusion electrodes, high current densities, and long operating times still needs to be verified. A comprehensive characterization of the porous MOF coating, covering its structural properties and introducing selective active sites created through targeted modification, would offer a deeper understanding of the MOF's influence and could further enhance the overall performance. In general, the developed model structures can be applied to other electrochemical systems and serve as a starting point for investigating other reactions in electrosynthesis or alternative electrolyte systems.

List of acronyms and symbols

Lattin letters

A	area	m^2
a_i	activity of species i	$-$
a_{cat}	specific surface area of Ag catalyst per electrode volume	$\mathrm{m}^2\,\mathrm{m}^{-3}$
C	capacitance	F, $\mathrm{F}\,\mathrm{m}^{-2}$
c_i	molar concentration of species i	$\mathrm{mol}\,\mathrm{m}^{-3}$
$c_i^{\ominus}$	molar, standard concentration of species i	$\mathrm{mol}\,\mathrm{m}^{-3}$
CE	carbon efficiency	$-$
d	thickness	m
$D_{i,j}$	binary diffusion coefficient of species i in j	$\mathrm{m}^2\,\mathrm{s}^{-1}$
E	potential	V
$\mathbf{E}$	electric field	$\mathrm{V}\,\mathrm{m}^{-1}$
E^0	Nernst potential	V
E^{00}	standard potential	V
$\mathrm{ECSA_a}$	area specific electrochemically active surface area	$\mathrm{m}^2\,\mathrm{m}^{-2}$
$\mathrm{ECSA_v}$	volumetric electrochemically active surface area	$\mathrm{m}^2\,\mathrm{m}^{-3}$
EE_i	energy efficiency of product i	$\%$
F	Faraday constant	$\mathrm{C}\,\mathrm{mol}^{-1}$
f	frequency	Hz
FE_i	Faradaic efficiency of product i	$\%$
G_i	Gibbs free energy	$\mathrm{kJ}\,\mathrm{mol}^{-1}$
H_i^{cp}	Henry's law solubility constant defined via concentration	$\mathrm{mol}\,\mathrm{m}^{-3}\,\mathrm{Pa}^{-1}$
H_i^{xp}	Henry's law solubility constant defined via mixing-ratio	Pa^{-1}
h_m	specific parameter to consider salting out effect of CO_2 dissolution	$\mathrm{m}^3\,\mathrm{kmol}^{-1}$
I	current	A

j	current density	$\mathrm{mA\,cm^{-2}}$
j_0	exchange current density	$\mathrm{m^2\,s^{-1}}$
k_0	reaction rate constant	$\mathrm{mol\,m^{-2}\,s^{-1}}$, $\mathrm{mol\,m^{-3}\,s^{-1}}$
K_i	equilibrium constant of reaction i	–
L	thickness of electrolyte layer between gas and catalyst within GDE	m
L_i	coefficient of proportionality	$\mathrm{m^2\,s^{-1}}$
n	number of cycles	–
$\dot{n}_{\mathrm{CO_2,chem}}$	chemical consumption rate of CO_2	$\mathrm{mol\,s^{-1}}$
$\dot{n}_{\mathrm{CO_2,elchem}}$	electrochemical consumption rate of CO_2	$\mathrm{mol\,s^{-1}}$
N_i	molar flux of species i	$\mathrm{mol\,cm^{-2}\,s^{-1}}$
n_i	number of moles of species i	mol
p	total pressure	Pa
p_i	partial pressure of species i	Pa
p_i^{sat}	saturation vapor pressure of species i	Pa
Q	charge	C
R	universal gas constant	$\mathrm{J\,K^{-1}\,mol^{-1}}$
r	radius	m
r_i	reaction rate of reaction i	$\mathrm{mol\,m^{-2}\,s^{-1}}$, $\mathrm{mol\,m^{-3}\,s^{-1}}$
R_{int}	internal resistance	Ω
RF	roughness factor	–
S	saturation of electrode with electrolyte	–
S_{gl}	specific surface area of gas/liquid interface per geometrical electrode area	–
$\dot{S}_i$	source term of species i	$\mathrm{mol\,m^{-3}\,s^{-1}}$
$s_{y,\xi}$	relative sensitivity of parameter ξ according to variable y	–
T	temperature	K
t	time	s
t_{switch}	time of single linear sweep	s
U	voltage	V
u_i	mobility of species i	$\mathrm{m^2\,mol\,J^{-1}\,s^{-1}}$
v	velocity	$\mathrm{m\,s^{-1}}$
$\dot{V}$	volumetric flow rate	$\mathrm{mL\,min^{-1}}$

x	local coordinate	m
x_i	mole fraction of species i	$\mathrm{mol\,mol^{-1}}$
z	number of electrons transferred	$-$
z_i	charge number of species i	$-$

Greek letters

α	charge transfer coefficient	$-$
ΔH_i^0	theoretical enthalpy change of species i	$\mathrm{kJ\,mol^{-1}}$
Δp	differential pressure between gas and electrolyte side	bar
Δx	thickness of discretization element	m
δ	thickness of liquid diffusion layer	m
δ_{H}	thickness of hydrodynamic layer	m
ϵ	permitivity	$\mathrm{F\,m^{-1}}$
ε	porosity	$-$
η	overpotential	V
Γ	concentration of active surface sites	$\mathrm{mol\,m^{-2}}$
γ_i	activity coefficient	$-$
μ_i	chemical potential of species i	$\mathrm{J\,mol^{-1}}$
ν	scan rate	$\mathrm{mV\,s^{-1}}$
ν_{kin}	kinematic viscosity	$\mathrm{m^2\,s^{-1}}$
$\nu_{i,j}$	stoichometric coefficient of species i in reaction j	$-$
ω	angular velocity	$\mathrm{rad\,s^{-1}}$
ϕ	potential	V
ρ_{e}	electric charge density	$\mathrm{C\,m^{-3}}$
σ	ionic conductivity of the electrolyte	$\mathrm{C^2\,kg^{-1}\,s^{-1}\,m^{-3}}$
τ	tortuosity	$-$
τ_{diff}	time constant of diffusion	s
$\theta_{[\,]}$	surface coverage by free surface sites	$-$
θ_k	surface coverage by adsorbed species k	$-$
$\xi^{+/-}$	variation of parameter ξ	diverse

ξ^0	original value of parameter ξ	diverse

Indices

*	at interface
a	anodic
b	backward
c	cathodic
c1	carbonate reaction of CO_2 to bicarbonate
c2	carbonate reaction of bicarbonate to carbonate
CL	catalyst layer
CO2R	CO_2 reduction
conv	convective
diff	diffusion
disk	disk electrode
diss	dissolved
DL	double layer
E	electrolyte
elyt	electrolyte
eq	equilibrium
evap	evaporation
ext	external
F	faradaic
f	forward
fa	flooded agglomerate
gas	gas phase
GDE	gas diffusion electrode
geom	geometric
gl	gas/liquid interface
HER	hydrogen evolution reaction
int	interface
ldl	liquid diffusion layer

liq	liquid
M	metal
mig	migration
p	pore
sol	dissolution
surf	surface
tf	thin film
tot	total
w	water dissociation reaction

Abbreviations

BPDC	biphenyl-4,4'-dicarboxylic acid
CL	catalyst layer
CO_2R	carbon dioxide reduction
CV	cyclic voltammogram
DFT	density functional theory
DMF	*N,N*-dimethylformamide
ECSA	electrochemically active surface area
EDL	electrical double layer
EIS	electrochemical impedance spectroscopy
GDE	gas diffusion electrode
GDL	gas diffusion layer
HER	hydrogen evolution reaction
HPLC	high-performance liquid chromatography
MEA	membrane electrode assembly
MOF	metal-organic framework
MPL	microporous layer
OER	oxygen evolution reaction
ORR	oxygen reduction reaction
PBT	polybutylene terephthalate
PMOF	polyoxometalate-metalloporphyrin organic framework

PTFE	polytetrafluoroethylene
RDE	rotating disk electrode
RHE	reversible hydrogen electrode
RMSE	root mean square error
RWGS	reverse water gas shift reaction
SEM	scanning electron microscopy
SOEC	solid oxide electrolyzer cell
STL	stereolithography
SURFMOF	surface-grafted metal-organic framework
TCD	thermal conductivity detector
TFFA	thin-film flooded agglomerate
UiO	Universitetet i Oslo
WGS	water gas shift reaction

A Supporting Information

A.1 Supporting information of Chapter 3

A.1.1 Variation of rotation rate

Besides 50 and 300 rpm, an intermediate rotation rate of 150 rpm was also simulated and experimentally validated. Current density curves show still a significant scan rate dependency (see Figure A.1).

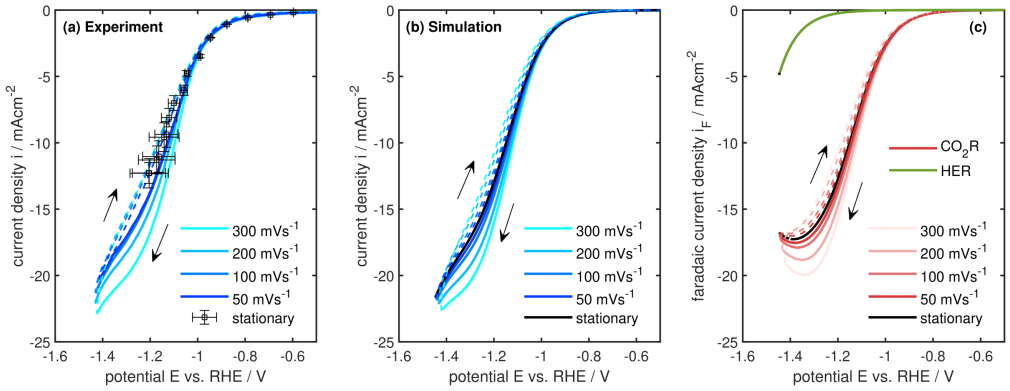

Figure A.1: (a) Experimental and (b) simulated cyclic voltammograms for different scan rates and steady-state polarization curve for a rotation rate of 150 rpm. (c) Corresponding simulated Faradaic current densities for electrochemical CO_2 reduction (CO_2R) and hydrogen evolution reaction (HER) as a function of potential. Forward sweeps are shown in solid lines and backward sweep in dashed lines. Conditions: CO_2 saturated $0.1\,\mathrm{M}$ $KHCO_3$ solution, room temperature, rotation rate of 150 rpm (corresponding to a diffusion layer thickness of $50\,\mu\mathrm{m}$). Potentials are corrected for iR-drop.

A.1.2 Impact of carbonation reactions

The molar changes in hydroxide ions within the diffusion layer due to electrochemical and chemical reactions and due to transport from bulk are shown for stationary operation in Figure A.2a and for dynamic operation in Figure A.2b for a rotation rate of 300 rpm. It shows, that in contrast to 50 rpm, dynamic and stationary operation become very similar in the ratio of c1 and c2. In both cases, the hydroxide sink induced by c2 is clearly larger than by c1. This means that an improved species transport leads to favored reaction of hydroxide ions via bicarbonate-to-carbonate reaction (c2) than via CO_2-to-bicarbonate reaction (c1). Thus, the reaction rate of c2 is largely determined by the species transport of bicarbonate and carbonate species. It is also observed that the transport of hydroxide ions out of the diffusion layer is increased by more than three-fold by increasing the rotation rate from 50 to 300 rpm. This illustrates that with reducing diffusion layer thickness, more hydroxide ions are transported out of the diffusion layer before reacting chemically in the diffusion layer. Still, also for 300 rpm the effect is negligible.

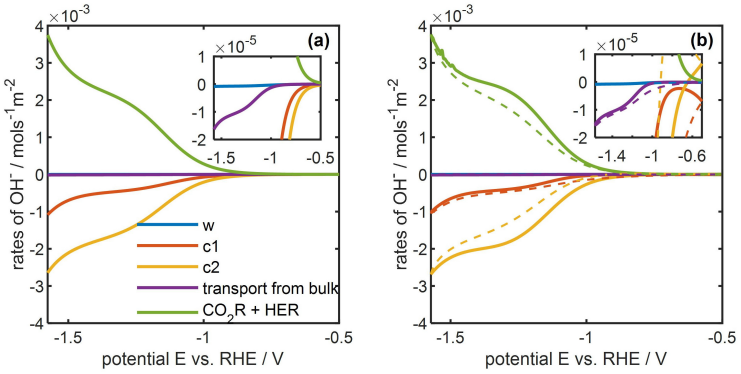

Figure A.2: Molar transport or reaction rates of hydroxide ions in the diffusion layer caused by water dissociation (w), by CO_2-to-bicarbonate reaction (c1)and by bicarbonate-to-carbonate reaction (c2), by transport of hydroxide ions from the bulk and by the electrochemical reactions HER and CO_2R for a rotation rate of 300 rpm for (a) stationary and (b) dynamic operation. Forward sweeps at $300\,\mathrm{mV\,s^{-1}}$ are shown in solid lines and backward sweep in dashed lines. Conditions: CO_2 saturated 0.1 M $KHCO_3$ solution, rotation rate of 50 rpm, room temperature. Potentials are corrected for iR-drop.

The concentration profiles for dissolved species along the diffusion layer for stationary (left) and dynamic (right) operation at 50 rpm for three operation potentials are shown in Figure A.3.
The deviation of the species profiles from a linear profile is due to consumption or production processes in the electrolyte by the homogeneous carbonation reactions. This deviation is more pronounced in the dynamic operation. It illustrates that the buffering zone in dynamic operation is much more expand locally compared to stationary operation due to a better species transport.

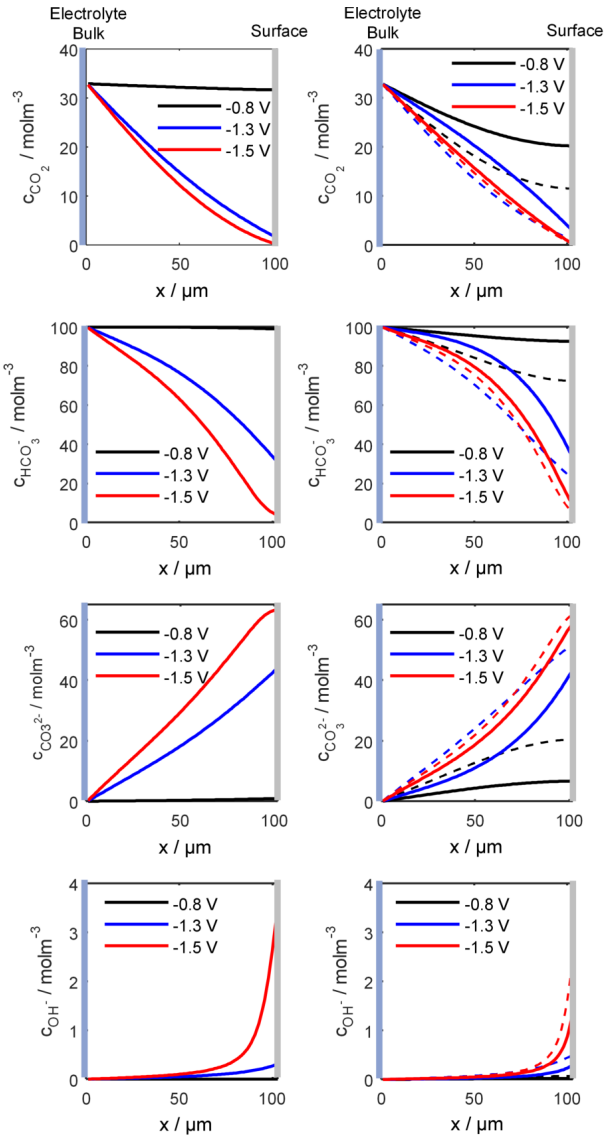

Figure A.3: Concentration profiles within the diffusion layer (bulk at $x = 0$) for dissolved species for stationary (left) and dynamic (right) operation at 50 rpm for three selected potentials. Forward sweeps at $300\,\mathrm{mV\,s^{-1}}$ are shown in solid lines and backward sweep in dashed lines. Conditions: CO_2 saturated 0.1 M $KHCO_3$ solution, rotation rate of 50 rpm, room temperature. Potentials are corrected for iR-drop.

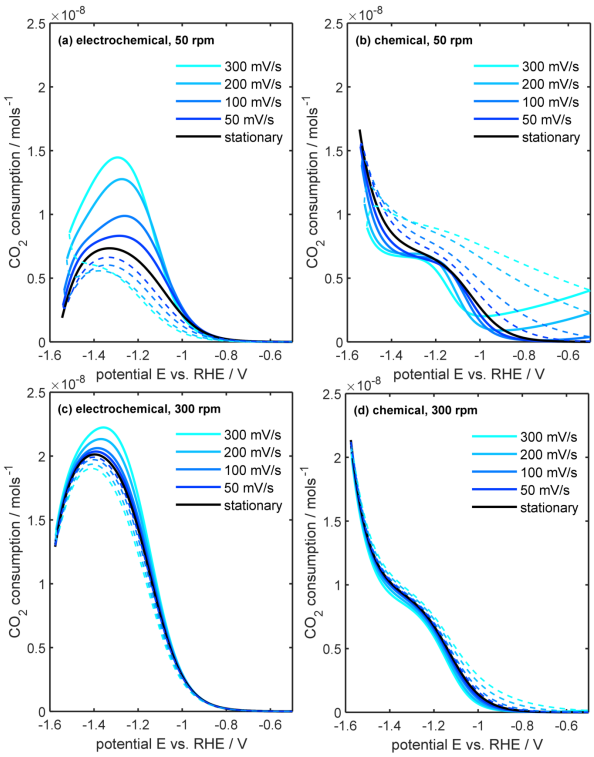

Figure A.4: CO_2 consumption via (a) electrochemical CO_2 reduction and via (b) chemical buffer reaction in the diffusion layer along the potential for steady state and for dynamic operation at different scan rates.

A.1.3 Impact of electrolyte concentration

To investigate if the observations and phenomena explained in this paper are also relevant for higher electrolyte concentration than 0.1 M $KHCO_3$, simulations were done with concentrations of 0.5 and 1.0 M $KHCO_3$. Figure A.5 shows the current density for these concentrations in dynamic and stationary operation. It shows that for higher concentrations, the scan rate dependency and the transport limitations of current and surface concentration are still there and qualitatively very similar. Thus, the effects and time-dependent interactions described before are also relevant for higher concentrations. The decrease of the current plateau to lower absolute current densities with higher electrolyte concentration is mainly caused by the decrease of CO_2 solubility in the electrolyte due to a "salting-out" effect. Higher electrolyte salt concentrations lead to a lower solubility of CO_2 in the electrolyte solution.[168] It decreases from $32.8\,\mathrm{mol\,m^{-3}}$ for 0.1 M to $23.9\,\mathrm{mol\,m^{-3}}$ CO_2 for 1.0 M $KHCO_3$. Therefore, a higher concentration does not necessarily result in a higher availability of CO_2. Thus, the interaction between species transport,

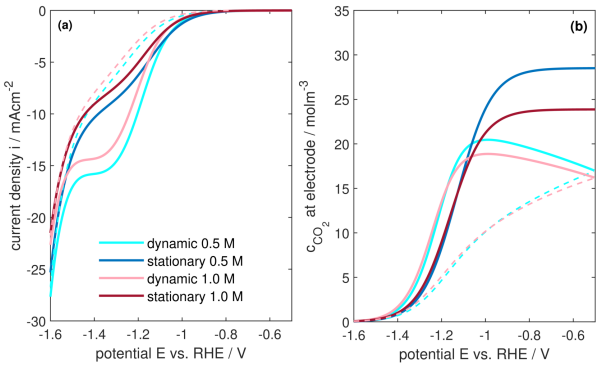

Figure A.5: (a) Simulated cyclic voltammogram for a scan rate of $300\,\mathrm{mV\,s^{-1}}$ and steady state polarization curve for electrolyte concentration of 0.5 and 1.0 M $KHCO_3$ (b) Predicted CO_2 concentration at the electrode during the potential sweep for dynamic and steady state simulation. Forward sweeps are shown in solid lines and backward sweep in dashed lines. Conditions: rotation rate of 50 rpm, room temperature. Potentials are corrected for iR-drop.

electrochemical and chemical reaction for higher potassium bicarbonate concentrations is quite similar to the concentration of 0.1 M, how it is discussed in the main section.

Estimation of the diffusion layer thickness d was done by fitting potential-current curves. The value bounds of this parameter were set in a narrow window calculated by Levich equation (Eq. 2.36). The thus identified thicknesses show a good agreement to the theoretical approach also for these relatively low rotation rates (see Figure A.6). Slight deviations from the linear trend could result from a not fully developed flow profile at low rotation rates.

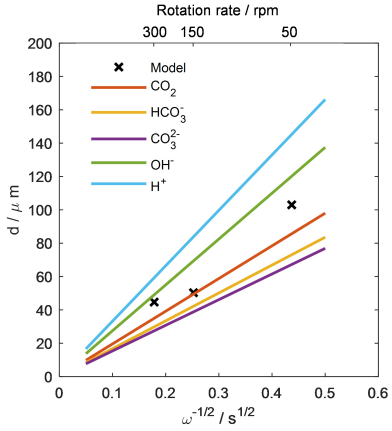

Figure A.6: Theoretical diffusion layer thickness in dependence of angular velocity for a rotating disc electrode setup calculated by Levich equation for different involved species, and parametrized diffusion layer thickness used in the model approach (crosses). Kinematic viscosity was assumed as that of water at $25\,^{\circ}\mathrm{C}$ with $0.893 \times 10^{-6}\,\mathrm{m^2\,s^{-1}}$.

A.2 Supporting information of Chapter 4

A.2.1 Chronoamperometric measurements for product analysis

Chronoamperometric measurements were conducted by holding the potential for 1 hour, with the current response shown in Figure A.7. Gas samples were injected into an online-GC every 6.5 minutes for product analysis. At the end of the experiment, electrolyte samples from both the cathode and anode sides were analyzed using HPLC.

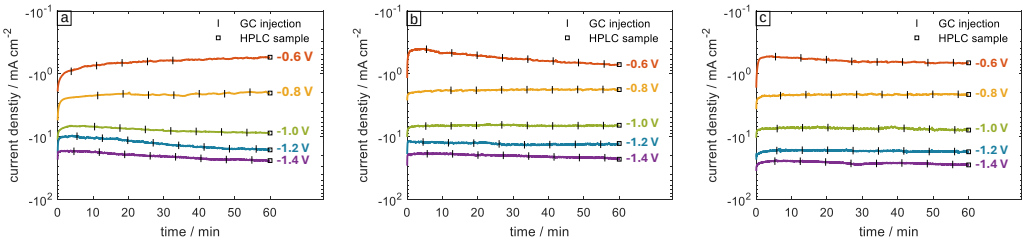

Figure A.7: Chronoamperometric measurements for applied potentials vs. RHE for (a) bare silver electrode, (b) UiO-67-07 and (c) UiO-67-22. Vertical lines show time of GC injections and square at the end of the measurement illustrated time of sampling for HPLC analysis.

A.2.2 Double-layer capacitance measurements

Electrical double-layer capacitance measurements were conducted by cyclic voltammetry measurements in a potential region of no faradaic currents with varying the scan rate (Figure A.8). By extracting the slope of the linear regression of double-layer current density j_{DL} as a function of scan rate the capacitance was determined. The capacitance of the electrical double layer is used to estimate the electrochemically active surface area. The UiO-67 coating does not significantly increase the ECSA. This leads to the assumption that the UiO-67 itself does not contribute to the electrochemical activity of the electrode.

A.2.3 Reproducibility of electrochemical measurements

Chronoamperometric measurements for recording polarization curve and cyclic voltammetry measurements were repeated for bare silver electrodes and UiO-67 coated electrodes with standard

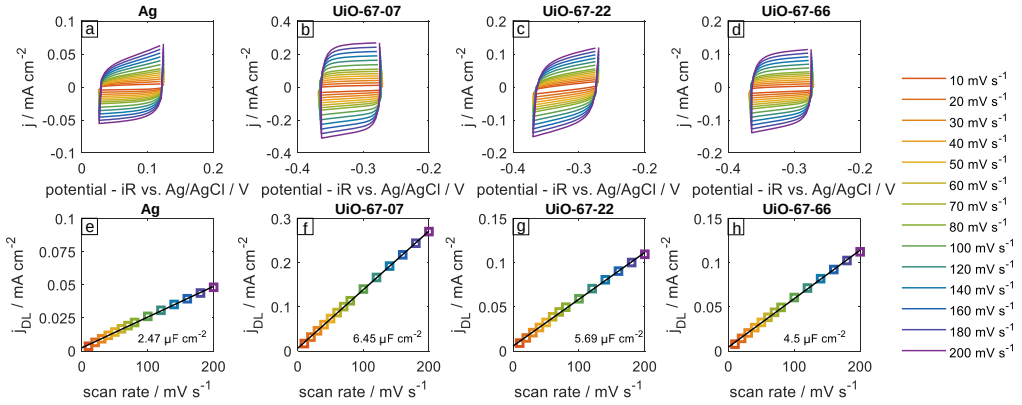

Figure A.8: (a)-(d) Exemplary cyclic voltammograms with variation of the scan rates in the non-faradaic potential region recorded for the determination of electrical double-layer capacitance by (e)-(f) extracting the slope of the linear regression of double-layer current density j_{DL} as a function of scan rate. A bare silver electrode sample and electrodes with variation of precursor concentrations for UiO-67 growth are shown.

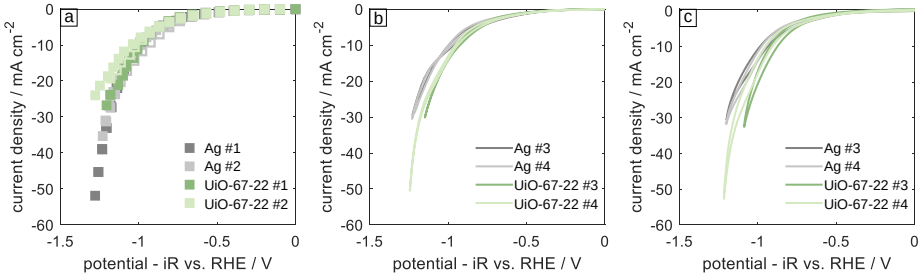

Figure A.9: Repeating measurements for (a) polarization curve and cyclic voltammetry with a scan rate of (b) $25\,\mathrm{mV\,s^{-1}}$ and (c) $200\,\mathrm{mV\,s^{-1}}$. All potentials were corrected for iR-drop.

precursor concentration (Figure A.9). While silver shows very good reproducibility with almost identical curves, MOF coated curves deviate slightly from each other, but the observed trend remains largely the same.

A.2.4 Local sensitivity analysis

A local sensitivity analysis was carried out by varying the adjustment parameters describing the MOF-related enhancement effects (Figure A.10). The parameter values were varied within a range of 0.5 to 10. A value of 1 (black line) corresponds to the reference state of the uncoated silver electrode.

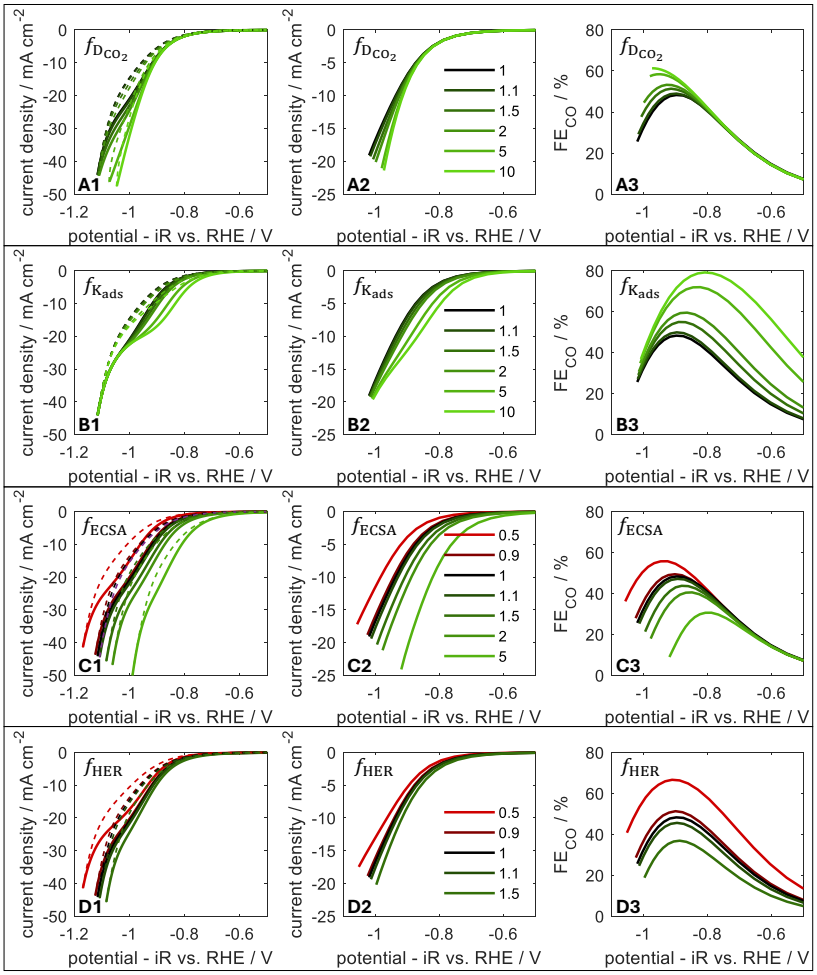

Figure A.10: Systematic variation of the adjustment parameters representing MOF-related enhancement effects: changes in effective CO_2 diffusion coefficient $f_{\mathrm{D_{CO_2}}}$, in chemical CO_2 adsorption equilibrium $f_{\mathrm{K_{ads}}}$, in electrochemically active surface area f_{ECSA}, and in HER reaction rate f_{HER} introduced by the UiO-67 coating. The resulting impact on (A) the cyclic voltammogram at a scan rate of $200\,\mathrm{mV\,s^{-1}}$, (B) the stationary polarization curve, and (C) the stationary FE_{CO} is shown.

This analysis reveals that, although the individual parameters act within a similar order of magnitude, they influence the cyclic voltammogram, polarization, and FE-potential curves in a highly selective manner.

An increase in the effective CO_2 diffusion coefficient within the MOF layer enhances both the absolute current density and FE_{CO} only at very negative potentials ($<-0.85\,\mathrm{V}$). At the same time, the plateau in the cyclic voltammogram shifts toward lower current densities, indicating

improved CO_2 transport. This observation is consistent with the fact that in this potential region, CO_2 reduction is strongly limited by CO_2 mass transport.
In contrast, an increase in the chemical CO_2 adsorption by K_{ads}, leads to higher current densities and FEs in the more positive and intermediate potential range. This can be attributed to an increased local CO_2 activity at the electrode surface, while the overall transport limitation through the liquid diffusion layer remains present.
An increase in the ECSA leads to a significant rise in the absolute current density across the entire potential range for both cyclic voltammetry and steady-state measurements. However, this also results in a faster depletion of CO_2 near the surface, thereby reducing FE_{CO}. Such behavior was not observed experimentally for the MOF-coated electrodes, supporting the assumption that the MOF layer contributes not or only marginally to the ECSA, or that any negative effects are compensated by other mechanisms.
A selective suppression of the HER by the MOF layer leads to an increase in FE_{CO} over the entire potential range. However, this would simultaneously decrease the absolute current density at all potentials, which is inconsistent with the experimentally observed trends.

Overall, the parameter optimization performed in the main part of this work (chapter 4) provides valuable insights into the interplay and combined impact of the individual factors introduced by the MOF layer on performance output.

A.3 Supporting information of Chapter 5

A.3.1 Binary diffusion coefficients in the gas phase

Binary diffusion coefficients for gaseous species i in species j are calculated using Eq. A.1 according to the Chapman-Enskog method[205]:

$$\frac{D_{i,j}^{\text{gas}}}{\text{cm}^2\,\text{s}^{-1}} = \frac{0.00266 \cdot T^{3/2}}{\frac{p}{\text{bar}} \cdot \left(\frac{M_{i,j}}{\text{g mol}^{-1}}\right)^{1/2} \cdot \left(\frac{\sigma_{i,j}}{\text{Å}}\right)^2 \cdot \Omega_D}. \tag{A.1}$$

Here, T is the absolute temperature, and p is the gas pressure. The mean value of molecular weight $M_{i,j}$ is calculated using Equation A.2:

$$M_{i,j} = 2\left(\frac{1}{M_i} + \frac{1}{M_j}\right)^{-1}. \tag{A.2}$$

The characteristic length for the Lennard-Jones potential $\sigma_{i,j}$ is calculated using Equation A.3:

$$\sigma_{i,j} = \frac{\sigma_i + \sigma_j}{2}. \tag{A.3}$$

The diffusion collision integral Ω_D is determined using the relation of Neufeld et al. as shown in Equation A.4:

$$\Omega_D = \frac{A}{(T^*)^B} + \frac{C}{\exp(DT^*)} + \frac{E}{\exp(FT^*)} + \frac{G}{\exp(HT^*)}, \tag{A.4}$$

where $A = 1.06036$, $B = 0.15610$, $C = 0.19300$, $D = 0.47635$, $E = 1.03587$, $F = 1.52996$, $G = 1.76474$, and $H = 3.89411$.
The dimensionless temperature T^* is expressed in Equation A.5 as:

$$T^* = \frac{kT}{\varepsilon_{i,j}}. \tag{A.5}$$

The Lennard-Jones potential $\varepsilon_{i,j}$ is calculated using Equation A.6:

$$\epsilon_{i,j} = \sqrt{\varepsilon_i \epsilon_j}. \tag{A.6}$$

The values of the constants used for the pure substances are listed in Table A.1.

Table A.1: Values for calculation of binary diffusion coefficients with Chapman-Enskog method taken from Polig et al.[205]

Species	σ / Å	ε/k_B / K
CO_2	3.941	195.2
CO	3.690	91.7
H_2O	2.641	809.1
H_2	2.827	59.7

A.3.2 Diffusion length of dissolved CO_2

The apparent thickness of the electrolyte layer between the gas and catalyst surface in partly flooded electrode conditions defines the maximum transport distance of dissolved CO_2 for this electrolyte intrusion state. A higher A_gl, as well as a shorter length of the flooded agglomerate d_fa, leads to a faster transport of CO_2 in the flooded agglomerate according to the transport equation:

$$N_{\mathrm{CO_2}} = -D^{\mathrm{liq}}_{\mathrm{CO_2}}\,\varepsilon^{1.5} S_\mathrm{gl} \nabla c_{\mathrm{CO_2}} \approx -D^{\mathrm{liq}}_{\mathrm{CO_2}}\,\varepsilon^{1.5} S_\mathrm{gl} \frac{\Delta c_{\mathrm{CO_2}}}{d_\mathrm{fa}} = -D^{\mathrm{liq}}_{\mathrm{CO_2}}\,\varepsilon^{1.5} \frac{1}{L} \Delta c_{\mathrm{CO_2}}, \quad \text{(A.7)}$$

with

$$S_\mathrm{gl} = \frac{A_\mathrm{gl}}{A_\mathrm{geom}}, \quad \text{(A.8)}$$

and

$$L = \frac{d_\mathrm{fa}}{S_\mathrm{gl}}. \quad \text{(A.9)}$$

A.3.3 Tafel plot

Figure A.11 shows the Faradaic current-potential curve as a Tafel plot for the exemplary gas-diffusion electrode configuration of $392\,\mu\mathrm{m}$ electrode thickness, $3\,\mathrm{wt}\%$ PTFE, and a differential pressure of $60\,\mathrm{mbar}$. The curves were measured in a flow cell and are dependent on transport limitation. This visualizes the change from the kinetically controlled regime of CO_2 reduction to the transport-controlled regime at a potential of $-1.2\,\mathrm{V}$ vs. SHE and lower.

A.3.4 Variation of electrode thickness

Spray coating used to produce the GDEs leads to slight variations in the electrode thickness in individual experiments, which can be attributed to differences in the loading of the electrodes

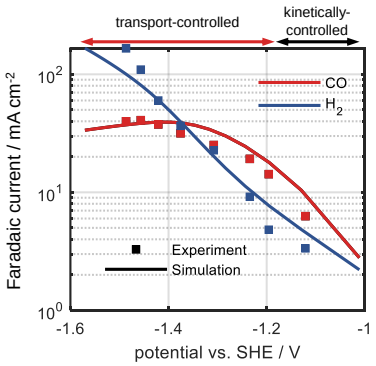

Figure A.11: Experimental and simulated Tafel plot for the Faradaic currents of CO and H_2 for a GDE with 392 µm electrode thickness, 3 wt% PTFE, and a differential pressure of 60 mbar between gas and electrolyte side. Measurements were done in a flow cell with aqueous 1 M $KHCO_3$.

with catalyst and PTFE material. Nevertheless, the fluctuation in electrode thickness in the series of measurements for differential pressure variation and in the series for PTFE content is 35% and 25% of the thickness change during the variation of thickness, respectively (Figure A.12). Since the variation of the thickness is the parameter with the least influence on the electrode performance (discussed in section 5.4.2.1), it can therefore be assumed that the changes in performance when varying the pressure and PTFE content are mainly due to these parameters. In addition, the real thickness of each GDE was considered in the model for simulation.

In connection with this, the simulation was repeated for the variation of the differential pressure with constant electrode thicknesses. The electrode thickness for the measurement of Δp of 20 and 100 mbar was adjusted to a thickness of 350 µm. Cell performance in comparison to the original data is shown in Figure A.13. It can be seen that there are still significant differences between the various differential pressures, which can therefore be attributed to the different differential

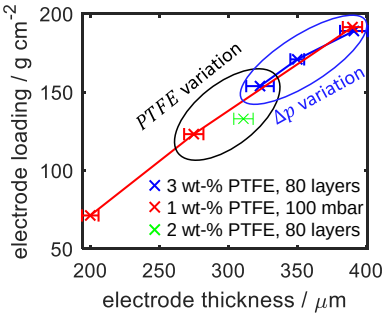

Figure A.12: Electrode loading with PTFE and Ag along the electrode thickness for the electrodes are used for measurements series of differential pressure, PTFE variation and electrode thickness variation.

pressures and less to the fluctuating electrode thicknesses. More precisely, the light variation in electrode thickness has no visible influence on the electrode potential. In the case of Faradaic efficiency, maintaining a constant electrode thickness, highlights a more pronounced difference between the differential pressures of 20 and 60 mbar, thereby clarifying the trend in the impact of the differential pressure.

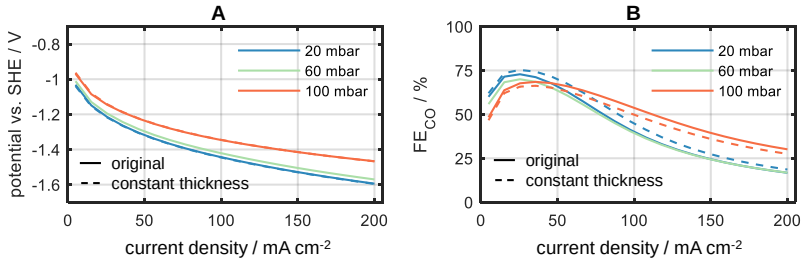

Figure A.13: Simulated (A) polarization curves and (B) FE_{CO} for the variation of differential pressure with fluctuation of electrode thickness (original) and with constant thickness of all electrodes of $350\,\mu m$ with a constant degree of flooding (d_{fa}/d_{GDE}) (PTFE content: $3\,wt\%$).

A.3.5 3D FIB-SEM reconstruction of porous electrode structure

Characteristic parameters for describing the porous media and the wettability were estimated by microstructural reconstruction of FIB-SEM images (Figure A.14). The reconstruction was

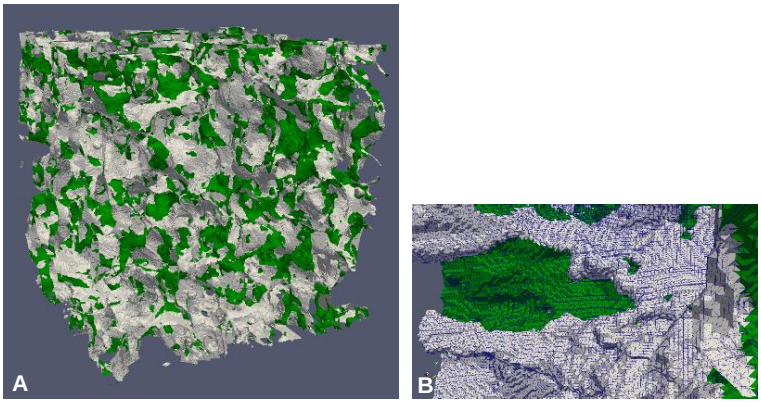

Figure A.14: SEM reconstruction of (A) $97\,wt\%$ Ag gas diffusion electrode by (B) meshing the solid wall by the marching cube algorithm from Lewiner et al.[209].

carried out for GDE with $97\,\mathrm{wt\%}$ Ag. A total box volume of $8490\,\mu\mathrm{m}^3$ was used to extract integral metrics of the cleaned images with statistically relevant quantities. The wall fractions of the different phases were determined by meshing the solid wall using the marching cube algorithm from Lewiner et al.[209]. The solid matrix wall was reconstructed as a stereolithographic file (STL). To distinguish the different solid phases, the mesh faces were colored as described: First, the value of the vertices, which corresponds to the next solid phase in the neighborhood of the vertices, was calculated. For faces with vertices both in PTFE and silver (4.74% of all faces), the face color was assigned to that phase that occupies two vertices of the face. Extracted, electrode structure parameters are listed in Table A.2.
Additional SEM analyses of these electrodes with varying PTFE contents are available in Franzen et al.[202] and are shown in Figure A.15.

Table A.2: Electrode structure parameters for a carbon-free Ag gas diffusion electrode with a silver content of $97\,\mathrm{wt\%}$ by 3D SEM reconstruction and STL-method with the voxel volume V_{total}, volumetric pore wall surface area a_{porewall} and volumetric silver surface area at the pore walls $a_{\mathrm{wall,Ag}}$.

	GDE $97\,\mathrm{wt\%}$ Ag
V_{total}	$8490\,\mu\mathrm{m}^3$
porosity	35%
a_{porewall}	$1.17 \times 10^6\,\mathrm{m}^2\,\mathrm{m}^{-3}$
$a_{\mathrm{wall,Ag}}$	$7.30 \times 10^5\,\mathrm{m}^2\,\mathrm{m}^{-3}$
wall fraction of Ag	62.6%

A.3.6 Experimental Faradaic efficiencies

Experimental Faradaic efficiencies over the current densities for H_2 and CO production of each electrode and parameter variation are shown in Figure A.16. From the figure, the total Faradaic efficiency can also be determined. No other products could be detected. Single deviations from 100% total Faradaic efficiency at low current densities are most likely due to incomplete detection of H_2, caused by low production rates and its poor displacement properties.

A.3.7 Profile root mean square error analysis

To verify whether the parameters were sensitive to finding a local optimum during parameter optimization, a profile root mean square error (RMSE) analysis was conducted analog to former studies. For this purpose, the values of a single parameter were slightly varied to a value of $\pm 10\%$

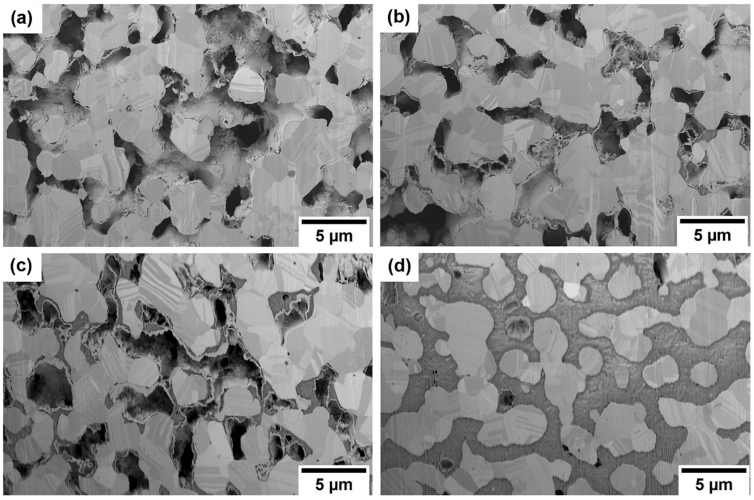

Figure A.15: FIB/SEM images of four silver electrodes with (a) 1 wt%, (b) 2 wt%, (c) 4 wt%, and (d) 9 wt% PTFE from Franzen et al.[202], 2019, licensed under CC BY 4.0 https://creativecommons.org/licenses/by/4.0/.

of the optimized value, and parameter optimization was performed again. The agreement with the experimental data was determined by the calculation of the RMSE of electrode potential and FE_{CO} for simulative and experimental data points n:

$$\text{RMSE} = \sqrt{\sum_{n}(E_{\text{sim}}(n) - E_{\text{exp}}(n))^2} + \sqrt{\sum_{n}(\text{FE}_{\text{CO,sim}}(n) - \text{FE}_{\text{CO,exp}}(n))^2}, \tag{A.10}$$

In Figure A.17, the RMSE values for parameter identification of a single GDE are shown as an example. The minimum RMSE at the final parameter value combination indicates that each optimized parameter is identifiable.

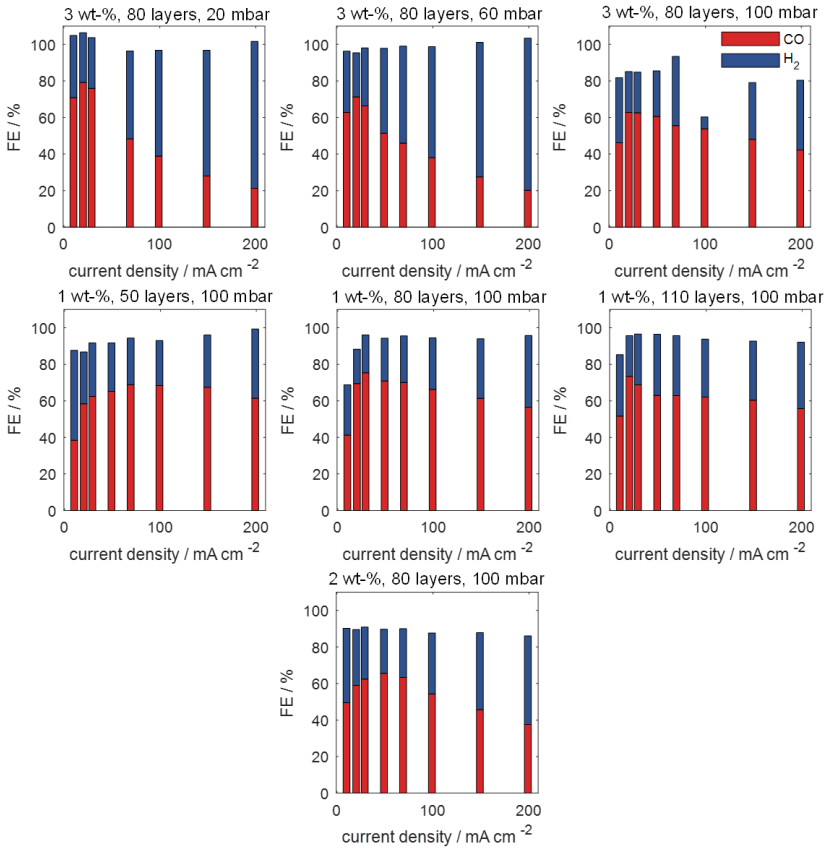

Figure A.16: Experimental Faradaic efficiencies over the current densities for H_2 and CO production across all variations of electrode design and operating parameter.

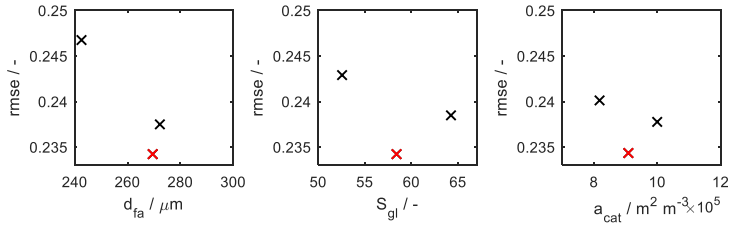

Figure A.17: Profile root mean square error analysis for parameter identification of GDE with 275 µm electrode thickness, 1 wt% PTFE, and a differential pressure of 100 mbar between gas and electrolyte side. The final parameter set for the parameter optimization is marked in red. Highest, reasonable value for d_{fa} was set to 95% of GDE thickness.

List of Figures

1.1 Global atmospheric CO_2 concentration over time compared to annual CO_2 emissions and scheme of CO_2 life cycle via electrochemical CO_2 reduction . . 1
2.1 Current density-overpotential curve according to Butler-Volmer and Tafel plot 7
2.2 Stationary one-sided diffusion at a gas/liquid phase boundary with convective Stefan flow. 11
2.3 Positive nonideal behavior of the vapor pressure. 13
2.4 Potential input over time for cyclic voltammetry and characteristic cyclic voltammogram 15
2.5 Schematic streamlines of flow next to the rotating disk electrode and concentration profile of the stagnant diffusion layer 18
2.6 Schematic mechanism of electrochemical CO_2 reduction 22
2.7 Concentrations of CO_2, HCO_3^-, and CO_3^{2-} at reaction equilibrium in seawater as a function of temperature and salinity 24
2.8 Electrode structures for CO_2R 29
2.9 Cell configurations for electrochemical CO_2 reduction 31
3.1 Model representation for the CO_2R at planar silver electrode 42
3.2 Experimental and simulated cyclic voltammograms and polarization curve with corresponding simulated Faradaic current densities for a rotation rate of 50 rpm. 49
3.3 Predicted CO_2 concentration at the electrode during the potential sweep and corresponding pH value at the electrode for a rotation rate of 50 rpm. . . 50
3.4 Experimental and simulated cyclic voltammograms and polarization curve with corresponding simulated CO_2 concentration and pH for a rotation rate of 300 rpm. 53
3.5 Molar transport or reaction rates of hydroxide ions for a rotation rate of 50 rpm. . . 55
3.6 Carbon efficiency along the potential for 50 rpm and 300 rpm. 56
3.7 Simulated Faradaic efficiencies of electrochemical CO_2 reduction for stationary and dynamic operation for 50 and 300 rpm. 58
4.1 Model representation for the CO_2R at planar silver electrode coated with MOF layer 66

4.2 Cyclic voltammogram, polarization curve, and capacitance of the double layer for a bare silver electrode and UiO-67@Ag samples. 69
4.3 Faradaic current density and FE for products of CO_2R at Ag and UiO-67@Ag samples. 70
4.4 Experimental and simulative polarisation curve and FE_CO of CO_2R at Ag and UiO-67-22 sample. 71
5.1 Scheme of gas diffusion electrode model for CO_2 reduction. 77
5.2 Experimental and simulated polarization curves and Faradaic efficiency of carbon monoxide for a GDE. 84
5.3 Simulated local profiles of Faradaic current densities, FE, CO_2 concentration, pH, and CO_2 consumption rate along flooded agglomerate. 85
5.4 Illustration of possible electrolyte arrangement in porous GDE 87
5.5 Impact of electrode thickness on GDE performance and state 88
5.6 Impact of differential pressure on GDE performance and state. 90
5.7 Impact of PTFE mass fraction on GDE performance and state. 92
5.8 Local relative sensitivity analysis for GDE parameters. 94
A.1 Experimental and simulated cyclic voltammograms and polarization curve with corresponding simulated Faradaic current densities for a rotation rate of 150 rpm. 107
A.2 Molar transport or reaction rates of hydroxide ions for a rotation rate of 300 rpm. . 108
A.3 Concentration profiles within the diffusion layer for stationary and dynamic operation at 50 rpm. 109
A.4 CO_2 consumption via electrochemical CO_2 reduction and via chemical buffer reaction 110
A.5 Simulated cyclic voltammogram and polarization curve for electrolyte concentration of 0.5 and 1.0 M $KHCO_3$ with predicted CO_2 concentration. 111
A.6 Theoretical diffusion layer thickness in dependence on angular velocity. 111
A.7 Chronoamperometric measurements for Ag electrode and UiO-67@Ag samples. 112
A.8 Measurments of the double-layer capacitance of Ag electrode and UiO-67@Ag samples. 113
A.9 Repeating measurements for polarization curve and cyclic voltammetry 113
A.10 Systematic variation of adjustment parameters for performance enhancment of UiO-67 coating 114
A.11 Experimental and simulated Tafel plot for a GDE 118
A.12 Electrode loading with PTFE and Ag along the electrode thickness for electrode samples 118
A.13 Simulated polarization curves and FE_{CO} for the variation of differential pressure with fluctuation of electrode thickness. 119
A.14 SEM reconstruction of a $97\,\mathrm{wt}\%$ Ag gas diffusion electrode. 119
A.15 FIB/SEM images of four silver electrodes with variing PTFE content 121

A.16 Experimental Faradaic efficiencies across all variations of electrode design and operating parameter 122
A.17 Profile root mean square error analysis for parameter identification of GDE 122

List of Tables

2.1 Overview of macroscopic-scale electrochemical CO_2R models 36
3.1 Model parameters of planar model 43
3.2 Values of reaction rate constants and equilibrium constants for the carbonate reaction 45
3.3 Model parameters for the consideration of "salting-out" effect 47
4.1 Composition of precursor solution of different samples for the synthesis of UiO-67 via Vapor Assisted Conversion 63
4.2 Model equations for MOF model 67
4.3 Model parameters and variables of planar model coated with MOF layer 68
5.1 Electrode parameters and the respective identified parameters of electrolyte intrusion and electrochemically active surface area 78
5.2 Model equations for GDE model 79
5.3 Material, design, and kinetic parameters that were kept constant for all simulations. 81
A.1 Values for calculation of binary diffusion coefficients with Chapman-Enskog method taken from Polig et al.[205] 117
A.2 Electrode structure parameters for a carbon-free Ag gas diffusion electrode with a silver content of 97 $\mathrm{wt}\%$ by 3D SEM reconstruction 120

Bibliography

[1] N. Climate.gov, Global atmospheric carbon dioxide campared ot annula emissions (1751-2022), **2023**.

[2] U. N. F. C. on Climate Change, The Paris Agreement, **2018**.

[3] H. Hekmatmehr, A. Esmaeili, M. Pourmahdi, S. Atashrouz, A. Abedi, M. Ali Abuswer, D. Nedeljkovic, M. Latifi, S. Farag, A. Mohaddespour, "Carbon capture technologies: A review on technology readiness level", *Fuel* **2024**, *363*, 130898.

[4] E. V. Kondratenko, G. Mul, J. Baltrusaitis, G. O. Larrazábal, J. Pérez-Ramírez, "Status and perspectives of CO_2 conversion into fuels and chemicals by catalytic, photocatalytic and electrocatalytic processes", *Energy Environ. Sci.* **2013**, *6*, 3112–3135.

[5] K. M. G. Langie, K. Tak, C. Kim, H. W. Lee, K. Park, D. Kim, W. Jung, C. W. Lee, H. S. Oh, D. K. Lee, J. H. Koh, B. K. Min, D. H. Won, U. Lee, "Toward economical application of carbon capture and utilization technology with near-zero carbon emission", *Nat. Commun.* **2022**, *13*, 7482.

[6] T. Haas, R. Krause, R. Weber, M. Demler, G. Schmid, "Technical photosynthesis involving CO_2 electrolysis and fermentation", *Nat. Catal.* **2018**, *1*, 32–39.

[7] M. C. O. Monteiro, M. F. Philips, K. J. P. Schouten, M. T. M. Koper, "Efficiency and selectivity of CO_2 reduction to CO on gold gas diffusion electrodes in acidic media", *Nat. Commun.* **2021**, *12*, 4943.

[8] E. J. F. Dickinson, A. J. Wain, "The Butler-Volmer equation in electrochemical theory: Origins, value, and practical application", *J. Electroanal. Chem.* **2020**, *872*, 114145.

[9] A. J. Bard, L. R. Faulkner, *Electrochemical methods: Fundamentals and applications*, *Vol. 2*, John Wiley & Sons, Inc., **2001**.

[10] C. H. Hamann, W. Vielstich, *Elektrochemie*, 4th, Wiley-VCH, Weinheim, **2005**.

[11] J. G. Wijmans, R. W. Baker, "The solution-diffusion model: a review", *J. Membr. Sci.* **1995**, *107*, 1–21.

[12] J. Newman, K. E. Thomas-Alyea, *Electrochemical Systems*, *Vol. 3*, John Wiley & Sons, Inc., New Jersey, **2004**.

[13] G. J. Bauer, PhD thesis, Technical University Munich, Munich, **2012**.

[14] B. Kögl, F. Moser, *Grundlagen der Verfahrenstechnik*, (Ed.: S.-V. W. GmbH), **1981**.

[15] C. Czeslik, H. Seemann, R. Winter, *Basiswissen physikalische Chemie*, 1st edition, B. G. Teubner GmbH, Stuttgart/Leipzig/Wiesbaden, **2001**.

[16] N. Eliaz, E. Gileadi, *Physical electrochemistry: Fundamentals, techniques, and applications*, 2nd, Wiley-VCH, **2019**.

[17] R. G. Compton, C. E. Banks, *Understanding voltammetry*, World Scientific, **2018**.

[18] N. Elgrishi, K. J. Rountree, B. D. McCarthy, E. S. Rountree, T. T. Eisenhart, J. L. Dempsey, "A practical beginner's guide to cyclic voltammetry", *J. Chem. Educ.* **2017**, *95*, 197–206.

[19] J. Geppert, F. Kubannek, P. Röse, U. Krewer, "Identifying the oxygen evolution mechanism by microkinetic modelling of cyclic voltammograms", *Electrochim. Acta* **2021**, *380*, 137902.

[20] P. Schön, U. Krewer, "Revealing the complex sulfur reduction mechanism using cyclic voltammetry simulation", *Electrochim. Acta* **2021**, *373*, 137523.

[21] B. J. Adesokan, X. Quan, A. Evgrafov, A. Heiskanen, A. Boisen, M. P. Sørensen, "Experimentation and numerical modeling of cyclic voltammetry for electrochemical micro-sized sensors under the influence of electrolyte flow", *J. Electroanal. Chem.* **2016**, *763*, 141–148.

[22] E. J. F. Dickinson, J. G. Limon-Petersen, N. V. Rees, R. G. Compton, "How much supporting electrolyte is required to make a cyclic voltammetry experiment quantitatively "diffusional"? A theoretical and experimental investigation", *J. Phys. Chem. C* **2009**, *113*, 11157–11171.

[23] H. Wang, A. Thiele, L. Pilon, "Simulations of cyclic voltammetry for electric double layers in asymmetric electrolytes: A generalized modified Poisson-Nernst-Planck model", *J. Phys. Chem. C* **2013**, *117*, 18286–18297.

[24] G. Leonzio, A. Hankin, N. Shah, "CO_2 electrochemical reduction: A state-of-the-art review with economic and environmental analyses", *Chem. Eng. Res. Des.* **2024**, *208*, 934–955.

[25] D. Gao, P. Wei, H. Li, L. Lin, G. Wang, X. Bao, "Designing electrolyzers for electrocatalytic CO_2 reduction", *Acta Phys. -Chim. Sin.* **2020**, *0*, 2009021.

[26] F. Li, X. V. Medvedeva, J. J. Medvedev, E. Khairullina, H. Engelhardt, S. Chandrasekar, Y. Guo, J. Jin, A. Lee, H. Thérien-Aubin, A. Ahmed, Y. Pang, A. Klinkova, "Interplay of electrochemical and electrical effects induces structural transformations in electrocatalysts", *Nat. Catal.* **2021**, *4*, 479–487.

[27] F. D. Speck, S. Cherevko, "Electrochemical copper dissolution: A benchmark for stable CO_2 reduction on copper electrocatalysts", *Electrochem. Commun.* **2020**, *115*, 106739.

[28] Y. Hori, H. Konishi, T. Futamura, A. Murata, O. Koga, H. Sakurai, K. Oguma, ""De-activation of copper electrode" in electrochemical reduction of CO_2", *Electrochim. Acta* **2005**, *50*, 5354–5369.

[29] J. Osiewacz, M. Löffelholz, L. Weseler, T. Turek, "CO poisoning of silver gas diffusion electrodes in electrochemical CO_2 reduction", *Electrochim. Acta* **2023**, *445*, 142046.

[30] S. Van Daele, L. Hintjens, S. Hoekx, B. Bohlen, S. Neukermans, N. Daems, J. Hereijgers, T. Breugelmans, "How flue gas impurities affect the electrochemical reduction of CO_2 to CO and formate", *Appl. Catal. B: Environ.* **2024**, *341*, 123345.

[31] N. J. Harmon, H. Wang, "Electrochemical CO_2 reduction in the presence of impurities: Influences and mitigation strategies", *Angew. Chem. Int. Ed.* **2022**, *61*, e202213782.

[32] M. E. Leonard, L. E. Clarke, A. Forner-Cuenca, S. M. Brown, F. R. Brushett, "Investigating electrode flooding in a flowing electrolyte, gas-fed carbon dioxide electrolyzer", *ChemSusChem* **2020**, *13*, 400–411.

[33] F. Lapicque, M. Belhadj, C. Bonnet, J. Pauchet, Y. Thomas, "A critical review on gas diffusion micro and macroporous layers degradations for improved membrane fuel cell durability", *J. Power Sources* **2016**, *336*, 40–53.

[34] A. Bagger, W. Ju, A. S. Varela, P. Strasser, J. Rossmeisl, "Electrochemical CO_2 reduction: A classification problem", *ChemPhysChem* **2017**, *18*, 3266–3273.

[35] X. Li, Y. Chen, X. Zhan, Y. Xu, L. Hao, L. Xu, X. Li, M. Umer, X. Tan, B. Han, A. W. Robertson, Z. Sun, "Strategies for enhancing electrochemical CO_2 reduction to multi-carbon fuels on copper", *Innov. Mater.* **2023**, *1*, 100014.

[36] G. Marcandalli, M. C. O. Monteiro, A. Goyal, M. T. M. Koper, "Electrolyte effects on CO_2 electrochemical reduction to CO", *Acc. Chem. Res.* **2022**, *55*, 1900–1911.

[37] X. Zhu, J. Huang, M. Eikerling, "Electrochemical CO_2 reduction at silver from a local perspective", *ACS Catal.* **2021**, *11*, 14521–14532.

[38] Z. Jiang, C. Clavaguera, C. Hu, S. A. Denisov, S. Shen, F. Hu, J. Ma, M. Mostafavi, "Direct time-resolved observation of surface-bound carbon dioxide radical anions on metallic nanocatalysts", *Nat. Commun.* **2023**, *14*, 7116.

[39] M. Melchionna, P. Fornasiero, M. Prato, M. Bonchio, "Electrocatalytic CO_2 reduction: Role of the cross-talk at nano-carbon interfaces", *Energy Environ. Sci.* **2021**, *14*, 5816–5833.

[40] H. Ait Ahsaine, M. Zbair, A. BaQais, M. Arab, "CO_2 electroreduction over metallic oxide, carbon-based, and molecular catalysts: A mini-review of the current advances", *Catalysts* **2022**, *12*, 450.

[41] A. Bagger, O. Christensen, V. Ivaništšev, J. Rossmeisl, "Catalytic CO_2/CO reduction: Gas, aqueous, and aprotic phases", *ACS Catal.* **2022**, *12*, 2561–2568.

[42] M. Re Fiorentin, F. Risplendi, C. Salvini, J. Zeng, G. Cicero, H. Jónsson, "Silver electrodes are highly selective for CO in CO_2 electroreduction due to interplay between voltage dependent kinetics and thermodynamics", *J. Phys. Chem. Lett.* **2024**, *15*, 11538–11545.

[43] T. Hatsukade, K. P. Kuhl, E. R. Cave, D. N. Abram, T. F. Jaramillo, "Insights into the electrocatalytic reduction of CO_2 on metallic silver surfaces", *Phys. Chem. Chem. Phys.* **2014**, *16*, 13814–13819.

[44] A. Bagger, W. Ju, A. S. Varela, P. Strasser, J. Rossmeisl, "Electrochemical CO_2 reduction: Classifying Cu facets", *ACS Catal.* **2019**, *9*, 7894–7899.

[45] S. J. Raaijman, N. Arulmozhi, M. T. M. Koper, "Morphological stability of copper surfaces under reducing conditions", *ACS Appl. Mater. Interfaces* **2021**, *13*, 48730–48744.

[46] R. Reske, H. Mistry, F. Behafarid, B. Roldan Cuenya, P. Strasser, "Particle size effects in the catalytic electroreduction of CO_2 on Cu nanoparticles", *J. Am. Chem. Soc.* **2014**, *136*, 6978–6986.

[47] H. S. Jeon, J. Timoshenko, F. Scholten, I. Sinev, A. Herzog, F. T. Haase, B. Roldan Cuenya, "Operando insight into the correlation between the structure and composition of CuZn nanoparticles and their selectivity for the electrochemical CO_2 reduction", *J. Am. Chem. Soc.* **2019**, *141*, 19879–19887.

[48] S. S. A. Shah, M. Sufyan Javed, T. Najam, C. Molochas, N. A. Khan, M. A. Nazir, M. Xu, P. Tsiakaras, S.-J. Bao, "Metal oxides for the electrocatalytic reduction of carbon dioxide: Mechanism of active sites, composites, interface and defect engineering strategies", *Coord. Chem. Rev.* **2022**, *471*, 214716.

[49] T. N. Nguyen, M. Salehi, Q. V. Le, A. Seifitokaldani, C. T. Dinh, "Fundamentals of electrochemical CO_2 reduction on single-metal-atom catalysts", *ACS Catal.* **2020**, *10*, 10068–10095.

[50] C. Jia, K. Dastafkan, W. Ren, W. Yang, C. Zhao, "Carbon-based catalysts for electrochemical CO_2 reduction", *Sustain. Energy Fuels* **2019**, *3*, 2890–2906.

[51] M. Abdinejad, A. Seifitokaldani, C. Dao, E. H. Sargent, X.-a. Zhang, H. B. Kraatz, "Enhanced electrochemical reduction of CO_2 catalyzed by cobalt and iron amino porphyrin complexes", *ACS Appl. Energy Mater.* **2019**, *2*, 1330–1335.

[52] K. A. Adegoke, J. O. Ighalo, J. Conradie, C. R. Ohoro, J. F. Amaku, K. O. Oyedotun, N. W. Maxakato, K. G. Akpomie, E. S. Okeke, C. Olisah, A. Malloum, "Metal-organic framework composites for electrochemical CO_2 reduction reaction", *Sep. Purif. Technol.* **2024**, 126532.

[53] N. Oppel, P. Röse, S. Heuser, M. Prokein, U.-P. Apfel, U. Krewer, "Unveiling the kinetics of CO_2 reduction in aprotic electrolyte: The critical role of adsorption", *Electrochim. Acta* **2024**, *490*, 144270.

[54] R. Witzel, L. Wildersinn, E. Tusini, S. Czioska, I. Dorner, A. Zimina, J.-D. Grunwaldt, P. Röse, "Investigation of the performance and stability of copper and brass nanoparticles for CO_2 reduction in organic electrolytes", *J. CO2 Util.* **2025**, *97*, 103138.

[55] A. Fortunati, F. Risplendi, M. Re Fiorentin, G. Cicero, E. Parisi, M. Castellino, E. Simone, B. Iliev, T. J. S. Schubert, N. Russo, S. Hernández, "Understanding the role of imidazolium-based ionic liquids in the electrochemical CO_2 reduction reaction", *Commun. Chem.* **2023**, *6*, 84.

[56] W. Paik, T. N. Andersen, H. Eyring, "Kinetic studies of the electrolytic reduction of carbon dioxide on the mercury electrode", *Electrochim. Acta* **1969**, *14*, 1217–1232.

[57] A. Murata, Y. Hori, "Product selectivity affected by cationic species in electrochemical reduction of CO_2 and CO at a Cu electrode", *Bull. Chem. Soc. Jpn.* **1991**, *64*, 123–127.

[58] C. J. Bondue, M. Graf, A. Goyal, M. T. M. Koper, "Suppression of hydrogen evolution in acidic electrolytes by electrochemical CO_2 reduction", *J. Am. Chem. Soc.* **2021**, *143*, 279–285.

[59] P. Moreno-García, N. Kovács, V. Grozovski, M. d. J. Gálvez-Vázquez, S. Vesztergom, P. Broekmann, "Toward CO_2 electroreduction under controlled mass flow conditions: A combined inverted RDE and gas chromatography approach", *Anal. Chem.* **2020**, *92*, 4301–4308.

[60] H. Ooka, M. C. Figueiredo, M. T. M. Koper, "Competition between hydrogen evolution and carbon dioxide reduction on copper electrodes in mildly acidic media", *Langmuir* **2017**, *33*, 9307–9313.

[61] L. B. T. de Kam, T. L. Maier, K. Krischer, "Electrolyte effects on the alkaline hydrogen evolution reaction: A mean-field approach", *Electrochim. Acta* **2024**, *497*, 144530.

[62] S. Ringe, C. G. Morales-Guio, L. D. Chen, M. Fields, T. F. Jaramillo, C. Hahn, K. Chan, "Double layer charging driven carbon dioxide adsorption limits the rate of electrochemical carbon dioxide reduction on gold", *Nat. Commun.* **2020**, *11*, 33.

[63] W. Deng, P. Zhang, B. Seger, J. Gong, "Unraveling the rate-limiting step of two-electron transfer electrochemical reduction of carbon dioxide", *Nat. Commun.* **2022**, *13*, 803.

[64] M. König, J. Vaes, E. Klemm, D. Pant, "Solvents and supporting electrolytes in the electrocatalytic reduction of CO_2", *iScience* **2019**, *19*, 135–160.

[65] R. N. Roy, L. N. Roy, K. M. Vogel, C. Porter-Moore, T. Pearson, C. E. Good, F. J. Millero, D. M. Campbell, "The dissociation constants of carbonic acid in seawater at salinities 5 to 45 and temperatures 0 to 45°C", *Mar. Chem.* **1993**, *44*, 249–267.

[66] K. G. Schulz, U. Riebesell, B. Rost, S. Thoms, R. E. Zeebe, "Determination of the rate constants for the carbon dioxide to bicarbonate inter-conversion in pH-buffered seawater systems", *Mar. Chem.* **2006**, *100*, 53–65.

[67] H. Hashiba, L.-C. Weng, Y. Chen, H. K. Sato, S. Yotsuhashi, C. Xiang, A. Z. Weber, "Effects of electrolyte buffer capacity on surface reactant species and the reaction rate of in electrochemical CO_2 reduction", *J. Phys. Chem. C* **2018**, *122*, 3719–3726.

[68] J. Resasco, Y. Lum, E. Clark, J. Z. Zeledon, A. T. Bell, "Effects of anion identity and concentration on electrochemical reduction of CO_2", *ChemElectroChem* **2018**, *5*, 1064–1072.

[69] M. N. Jackson, O. Jung, H. C. Lamotte, Y. Surendranath, "Donor-dependent promotion of interfacial proton-coupled electron transfer in aqueous electrocatalysis", *ACS Catal.* **2019**, *9*, 3737–3743.

[70] G. Marcandalli, A. Goyal, M. T. M. Koper, "Electrolyte effects on the Faradaic efficiency of CO_2 reduction to CO on a gold electrode", *ACS Catal.* **2021**, *11*, 4936–4945.

[71] J. M. Yoo, J. Ingenmey, M. Salanne, M. R. Lukatskaya, "Anion effect in electrochemical CO_2 Reduction: From spectators to orchestrators", *J. Am. Chem. Soc.* **2024**, *146*, 31768–31777.

[72] J. N. Mills, I. T. McCrum, M. J. Janik, "Alkali cation specific adsorption onto fcc(111) transition metal electrodes", *Phys. Chem. Chem. Phys.* **2014**, *16*, 13699–13707.

[73] M. R. Singh, Y. Kwon, Y. Lum, J. W. Ager, A. T. Bell, "Hydrolysis of electrolyte cations enhances the electrochemical reduction of CO_2 over Ag and Cu", *J. Am. Chem. Soc.* **2016**, *138*, 13006–13012.

[74] J. Resasco, L. D. Chen, E. Clark, C. Tsai, C. Hahn, T. F. Jaramillo, K. Chan, A. T. Bell, "Promoter effects of alkali metal cations on the electrochemical reduction of carbon dioxide", *J. Am. Chem. Soc.* **2017**, *139*, 11277–11287.

[75] M. C. O. Monteiro, F. Dattila, B. Hagedoorn, R. García-Muelas, N. López, M. T. M. Koper, "Absence of CO_2 electroreduction on copper, gold and silver electrodes without metal cations in solution", *Nat. Catal.* **2021**, *4*, 654–662.

[76] M. Sassenburg, M. Kelly, S. Subramanian, W. A. Smith, T. Burdyny, "Zero-gap electrochemical CO_2 reduction cells: Challenges and operational strategies for prevention of salt precipitation", *ACS Energy Lett.* **2023**, *8*, 321–331.

[77] S. Verma, Y. Hamasaki, C. Kim, W. Huang, S. Lu, H.-R. M. Jhong, A. A. Gewirth, T. Fujigaya, N. Nakashima, P. J. A. Kenis, "Insights into the low overpotential electroreduction of CO_2 to CO on a supported gold catalyst in an alkaline flow electrolyzer", *ACS Energy Lett.* **2018**, *3*, 193–198.

[78] B. Endrődi, E. Kecsenovity, A. Samu, F. Darvas, R. V. Jones, V. Török, A. Danyi, C. Janáky, "Multilayer electrolyzer stack converts carbon dioxide to gas products at high pressure with high efficiency", *ACS Energy Lett.* **2019**, *4*, 1770–1777.

[79] Y. Xu, J. P. Edwards, S. Liu, R. K. Miao, J. E. Huang, C. M. Gabardo, C. P. O'Brien, J. Li, E. H. Sargent, D. Sinton, "Self-cleaning CO_2 reduction systems: Unsteady electrochemical forcing enables stability", *ACS Energy Lett.* **2021**, *6*, 809–815.

[80] Z. Liu, H. Yang, R. Kutz, R. I. Masel, "CO_2 electrolysis to CO and O_2 at high selectivity, stability and efficiency using sustainion membranes", *J. Electrochem. Soc.* **2018**, *165*, J3371–J3377.

[81] E. R. Cofell, U. O. Nwabara, S. S. Bhargava, D. E. Henckel, P. J. A. Kenis, "Investigation of electrolyte-dependent carbonate formation on gas diffusion electrodes for CO_2 electrolysis", *ACS Appl. Mater. Interfaces* **2021**, *13*, 15132–15142.

[82] C. Ampelli, F. Tavella, D. Giusi, A. M. Ronsisvalle, S. Perathoner, G. Centi, "Electrode and cell design for CO_2 reduction: A viewpoint", *Catal. Today* **2023**, *421*, 114217.

[83] J. T. Feaster, C. Shi, E. R. Cave, T. Hatsukade, D. N. Abram, K. P. Kuhl, C. Hahn, J. K. Nørskov, T. F. Jaramillo, "Understanding selectivity for the electrochemical reduction of carbon dioxide to formic acid and carbon monoxide on metal electrodes", *ACS Catal.* **2017**, *7*, 4822–4827.

[84] F. Bienen, D. Kopljar, S. Geiger, N. Wagner, K. A. Friedrich, "Investigation of CO_2 electrolysis on tin foil by electrochemical impedance spectroscopy", *ACS Sustain. Chem. Eng.* **2020**, *8*, 5192–5199.

[85] R. Daiyan, X. Lu, Y. H. Ng, R. Amal, "Highly selective conversion of CO_2 to CO achieved by a three-dimensional porous silver electrocatalyst", *ChemistrySelect* **2017**, *2*, 879–884.

[86] J. Albo, D. Vallejo, G. Beobide, O. Castillo, P. Castano, A. Irabien, "Copper-based metal-organic porous materials for CO_2 electrocatalytic reduction to alcohols", *ChemSusChem* **2017**, *10*, 1100–1109.

[87] I. Dorner, J. Osiewacz, P. Röse, B. Ellendorff, M. Röhe, T. Turek, U. Krewer, "Control of electrolyte intrusion in carbon-free silver gas diffusion electrodes for electrochemical CO_2 reduction", *J. CO2 Util.*, *99*, 103163.

[88] A. A. Samu, I. Szenti, A. Kukovecz, B. Endrodi, C. Janaky, "Systematic screening of gas diffusion layers for high performance CO_2 electrolysis", *Commun. Chem.* **2023**, *6*.

[89] K. Yang, R. Kas, W. A. Smith, T. Burdyny, "Role of the carbon-based gas diffusion layer on flooding in a gas diffusion electrode cell for electrochemical CO_2 reduction", *ACS Energy Lett.* **2020**, *6*, 33–40.

[90] A. H. M. da Silva, S. J. Raaijman, P. J. Corbett, "Mesh GDEs: An alternative to carbon-based electrodes for CO_2 reduction at higher current densities", *Chem. Eng. J.* **2024**, *494*, 153266.

[91] J. Zhang, W. Luo, A. Züttel, "Self-supported copper-based gas diffusion electrodes for CO_2 electrochemical reduction", *J. Mater. Chem.* **2019**, *7*, 26285–26292.

[92] M. Filippi, T. Möller, R. Pastusiak, E. Magori, B. Paul, P. Strasser, "Scale-up of PTFE-based gas diffusion electrodes using an electrolyte-integrated polymer-coated current collector approach", *ACS Energy Lett.* **2024**, *9*, 1361–1368.

[93] G. O. Larrazabal, P. Strom-Hansen, J. P. Heli, K. Zeiter, K. T. Therkildsen, I. Chorkendorff, B. Seger, "Analysis of mass flows and membrane cross-over in CO_2 reduction at high current densities in an MEA-type electrolyzer", *ACS Appl. Mater. Interfaces* **2019**, *11*, 41281–41288.

[94] N. Furuya, H. Aikawa, "Comparative study of oxygen cathodes loaded with Ag and Pt catalysts in chlor-alkali membrane cells", *Electrochim. Acta* **2000**, *45*, 4251–4256.

[95] R. Krause, D. Reinisch, C. Reller, H. Eckert, D. Hartmann, D. Taroata, K. Wiesner-Fleischer, A. Bulan, A. Lueken, G. Schmid, "Industrial application aspects of the electrochemical reduction of CO_2 to CO in aqueous electrolyte", *Chem. Ing. Tech.* **2020**, *92*, 53–61.

[96] P. Jeanty, C. Scherer, E. Magori, K. Wiesner-Fleischer, O. Hinrichsen, M. Fleischer, "Upscaling and continuous operation of electrochemical CO_2 to CO conversion in aqueous solutions on silver gas diffusion electrodes", *J. CO2 Util.* **2018**, *24*, 454–462.

[97] M. G. Kibria, J. P. Edwards, C. M. Gabardo, C. T. Dinh, A. Seifitokaldani, D. Sinton, E. H. Sargent, "Electrochemical CO_2 reduction into chemical feedstocks: From mechanistic electrocatalysis models to system design", *Adv. Mater.* **2019**, *31*, e1807166.

[98] Q. Sun, L. Fu, X. Chang, B. Xu, "Bridging activity gaps between batch and flow reactor configurations in the electroreduction of carbon dioxide", *Sci. Adv.* **2024**, *10*, eadp5697.

[99] D. M. Weekes, D. A. Salvatore, A. Reyes, A. Huang, C. P. Berlinguette, "Electrolytic CO_2 reduction in a flow cell", *Acc. Chem. Res.* **2018**, *51*, 910–918.

[100] G. Wen, B. Ren, X. Wang, D. Luo, H. Dou, Y. Zheng, R. Gao, J. Gostick, A. Yu, Z. Chen, "Continuous CO_2 electrolysis using a CO_2 exsolution-induced flow cell", *Nat. Energy* **2022**, *7*, 978–988.

[101] L. M. Baumgartner, C. I. Koopman, A. Forner-Cuenca, D. A. Vermaas, "When flooding is not catastrophic-woven gas diffusion electrodes enable stable CO_2 electrolysis", *ACS Appl. Energy Mater.* **2022**, *5*, 15125–15135.

[102] L.-C. Weng, A. T. Bell, A. Z. Weber, "Towards membrane-electrode assembly systems for CO_2 reduction: A modeling study", *Energy Environ. Sci.* **2019**, *12*, 1950–1968.

[103] C. Delacourt, P. L. Ridgway, J. B. Kerr, J. Newman, "Design of an electrochemical cell making syngas ($CO+H_2$) from CO_2 and H_2O reduction at room temperature", *J. Electrochem. Soc.* **2008**, *155*, B42–B49.

[104] S. M. A. Kriescher, K. Kugler, S. S. Hosseiny, Y. Gendel, M. Wessling, "A membrane electrode assembly for the electrochemical synthesis of hydrocarbons from $CO_{2(g)}$ and $H_2O_{(g)}$", *Electrochem. Commun.* **2015**, *50*, 64–68.

[105] G. Wang, J. Pan, S. P. Jiang, H. Yang, "Gas phase electrochemical conversion of humidified CO_2 to CO and H_2 on proton-exchange and alkaline anion-exchange membrane fuel cell reactors", *J. CO2 Util.* **2018**, *23*, 152–158.

[106] C. P. O'Brien, R. K. Miao, A. Shayesteh Zeraati, G. Lee, E. H. Sargent, D. Sinton, "CO_2 electrolyzers", *Chem. Rev.* **2024**, 3648–3693.

[107] F. Bidrawn, G. Kim, G. Corre, J. T. S. Irvine, J. M. Vohs, R. J. Gorte, "Efficient reduction of CO_2 in a solid oxide electrolyzer", *Electrochem. Solid-State Lett.* **2008**, *11*, B167.

[108] Z. Ma, J. Zhou, Y. Li, C. Liu, J. Pu, X. Chen, "Developments in CO_2 electrolysis of solid oxide electrolysis cell with different cathodes", *Fuel Cells* **2020**, *20*, 650–660.

[109] Y. Zheng, J. Wang, B. Yu, W. Zhang, J. Chen, J. Qiao, J. Zhang, "A review of high temperature co-electrolysis of H_2O and CO_2 to produce sustainable fuels using solid oxide electrolysis cells (SOECs): Advanced materials and technology", *Chem. Soc. Rev.* **2017**, *46*, 1427–1463.

[110] A. S. Nielsen, B. A. Peppley, O. S. Burheim, "Reverse water gas shift versus carbon dioxide electro-reduction: The reaction pathway responsible for carbon monoxide production in solid oxide co-electrolysis cells", *Energies* **2023**, *16*, 5781.

[111] J. M. Álvarez-Gómez, A. S. Varela, "Review on long-term stability of electrochemical CO_2 reduction", *Energy Fuels* **2023**, *37*, 15283–15308.

[112] R. B. Kutz, Q. Chen, H. Yang, S. D. Sajjad, Z. Liu, I. R. Masel, "Sustainion Imidazolium-functionalized polymers for carbon dioxide electrolysis", *Energy Technol.* **2017**, *5*, 929–936.

[113] N. Gupta, M. Gattrell, B. MacDougall, "Calculation for the cathode surface concentrations in the electrochemical reduction of CO_2 in $KHCO_3$ solutions", *J. Appl. Electrochem.* **2006**, *36*, 161–172.

[114] D. Raciti, M. Mao, C. Wang, "Mass transport modelling for the electroreduction of CO_2 on Cu nanowires", *Nanotechnology* **2018**, *29*, 044001.

[115] T. Burdyny, P. J. Graham, Y. Pang, C.-T. Dinh, M. Liu, E. H. Sargent, D. Sinton, "Nanomorphology-enhanced gas-evolution intensifies CO_2 reduction electrochemistry", *ACS Sustain. Chem. Eng.* **2017**, *5*, 4031–4040.

[116] C. Delacourt, P. L. Ridgway, J. Newman, "Mathematical modeling of CO_2 reduction to CO in aqueous electrolytes", *J. Electrochem. Soc.* **2010**, *157*, B1902–B1910.

[117] M. R. Singh, J. D. Goodpaster, A. Z. Weber, M. Head-Gordon, A. T. Bell, "Mechanistic insights into electrochemical reduction of CO_2 over Ag using density functional theory and transport models", *Proc. Natl. Acad. Sci.* **2017**, *114*, E8812–E8821.

[118] J. Rosen, G. S. Hutchings, Q. Lu, S. Rivera, Y. Zhou, D. G. Vlachos, F. Jiao, "Mechanistic insights into the electrochemical reduction of CO_2 to CO on nanostructured Ag surfaces", *ACS Catal.* **2015**, *5*, 4293–4299.

[119] A. Rendón-Calle, S. Builes, F. Calle-Vallejo, "A brief review of the computational modeling of CO_2 electroreduction on Cu electrodes", *Curr. Opin. Electrochem.* **2018**, *9*, 158–165.

[120] D. Bohra, J. H. Chaudhry, T. Burdyny, E. A. Pidko, W. A. Smith, "Modeling the electrical double layer to understand the reaction environment in a CO_2 electrocatalytic system", *Energy Environ. Sci.* **2019**, *12*, 3380–3389.

[121] S. Ringe, E. L. Clark, J. Resasco, A. Walton, B. Seger, A. T. Bell, K. Chan, "Understanding cation effects in electrochemical CO_2 reduction", *Energy Environ. Sci.* **2019**, *12*, 3001–3014.

[122] H. Li, C. Oloman, "Development of a continuous reactor for the electro-reduction of carbon dioxide to formate – Part 2: Scale-up", *J. Appl. Electrochem.* **2007**, *37*, 1107–1117.

[123] K. Wu, E. Birgersson, P. J. A. Kenis, I. A. Karimi in 8th International Conference on Foundations of Computer-Aided Process Design, **2014**, pp. 639–644.

[124] N. T. Nesbitt, T. Burdyny, H. Simonson, D. Salvatore, D. Bohra, R. Kas, W. A. Smith, "Liquid-solid boundaries dominate activity of CO_2 reduction on gas-diffusion electrodes", *ACS Catal.* **2020**, *10*, 14093–14106.

[125] L.-C. Weng, A. T. Bell, A. Z. Weber, "Modeling gas-diffusion electrodes for CO_2 reduction", *Phys. Chem. Chem. Phys.* **2018**, *20*, 16973–16984.

[126] I. V. Zenyuk, P. K. Das, A. Z. Weber, "Understanding impacts of catalyst-layer thickness on fuel-cell performance via mathematical modeling", *J. Electrochem. Soc.* **2016**, *163*, F691–F703.

[127] M. Löffelholz, J. Osiewacz, A. Lüken, K. Perrey, A. Bulan, T. Turek, "Modeling electrochemical CO_2 reduction at silver gas diffusion electrodes using a TFFA approach", *Chem. Eng. J.* **2022**, *435*, 134920.

[128] S. Pinnow, N. Chavan, T. Turek, "Thin-film flooded agglomerate model for silver-based oxygen depolarized cathodes", *J. Appl. Electrochem.* **2011**, *41*, 1053–1064.

[129] J. Osiewacz, M. Löffelholz, B. Ellendorff, T. Turek, "Modeling mass transfer limitations driven by electrowetting in electrochemical CO_2 reduction at silver gas diffusion electrodes", *J. Power Sources* **2024**, *603*, 234430.

[130] M. Leverett, "Capillary behavior in porous solids", *Trans. AIME* **1941**, *142*, 152–169.

[131] K. S. Udell, "Heat transfer in porous media considering phase change and capillarity - the heat pipe effect", *Int. J. Heat Mass Transf.* **1985**, *28*, 485–495.

[132] M. R. Singh, E. L. Clark, A. T. Bell, "Effects of electrolyte, catalyst, and membrane composition and operating conditions on the performance of solar-driven electrochemical reduction of carbon dioxide", *Phys. Chem. Chem. Phys.* **2015**, *17*, 18924–18936.

[133] L. C. Brée, M. Wessling, A. Mitsos, "Modular modeling of electrochemical reactors: Comparison of CO_2-electolyzers", *Comput. Chem. Eng.* **2020**, *139*, 106890.

[134] I. Dorner, P. Röse, U. Krewer, "Dynamic vs. stationary analysis of electrochemical carbon dioxide reduction: Profound differences in local states", *ChemElectroChem* **2023**, *10*, e202300387.

[135] Y. Hori, K. Kikuchi, S. Suzuki, "Production of CO and CH_4 in electrochemical reduction of CO_2 at metal electrodes in aqueous hydrogencarbonate solution", *Chem. Lett.* **1985**, *14*, 1695–1698.

[136] B. Kumar, M. Asadi, D. Pisasale, S. Sinha-Ray, B. A. Rosen, R. Haasch, J. Abiade, A. L. Yarin, A. Salehi-Khojin, "Renewable and metal-free carbon nanofibre catalysts for carbon dioxide reduction", *Nat. Commun.* **2013**, *4*, 2819.

[137] J. K. Pedersen, T. A. A. Batchelor, A. Bagger, J. Rossmeisl, "High-entropy alloys as catalysts for the CO_2 and CO reduction reactions", *ACS Catal.* **2020**, *10*, 2169–2176.

[138] T. Asset, S. T. Garcia, S. Herrera, N. Andersen, Y. Chen, E. J. Peterson, I. Matanovic, K. Artyushkova, J. Lee, S. D. Minteer, S. Dai, X. Pan, K. Chavan, S. Calabrese Barton, P. Atanassov, "Investigating the nature of the active sites for the CO_2 reduction reaction on carbon-based electrocatalysts", *ACS Catal.* **2019**, *9*, 7668–7678.

[139] G. Li, T. Yan, X. Chen, H. Liu, S. Zhang, X. Ma, "Electrode engineering for electrochemical CO_2 reduction", *Energy Fuels* **2022**, *36*, 4234–4249.

[140] F. Pan, Y. Yang, "Designing CO_2 reduction electrode materials by morphology and interface engineering", *Energy Environ. Sci.* **2020**, *13*, 2275–2309.

[141] J.-B. Vennekötter, R. Sengpiel, M. Wessling, "Beyond the catalyst: How electrode and reactor design determine the product spectrum during electrochemical CO_2 reduction", *Chem. Eng. J.* **2019**, *364*, 89–101.

[142] T. Shinagawa, A. T. Garcia-Esparza, K. Takanabe, "Insight on Tafel slopes from a microkinetic analysis of aqueous electrocatalysis for energy conversion", *Sci. Rep.* **2015**, *5*, 13801.

[143] A. M. Limaye, J. S. Zeng, A. P. Willard, K. Manthiram, "Bayesian data analysis reveals no preference for cardinal Tafel slopes in CO_2 reduction electrocatalysis", *Nat. Commun.* **2021**, *12*, 703.

[144] M. Dunwell, W. Luc, Y. Yan, F. Jiao, B. Xu, "Understanding surface-mediated electrochemical reactions: CO_2 reduction and beyond", *ACS Catal.* **2018**, *8*, 8121–8129.

[145] E. L. Clark, J. Resasco, A. Landers, J. Lin, L.-T. Chung, A. Walton, C. Hahn, T. F. Jaramillo, A. T. Bell, "Standards and protocols for data acquisition and reporting for studies of the electrochemical reduction of carbon dioxide", *ACS Catal.* **2018**, *8*, 6560–6570.

[146] U. Krewer, C. Weinzierl, N. Ziv, D. R. Dekel, "Impact of carbonation processes in anion exchange membrane fuel cells", *Electrochim. Acta* **2018**, *263*, 433–446.

[147] B. J. M. Etzold, U. Krewer, S. Thiele, A. Dreizler, E. Klemm, T. Turek, "Understanding the activity transport nexus in water and CO_2 electrolysis: State of the art, challenges and perspectives", *Chem. Eng. J.* **2021**, *424*, 130501.

[148] U. Krewer, T. Vidakovic-Koch, L. Rihko-Struckmann, "Electrochemical oxidation of carbon-containing fuels and their dynamics in low-temperature fuel cells", *ChemPhysChem* **2011**, *12*, 2518–2544.

[149] D. Zhang, K. Zeng, "Evaluating the behavior of electrolytic gas bubbles and their effect on the cell voltage in alkaline water electrolysis", *Ind. Eng. Chem. Res.* **2012**, *51*, 13825–13832.

[150] J. G. Vos, M. T. M. Koper, "Measurement of competition between oxygen evolution and chlorine evolution using rotating ring-disk electrode voltammetry", *J. Electroanal. Chem.* **2018**, *819*, 260–268.

[151] A. Goyal, G. Marcandalli, V. A. Mints, M. T. M. Koper, "Competition between CO_2 reduction and hydrogen evolution on a gold electrode under well-defined mass transport conditions", *J. Am. Chem. Soc.* **2020**, *142*, 4154–4161.

[152] M. Löffler, P. Khanipour, N. Kulyk, K. J. J. Mayrhofer, I. Katsounaros, "Insights into liquid product formation during carbon dioxide reduction on copper and oxide-derived copper from quantitative real-time measurements", *ACS Catal.* **2020**, *10*, 6735–6740.

[153] R. Casebolt, K. W. Kimura, K. Levine, J. A. Cimada DaSilva, J. Kim, T. A. Dunbar, J. Suntivich, T. Hanrath, "Effect of electrolyte composition and concentration on pulsed potential electrochemical CO_2 reduction", *ChemElectroChem* **2021**, *8*, 681–688.

[154] M. Röhe, F. Kubannek, U. Krewer, "Processes and their limitations in oxygen depolarized cathodes: A dynamic model-based analysis", *ChemSusChem* **2019**, *12*, 2373–2384.

[155] M. Röhe, A. Botz, D. Franzen, F. Kubannek, B. Ellendorff, D. Öhl, W. Schuhmann, T. Turek, U. Krewer, "The key role of water activity for the operating behavior and dynamics of oxygen depolarized cathodes", *ChemElectroChem* **2019**, *6*, 5671–5681.

[156] C. Kim, L.-C. Weng, A. T. Bell, "Impact of pulsed electrochemical reduction of CO_2 on the formation of C2+ products over Cu", *ACS Catal.* **2020**, *10*, 12403–12413.

[157] J. C. Bui, C. Kim, A. Z. Weber, A. T. Bell, "Dynamic boundary layer simulation of pulsed CO_2 Electrolysis on a copper catalyst", *ACS Energy Lett.* **2021**, *6*, 1181–1188.

[158] E. Barsoukov, J. R. Macdonald, *Impedance spectroscopy theory, experiment, and applications*, A John Wiley & Sons, Inc., Hoboken, New Jersey, **2005**.

[159] U. Krewer, M. Christov, T. Vidakovic, K. Sundmacher, "Impedance spectroscopic analysis of the electrochemical methanol oxidation kinetics", *J. Electroanal. Chem.* **2006**, *589*, 148–159.

[160] M. Röhe, D. Franzen, F. Kubannek, B. Ellendorff, T. Turek, U. Krewer, "Revealing the degree and impact of inhomogeneous electrolyte distributions on silver based gas diffusion electrodes", *Electrochim. Acta* **2021**, *389*, 138693.

[161] F. Bienen, D. Kopljar, A. Löwe, S. Geiger, N. Wagner, E. Klemm, K. A. Friedrich, "Revealing mechanistic processes in gas-diffusion electrodes during CO_2 reduction via impedance spectroscopy", *ACS Sustain. Chem. Eng.* **2020**, *8*, 13759–13768.

[162] J. Geppert, P. Röse, S. Czioska, D. Escalera-Lopez, A. Boubnov, E. Saraci, S. Cherevko, J. D. Grunwaldt, U. Krewer, "Microkinetic analysis of the oxygen evolution performance at different stages of iridium oxide degradation", *J. Am. Chem. Soc.* **2022**, *144*, 13205–13217.

[163] E. L. Clark, A. T. Bell, "Direct observation of the local reaction environment during the electrochemical reduction of CO_2", *J. Am. Chem. Soc.* **2018**, *140*, 7012–7020.

[164] M. C. O. Monteiro, A. Mirabal, L. Jacobse, K. Doblhoff-Dier, S. C. Barton, M. T. M. Koper, "Time-Resolved local pH measurements during CO_2 reduction using scanning electrochemical microscopy: Buffering and tip effects", *JACS Au* **2021**, *1*, 1915–1924.

[165] B. Jähne, G. Heinz, W. Dietrich, "Measurement of the diffusion coefficients of sparingly soluble gases in water", *J. Geophys. Res.* **1987**, *92*, 10.767–10.776.

[166] J. H. Wang, "Self-diffusion coefficients of water", *J. Phys. Chem. C* **1965**, *69*, 4412–4412.

[167] M. Flury, T. F. Gimmi in *Methods of soil analysis: Part 4 physical methods*, *Vol. 5*, John Wiley & Sons, **2002**, pp. 1323–1351.

[168] S. Weisenberger, A. Schumpe, "Estimation of gas solubilities in salt solutions at temperatures from 273 K to 363 K", *AIChE J* **1996**, *42*, 298–300.

[169] T. Burdyny, W. A. Smith, "CO_2 reduction on gas-diffusion electrodes and why catalytic performance must be assessed at commercially-relevant conditions", *Energy Environ. Sci.* **2019**, *12*, 1442–1453.

[170] S. Dieckhöfer, D. Öhl, J. R. C. Junqueira, T. Quast, T. Turek, W. Schuhmann, "Probing the local reaction environment during high turnover carbon dioxide reduction with Ag-based gas diffusion electrodes", *Chem. Eur. J.* **2021**, *27*, 5906–5912.

[171] D. A. Henckel, M. J. Counihan, H. E. Holmes, X. Chen, U. O. Nwabara, S. Verma, J. Rodríguez-López, P. J. A. Kenis, A. A. Gewirth, "Potential dependence of the local pH in a CO_2 reduction electrolyzer", *ACS Catal.* **2021**, *11*, 255–263.

[172] E. Tayyebi, J. Hussain, Y. Abghoui, E. Skúlason, "Trends of electrochemical CO_2 reduction reaction on transition metal oxide catalysts", *J. Phys. Chem. C* **2018**, *122*, 10078–10087.

[173] J. Li, J. Halldin Stenlid, M. T. Tang, H.-J. Peng, F. Abild-Pedersen, "Screening binary alloys for electrochemical CO_2 reduction towards multi-carbon products", *J. Mater. Chem.* **2022**, *10*, 16171–16181.

[174] D. Narváez-Celada, A. S. Varela, "CO_2 electrochemical reduction on metal-organic framework catalysts: Current status and future directions", *J. Mater. Chem.* **2022**, *10*, 5899–5917.

[175] L. S. Xie, G. Skorupskii, M. Dinca, "Electrically conductive metal-organic frameworks", *Chem. Rev.* **2020**, *120*, 8536–8580.

[176] Y. R. Wang, Q. Huang, C. T. He, Y. Chen, J. Liu, F. C. Shen, Y. Q. Lan, "Oriented electron transmission in polyoxometalate-metalloporphyrin organic framework for highly selective electroreduction of CO_2", *Nat. Commun.* **2018**, *9*, 4466.

[177] L. Ye, J. Liu, Y. Gao, C. Gong, M. Addicoat, T. Heine, C. Wöll, L. Sun, "Highly oriented MOF thin film-based electrocatalytic device for the reduction of CO_2 to CO exhibiting high Faradaic efficiency", *J. Mater. Chem.* **2016**, *4*, 15320–15326.

[178] J. Lu, Q. Wang, Z. Jin, Y. Xiao, B.-H. Huang, C.-H. Zhang, G.-Z. Yang, Y. Zhou, F.-S. Ke, "One-dimensional metal-organic framework for high-efficiency electrocatalytic reduction of CO_2 to CO", *Chin. J. Chem.* **2024**, *42*, 2788–2794.

[179] X. Tan, C. Yu, C. Zhao, H. Huang, X. Yao, X. Han, W. Guo, S. Cui, H. Huang, J. Qiu, "Restructuring of Cu_2O to Cu_2O@Cu-metal-organic frameworks for selective electrochemical reduction of CO_2", *ACS Appl. Mater. Interfaces* **2019**, *11*, 9904–9910.

[180] A. K. Singh, L. Gu, A. Dutta Chowdhury, A. Indra, "Exploring ligand-controlled C_2 product selectivity in carbon dioxide reduction with copper metal-organic framework nanosheets", *Inorg. Chem.* **2023**, *62*, 8803–8811.

[181] K. Yao, Y. Xia, J. Li, N. Wang, J. Han, C. Gao, M. Han, G. Shen, Y. Liu, A. Seifitokaldani, X. Sun, H. Liang, "Metal-organic framework derived copper catalysts for CO_2 to ethylene conversion", *J. Mater. Chem.* **2020**, *8*, 11117–11123.

[182] N. Sikdar, J. R. C. Junqueira, S. Dieckhofer, T. Quast, M. Braun, Y. Song, H. B. Aiyappa, S. Seisel, J. Weidner, D. Ohl, C. Andronescu, W. Schuhmann, "A metal-organic framework derived $Cu_xO_yC_z$ catalyst for electrochemical CO_2 reduction and impact of local pH change", *Angew. Chem. Int. Ed.* **2021**, *60*, 23427–23434.

[183] H. Furukawa, K. E. Cordova, M. O'Keeffe, O. M. Yaghi, "The chemistry and applications of metal-organic frameworks", *Science* **2013**, *341*, 1230444.

[184] H. Furukawa, N. Ko, Y. B. Go, N. Aratani, S. B. Choi, E. Choi, A. O. Yazaydin, R. Q. Snurr, M. O'Keeffe, J. Kim, O. M. Yaghi, "Ultrahigh porosity in metal-organic frameworks", *Science* **2010**, *329*, 424–428.

[185] P. L. Llewellyn, S. Bourrelly, C. Serre, A. Vimont, M. Daturi, L. Hamon, G. D. Weireld, J.-S. Chang, D.-Y. Hong, Y. Kyu Hwang, S. H. Jhung, G. Ferey, "High uptakes of CO_2 and CH_4 in mesoporous metals - Organic frameworks MIL-100 and MIL-101", *Langmuir* **2008**, *24*, 7245–7250.

[186] S. Mukhopadhyay, M. S. Naeem, G. Shiva Shanker, A. Ghatak, A. R. Kottaichamy, R. Shimoni, L. Avram, I. Liberman, R. Balilty, R. Ifraemov, I. Rozenberg, M. Shalom, N. Lopez, I. Hod, "Local CO_2 reservoir layer promotes rapid and selective electrochemical CO_2 reduction", *Nat. Commun.* **2024**, *15*, 3397.

[187] E. Virmani, J. M. Rotter, A. Mahringer, T. von Zons, A. Godt, T. Bein, S. Wuttke, D. D. Medina, "On-surface synthesis of highly oriented thin metal-organic framework films through vapor-assisted conversion", *J. Am. Chem. Soc.* **2018**, *140*, 4812–4819.

[188] M. J. Katz, Z. J. Brown, Y. J. Colon, P. W. Siu, K. A. Scheidt, R. Q. Snurr, J. T. Hupp, O. K. Farha, "A facile synthesis of UiO-66, UiO-67 and their derivatives", *Chem. Commun.* **2013**, *49*, 9449–9451.

[189] D. K. Yoo, S. H. Jhung, "Selective CO_2 adsorption at low pressure with a Zr-based UiO-67 metal-organic framework functionalized with aminosilanes", *J. Mater. Chem.* **2022**, *10*, 8856–8865.

[190] K. M. Batoo, E. Ali, S. A. Hussein, S. Chandra, A. S. Abdulwahid, S. H. Kareem, S. Hussain, A. A. Omran, M. K. Abid, A. Alawadi, "UiO-67 metal-organic frameworks with dual amino/iodo functionalization, and mixed Zr/Ce clusters: Highly selective and efficient photocatalyst for CO_2 transformation to methanol", *J. Mol. Struct.* **2024**, *1312*, 138492.

[191] K. Trepte, S. Schwalbe, Systematic analysis of porosities in metal-organic frameworks, **2019**.

[192] K. Ao, P. Zhao, Q. Zhang, X. Fan, Q. Fang, G. Wang, Y. Zhu, "Activating the Ni-contenting carbon nanotube by covalent triazine frameworks to form atomically dispersed Ni sites with curvature effect for electrocatalytic CO_2 reduction", *Small Structures* **2024**, *5*, 2300500.

[193] J. Li, H. Shen, C. Ma, H. Zhang, P. Luo, J. Chen, M. Mu, X. Yin, "Assembly and electrocatalytic CO_2 reduction of two-dimensional bimetallic porphyrin-based conjugated cobalt metal-organic framework", *Electrochim. Acta* **2023**, *443*, 141896.

[194] S. Verma, B. Kim, H. R. Jhong, S. Ma, P. J. Kenis, "A Gross-Margin model for defining technoeconomic benchmarks in the electroreduction of CO_2", *ChemSusChem* **2016**, *9*, 1972–1979.

[195] Y. Wu, S. Garg, M. Li, M. N. Idros, Z. Li, R. Lin, J. Chen, G. Wang, T. E. Rufford, "Effects of microporous layer on electrolyte flooding in gas diffusion electrodes and selectivity of CO_2 electrolysis to CO", *J. Power Sources* **2022**, *522*, 230998.

[196] Y. Kong, H. Hu, M. Liu, Y. Hou, V. Kolivoška, S. Vesztergom, P. Broekmann, "Visualisation and quantification of flooding phenomena in gas diffusion electrodes used for electrochemical CO_2 reduction: A combined EDX/ICP-MS approach", *J. Catal.* **2022**, *408*, 1–8.

[197] Y. Wu, L. Charlesworth, I. Maglaya, M. N. Idros, M. Li, T. Burdyny, G. Wang, T. E. Rufford, "Mitigating electrolyte flooding for electrochemical CO_2 reduction via infiltration of hydrophobic particles in a gas diffusion layer", *ACS Energy Lett.* **2022**, *7*, 2884–2892.

[198] M. Heßelmann, B. C. Bräsel, R. G. Keller, M. Wessling, "Simulation-based guidance for improving CO_2 reduction on silver gas diffusion electrodes", *Electrochem. Sci. Adv.* **2022**, *3*, 2100160.

[199] M. C. Paulisch, M. Gebhard, D. Franzen, A. Hilger, M. Osenberg, N. Kardjilov, B. Ellendorff, T. Turek, C. Roth, I. Manke, "Operando laboratory X-Ray imaging of silver-based gas diffusion electrodes during oxygen reduction reaction in highly alkaline media", *Materials* **2019**, *12*, 2686.

[200] H. Hoffmann, M. C. Paulisch, M. Gebhard, J. Osiewacz, M. Kutter, A. Hilger, T. Arlt, N. Kardjilov, B. Ellendorff, F. Beckmann, H. Markötter, M. Luik, T. Turek, I. Manke, C. Roth, "Development of a modular operando cell for X-ray imaging of strongly absorbing silver-based gas diffusion electrodes", *J. Electrochem. Soc.* **2022**, *169*, 044508.

[201] L. M. Baumgartner, A. Goryachev, C. I. Koopman, D. Franzen, B. Ellendorff, T. Turek, D. A. Vermaas, "Electrowetting limits electrochemical CO_2 reduction in carbon-free gas diffusion electrodes", *Energy Adv.* **2023**, *2*, 1893–1904.

[202] D. Franzen, B. Ellendorff, M. C. Paulisch, A. Hilger, M. Osenberg, I. Manke, T. Turek, "Influence of binder content in silver-based gas diffusion electrodes on pore system and electrochemical performance", *J. Appl. Electrochem.* **2019**, *49*, 705–713.

[203] I. Moussallem, S. Pinnow, N. Wagner, T. Turek, "Development of high-performance silver-based gas-diffusion electrodes for chlor-alkali electrolysis with oxygen depolarized cathodes", *Chem. Eng. Process.* **2012**, *52*, 125–131.

[204] W. Zheng, "iR compensation for electrocatalysis studies: Considerations and recommendations", *ACS Energy Lett.* **2023**, *8*, 1952–1958.

[205] B. E. Poling, J. M. Prausnitz, J. P. O'Connell, *The properties of gases and liquids*, fifth edition, McGRAW-HILL, **2004**.

[206] M. Neumann, M. Osenberg, A. Hilger, D. Franzen, T. Turek, I. Manke, V. Schimdt, "On a pluri-Gaussian model for three-phase microstructures, with applications to 3D image data of gas-diffusion electrodes", *Comput. Mater. Sci.* **2019**, *156*, 325–331.

[207] B. De Mot, J. Hereijgers, M. Duarte, T. Breugelmans, "Influence of flow and pressure distribution inside a gas diffusion electrode on the performance of a flow-by CO_2 electrolyzer", *Chem. Eng. J.* **2019**, *378*, 122224.

[208] F. Bienen, M. C. Paulisch, T. Mager, J. Osiewacz, M. Nazari, M. Osenberg, B. Ellendorff, T. Turek, U. Nieken, I. Manke, K. A. Friedrich, "Investigating the electrowetting of silver-based gas-diffusion electrodes during oxygen reduction reaction with electrochemical and optical methods", *Electrochem. Sci. Adv.* **2022**, *3*, e2100158.

[209] T. Lewiner, H. Lopes, A. W. Vieira, G. Tavares, "Efficient implementation of marching cubes' cases with topological guarantees", *JGED* **2003**, *8*, 1–15.